Simulation of Thermal Transport in Semiconductor Nanostructures

by

Song Mei

A dissertation submitted in partial fulfillment of the requirements for the degree of

Doctor of Philosophy
(Electrical and Computer Engineering Department)

at the UNIVERSITY OF WISCONSIN-MADISON 2017

Date of final oral examination: 11/14/2017

The dissertation is approved by the following members of the Final Oral Committee:

Irena Knezevic, Professor, Electrical and Computer Engineering

Luke J. Mawst, Professor, Electrical and Computer Engineering

Dan Botez, Professor, Electrical and Computer Engineering

Mark A. Eriksson, Professor, Physics

ACKNOWLEDGMENTS

I want to express my deepest appreciation to my advisor Irena Knezevic. You are a great teacher, mentor, and role model. More importantly, you are a friend who truly cares about our growth and wellbeing, both academically and as a person. Thank you for showing me how to be strong and independent in this male-dominated field. Your rigorous academic attitude and your desire for knowledge will always impact my future career. Thank you for all your guidance, support, and encouragement during my PhD study.

I also want to thank my wonderful committee members who are also my collaborators, Prof. Luke Mawst, Prof. Dan Botez, and Prof. Mark Eriksson. It has been a privilege to work with you and thank you for all your help. Thanks also to Prof. Srdjan Milicic for your support when I was a TA of your course.

I want to thank Leon Maurer, Zlatan Aksamija and Nishant Sule, for holding my hands when I was just getting started with the Phonon Monte Carlo simulation and many other discussions. Thanks to Olafur Jonasson and Farhad Karimi: the two of you have been nothing but great friends and collaborators from the moment we joined the group together. Thanks to Amirhossein Davoody and Yanbing Shi for your continuous help. I want to thank Gabriel Jaffe, Jeremy Kirch, and Colin Boyle for the many discussions that gave me more insights on the experimental side of world. It was a pleasure to get to know all other group members, Sina Soleimanikahnoj, Alex Gabourie, Jason Hsu, Amanda ZuVerink, Michelle King, and Suraj Suri, so thank you.

Thanks to all the friends I met during graduate school. I wouldn't have survived these years without your company and support. I also want to thank my old friends, many of whom even visited me despite the cold winter of Madison.

Last but not the least, I need to thank my family for always being the strongest support. I couldn't have done anything without my parents guidance. I want to thank my husband, for loving me as who I am. You and Max are my biggest gifts and I look forward to the wonderful adventures for many years to come.

TABLE OF CONTENTS

			Page
LI	ST (OF TABLES	vi
LI	ST (OF FIGURES	vii
\mathbf{A}	BST	RACT	xiv
1	Int	$egin{array}{cccccccccccccccccccccccccccccccccccc$	1
	1.1	Phonons	1
		1.1.1 Bravais Lattice and Reciprocal Lattice	1
		1.1.2 Lattice Waves and Phonon Dispersion	2
		1.1.3 Phonon Distribution and Density of States (DOS)	3
	1.2	Thermal Conductivity in Semiconductor Nanostructures	4
		1.2.1 Fourier's Law	4
		1.2.2 Phonon Scattering	5
	1.3	Phonon Transport	6
		1.3.1 Coherent Phonon Transport	7
		1.3.2 Semiclassical Phonon Transport	7
		1.3.3 Phonon Transport in Semiconductor Nanostructures	8
	1.4	Overview of This Dissertation	8
		1.4.1 Organization of Chapters	9
		1.4.2 Research Accomplishments	10
2	Ser	miclassical Techniques for Predicting Thermal Conductivity	11
	2.1	The Relaxation Time Approximation (RTA)	12
	2.2	Phonon Monte Carlo (PMC)	13
	2.3	Molecular Dynamics (MD)	16
3		nermal Conductivity of Graphene Nanoribbons (GNRs): 2D PMC in Full Dispersion	21
	3.1	Phonon Properties of Graphene	21

				Page
		3.1.1	Phonon Dispersion with Dynamical Matrix Method	. 21
		3.1.2	Phonon DOS from Full Dispersion	
	3.2	Single	Phonon Generation	
		3.2.1	Choosing Energy	
		3.2.2	Choosing Branch	
		3.2.3	Choosing Wave Vector	
	3.3	Simula	ation Domain	
		3.3.1	Boundary Conditions and Contacts	
	3.4		ransport Kernel	
		3.4.1	Phonon Drift and Edge Scattering	
		3.4.2	Phonon Scattering Rate in Graphene	
		3.4.3	Phonon Scattering and Time Step	
	3.5		y Conservation	
	0.0	3.5.1	Initialization	
		3.5.2	Reinitialization	
	3.6		ation Results	
	0.0	3.6.1	Reliability Test	
		3.6.2	Length-Dependent Thermal Conductivity	
		3.6.3	Isotope effect	
		3.6.4	Width-dependent thermal conductivity	
		3.6.5	Bulk Limit	
	3.7		usion to Chapter 3	
	0.1	Concr		. 00
4	Th	ermal	Conductivity of III-V Bulk Materials: 3D RTA with Full Dis	_
	•			
	4.1	Phono	on Scattering Rate in III-V Materials	. 58
		4.1.1	Phonon-Phonon Scattering	. 59
		4.1.2	Mass-Difference Scattering	. 60
		4.1.3	Dopant and Electron Scattering	. 61
	4.2	Therm	nal Conductivity of Binary Compounds	
		4.2.1	Thermal Conductivity of GaAs	. 64
		4.2.2	Thermal Conductivity of AlAs	. 64
		4.2.3	Thermal Conductivity of InAs	
	4.3	Therm	nal Conductivity of Ternary Alloys	. 67
		4.3.1	Thermal Conductivity of InGaAs	
		4.3.2	Thermal Conductivity of AlGaAs	
		4.3.3	Thermal Conductivity of InAlAs	
	4.4		usion to Chapter 4	
			1	. –

Appendix

			Page
5		ermal Conductivity of III-V Superlattices (SLs): 3D RTA with Full persion	73
	5.1	Model Overview	74
	5.2	The Twofold Influence of Effective Interface Roughness	76
		5.2.1 Layer Thermal Conductivity	78
		5.2.2 Thermal Boundary Resistance	78
	5.3	Calculation of In-plane and Cross-plane Thermal Conductivities	80
	5.4	Results and Comparison with Experiments	81
		5.4.1 GaAs/AlAs Superlattices	81
		5.4.2 InGaAs/InAlAs Superlattices	86
	5.5	Conclusion to Chapter 5	87
6	Th	ermal Conductivity of III-V Bulk Materials: EMD	90
	6.1	Thermal Conductivity from Equilibrium Molecular Dynamics	91
		6.1.1 Quantum-Correction of Temperature	92
	6.2	Optimizing the Tersoff Potentials	93
		6.2.1 Tersoff Potentials	93
		6.2.2 Phonon Dispersion from EIP	96
		6.2.3 Parameter Optimization	97
		6.2.4 Optimized Potentials	98
	6.3	Thermal Conductivity of Ternary Alloy: The Role of Cation Mass Difference	101
	6.4	Thermal Conductivity of Ternary Alloy: The Role of Order	103
		6.4.1 Thermal Conductivity of Alloys Near A _{0.5} B _{0.5} C Composition with CuPt-	-
		B and CuAu-I order	103
		6.4.2 Thermal Conductivity of Alloys with Dierent Compositions and TPA	
		Order	107
	6.5	Conclusion to Chapter 6	107
\mathbf{A}	PPE	NDICES	
	App	endix A: Algorithm for Choosing Wave Vector	111
	App	endix B: Parameterization of Isotropic Dispersion Relation in III-V Binary	190
		Materials	120
T 1	CT (OF BEFERENCES	198

LIST OF TABLES

Tabl	e	Page
3.1	Force constants for 2D graphene in units of 10 N/m . The subscripts r , ti , and to refer to the radial, transverse in-plane, and transverse out-of-plane directions, respectively	23
4.1	Material parameters used in the calculation	63
5.1	Comparison of experimental results from Luckyanova <i>et al.</i> [1] and our calculated data for GaAs/AlAs SLs with layer thickness of 2 nm and 8 nm. In the calculation, we assume an interface rms roughness of 1.1 Å for the 2-nm system and 1.9 Å for the 8-nm one	86
6.1	Optimized parameters for the Albe-Tersoff potentials for AlAs and InAs. Parameters not listed are the same as in the original sets.[2, 3]	99
6.2	Comparison of calculated RT TC for $In_{0.5}Ga_{0.5}As$ and $In_{0.5}Al_{0.5}As$ with perfectly ordered CuPt-B and CuAu-I structure as well as the random alloy structure and the experimentally measured TC for $In_{0.53}Ga_{0.47}As[4]$ and $In_{0.52}Al_{0.48}As[5]$	104
6.3	Calculated RT TC for lattice-matched (LM) In _{0.53} Ga _{0.47} As and In _{0.52} Al _{0.48} As with various percentage of additional random disorder. Experimentally measured TC are also listed for comparison.[4, 5]	
A.1	Mapping rule of calculating the final group velocities $v_{\rm x}^{\rm final}$ and $v_{\rm y}^{\rm final}$ from the group velocities $v_{\rm x}$ and $v_{\rm y}$ in the irreducible wedge of the 1BZ according to the triangle index	
B.1	Fitting parameters for sound velocity and quadratic coefficient to get isotropic dispersion.	127

LIST OF FIGURES

Figu	ire	Page
1.1	A schematic of the hexagonal lattice, $ \mathbf{a_1} = \mathbf{a_2} , \theta = 120^{\circ}$	2
2.1	Flowchart of the PMC simulation. Transport kernel is inside the dashed box.	15
2.2	Simulation domain of NEMD method for extracting thermal conductivity using (a) fixed boundary conditions and (b) periodic boundary conditions	
2.3	Simulation domain of NEMD method for extracting thermal boundary resistance (from material 1 to material 2) using (a) fixed boundary conditions and (b) periodic boundary conditions	
3.1	Dispersion curves in the 1BZ for the TA, LA, ZA, TO, LO, and ZO phonon branches in single-layer graphene, calculated from the empirical dynamical matrix method including 4th nearest neighbors	
3.2	Phonon density of states (PDOS) for TA, LA, and ZA branches in graphene, calculated following the Gilat-Raubenheimer method.[6]	25
3.3	Flowchart showing the steps for generating a single phonon in the numerical ensemble of a cell at a given temperature. Dice indicate the use of random numbers	
3.4	Cumulative distribution function of phonon frequency at 300 K. The frequency range $\omega \in [0, 2.5 \times 10^{14}] \text{rad/s}$ was divided into $N_{\text{int}} = 2500$ equal intervals in the numerical calculation.	28
3.5	Schematic of the simulation domain of width W and length L . (Top) Armchair GNR. (Bottom) Zigzag GNR	
3.6	Illustration of the shadowing effect in treating boundary scattering in (a) arm-chair and (b) zigzag edges. By direct calculation, end-point location A is inside the ribbon. However, an edge-scattering event should have happened at point B and the real end-point location should be A'	

Figu	re	Page
3.7	A typical modified (post-scattering) CDF, Eq. (3.14), and the original CDF, Eq. (3.3), at 300 K	. 38
3.8	(Main panel) Normalized phonon distribution histogram in the ballistic transport regime compared with the Bose-Einstein distribution. The histogram is obtained by running the simulation with all the scattering mechanism turned off and recording the energies of all the phonons inside the GNR after the steady state is established; $T_{\rm h}=315~{\rm K}$ and $T_{\rm c}=285~{\rm K}$ in this case. The Bose-Einstein distribution is obtained based on temperature $T_{\rm ballistic}=301.12~{\rm K}$ inside the ribbon. (Inset) The calculated temperature profile inside the ribbon in the ballistic limit. The linear profile is also depicted for comparison	
3.9	A typical temperature profile along the ribbon in the quasiballistic transport regime. Here the temperature at two ends are $T_{\rm h}=315~{\rm K}$ and $T_{\rm c}=285~{\rm K}$ and the number of cells $N_{\rm c}=60.$	
3.10	Thermal conductivity of graphene for different lateral dimensions, as obtained by Chen <i>et al.</i> [7] in the circular geometry (symbols) and from our simulation in the rectangular GNR geometry (lines)	
3.11	Normalized cumulative distribution function of phonon mean free path for suspended graphene at 300 K. About 20% of phonons have a mean free path greater than 100 μ m	
3.12	Length-dependent thermal conductivity of wide GNRs at room temperature, obtained from the PMC simulation. Dashed line is a guide for the eye. (Inset) Comparison of normalized thermal conductivity from our simulation (red dots) and the experimentally obtained data of Xu et al.[8] The blue curve shows the thermal conductivity estimated with maximal contact resistance, the green one corresponds to the value with no contact resistance	
3.13	Thermal conductivity of graphene with different ¹³ C abundance as a function of temperature. Symbols represent the experimental data from Chen <i>et al.</i> [9] and lines show our PMC simulation results	
3.14	Thermal conductivity of graphene as a function of ¹³ C abundance at 380 K. Red squares show the experimental data from Chen <i>et al.</i> [9], green squares are the MD simulation results from the same paper, and blue diamonds correspond to the PMC simulation	

Appe Figu		Page
3.15	Thermal conductivity of $10-\mu$ m-long AGNRs (blue squares) and ZGNRs (green triangles) at 300 K as a function of GNR width, obtained from the PMC simulation. The red dashed line is the upper limit of thermal conductivity for the same length, calculated with a flat-edge GNR	
3.16	Thermal conductivity versus temperature for GNRs of width 500 nm (black), 200 nm (red), and 100 nm (blue) calculated based on PMC. For each width, we present data obtained with isotropic dispersion (open circles), as well as with full dispersion assuming the AGNR (solid squares) and ZGNR (solid triangles) ribbon orientation	
3.17	Thermal conductivity for suspended pristine bulk graphene from the PMC simulation (squares – armchair direction, triangles – zigzag direction) and the maximal thermal conductivity predicted by Dorgan et al[10]	
4.1	Thermal conductivity of bulk GaAs based on our calculation with full dispersion; $\gamma_{\text{TA}} = 0.57$, $\gamma_{\text{LA}} = 1.35$ (blue curve) and $\gamma_{\text{TA}} = 0.52$, $\gamma_{\text{LA}} = 1.30$ (red curve). The green curve shows the <i>ab initio</i> results from Lindsay <i>et al.</i> [11] The orange curve is an analytic fit to the experimental data of Evans <i>et al.</i> [12] The purple curve is the calculated thermal conductivity based on our model and with the isotropic dispersion approximation (see Appendix B). Blue circles, yellow triangles, and blue diamonds correspond to the experimental data from Inyushkin <i>et al.</i> ,[13] Carlson <i>et al.</i> ,[14] and Amith <i>et al.</i> ,[15] respectively	
4.2	Thermal conductivity of bulk AlAs based on our calculation with full dispersion. $\gamma_{\text{TA}} = 0.46$ and $\gamma_{\text{LA}} = 1.35$ (blue curve). In green, orange, and purple we show the <i>ab initio</i> data from Lindsay <i>et al.</i> ,[11] an analytic fit to the experimental data from Evans <i>et al.</i> ,[12] and the calculation with isotropic dispersion approximation (see Appendix B), respectively. The red symbol shows experimental data from Afromowitz.[16]	
4.3	Thermal conductivity of bulk InAs based on our calculation with full dispersion; $\gamma_{\text{TA}} = 0.56$, $\gamma_{\text{LA}} = 1.60$ (blue curve) and $\gamma_{\text{TA}} = 0.46$, $\gamma_{\text{LA}} = 1.35$ (red curve). The green curve shows the <i>ab initio</i> results from Lindsay <i>et al.</i> .[11] The purple curve shows the calculated thermal conductivity with the isotropic dispersion approximation (see Appendix B). Yellow triangles, brown circles, pink diamonds, and orange squares correspond to the experimental data from Heckman <i>et al.</i> ,[17] Tamarin <i>et al.</i> ,[18] Guillou <i>et al.</i> ,[19] and Bowers <i>et al.</i> ,[20] respectively	

Appe Figur		Page
4.4	Thermal conductivity of bulk $In_xGa_{1-x}As$ with varying In composition. The blue curve shows the theoretical results from Abeles.[21] The red curve and orange dots present the experimental results from Adachi[22] and Abrahams <i>et al.</i> ,[4] respectively. Purple diamonds represent the results of our calculation	69
4.5	Thermal conductivity of bulk $Al_xGa_{1-x}As$ with varying Al composition. Blue dots and red diamonds show the experimental data of Afromowitz <i>et al.</i> [16] and the results of our calculation, respectively	70
4.6	Thermal conductivity of bulk $In_xAl_{1-x}As$ with varying In composition from our calculation	72
5.1	Even between lattice-matched crystalline materials, there exist nonuniform transition layers that behave as an effective atomic-scale interface roughness with some rms roughness Δ . This effective interface roughness lead to phonon momentum randomization and to interface resistance in cross-plane transport	77
5.2	In-plane thermal conductivity of GaAs/AlAs superlattices as a function of layer thickness. Red dots are the experimental data from Yao [23] and blue diamonds are our calculated data with $\Delta=6\text{Å}.$	82
5.3	In-plane thermal conductivity of a GaAs/AlAs superlattice (layer thickness 70 nm) as a function of temperature. Red symbols show the experimental results of Yu et al.[24] and the blue curve shows the calculations from our model with $\Delta=3.7$ Å	83
5.4	Cross-plane thermal conductivity of GaAs/AlAs superlattices as a function of temperature. Blue circles, orange diamonds, and brown squares show the measured cross-plane thermal conductivity data for 40×40 , 25×25 , and 10×10 SLs from Capinski et al.[25] Grey stars are the cross-plane thermal conductivity data for for a 12×14 SL from Capinski and Maris.[26] The corresponding curves are calculated based on our model, with the effective rms roughness Δ denoted in the legend	85

Appe Figu	endix re	Page
5.5	Cross-plane thermal conductivity of $In_{0.53}Ga_{0.47}As/In_{0.52}Al_{0.48}As$ SLs as a function of the period length. The notation AmGn represents a SL structure with the InAlAs and InGaAs layer thicknesses of m and n nanometers, respectively. Blue diamonds show the experimental data from Sood $et~al.[27]$, green dots show our calculation with regular scattering rates, and red squares show the calculation results with artificially increased bulk rates for InAlAs. In both calculations, Δ is chosen to be 0.5 Å, in keeping with the perfect interface quality revealed in X-ray diffraction experiments	88
6.1	A typical mapping between the MD calculated temperature $T_{\rm MD}$ and the quantum corrected temperature $T_{\rm Q}$ (figure showing the case of GaAs). The two values converge at high temperatures and differ a great deal at low temperatures	
6.2	Temperature-dependent thermal conductivity, as calculated in this work with optimized potentials (dark green dots with error bars) and from experiments (light green solid lines) for AlAs,[12] GaAs,[13, 15] and InAs.[18, 19, 20] The insets show the calculated phonon dispersions (dashed lines) along the $\Gamma-X$ direction along with experimental values (dots).[11, 28, 29, 30]	100
6.3	Thermal conductivity as a function of In composition in $In_xGa_{1-x}As$ and $In_xAl_{1-x}As$	
6.4	The crystal structure of ordered ternary alloy $A_{0.5}B_{0.5}C$ with CuPt-B and CuAu-I ordering	105
6.5	A sample crystal structure of ordered ternary alloy $A_{0.5}B_{0.5}C$ with TPA ordering. The 3 planes in a period $(A_uB_{1-u}/A_vB_{1-v}/A_wB_{1-w})$ has configurations of $u=1,\ v=0,$ and $w=0.5.$	105
6.6	Calculated RT TC of InGaAs and InAlAs with perfect TPA ordering and various In compositions. Red squares and yellow dots show the results from the most-symmetric (MS) and least-symmetric (LS) structures. Experimental measurement 5] are shown in blue diamonds	-
A.1	Isoenergy curves in the 1BZ for TA-branch phonons. The neighboring curves are separated by 2×10^{13} rad/s and the shaded region in the black triangle is the irreducible wedge in the 1BZ.	112

	Appendix Figure	
A.2	A typical isoenergy curve ($\omega = 9 \times 10^{13} \text{ rad/s}$). The shaded area shows the irreducible wedge. Angle θ fixes a point at the curve and the associated wave vector \mathbf{q} and group velocity \mathbf{v}_g is shown	114
A.3	A typical normalized probability versus angle curve for phonon generation. Here the frequency level is at $\omega=3\times10^{13}$ rad/s in TA-branch	116
A.4	Twelve equivalent triangles in 1BZ numbered counter-clockwise	117
B.1	Typical phonon dispersion of ternary group III arsenide compound ($In_{0.53}Ga_{0.47}As$ along highly symmetric directions	
B.2	Comparison of the full dispersion with isotropic fit along [100] direction for $In_{0.53}Ga_{0.47}As.$	122
В.3	Comparison of the phonon DOS calculated from the full dispersion and the isotropic quadratic fit for ${\rm In}_{0.53}{\rm Ga}_{0.47}{\rm As}.$	123
B.4	Sound velocity of the quadratic fit to dispersion of InGaAs along [100] direction as a function of In composition	125
B.5	Quadratic term of the quadratic fit to dispersion of InGaAs along [100] direction as a function of In composition	126

ABSTRACT

With the advancement of nanofabrication techniques, the sizes of semiconductor electronic and optoelectronic devices keep decreasing while the operating speeds keep increasing. High-speed operation leads to more heat generation and puts more thermal stress on the devices. Since the heat conduction in semiconductors is dominated by the lattice (i.e., phonons), understanding phonon transport in nanostructures is essential to addressing and alleviating the thermal-stress problem in these modern devices.

In addition to the increased thermal stress, the advanced techniques that have allowed for the shrinking of the devices routinely rely on heterostructuring, doping, alloying, and the growth of intentionally strained layers to achieve the desired electronic and optical properties. These introduce impediments to phonon transport such as boundaries, interfaces, point defects (alloy atoms or dopants), and strain. Phonon transport is strongly affected by this nanoscale disorder. This dissertation examines how different types of disorder interact with phonons and degrade phonon transport.

First, we study thermal transport in graphene nanoribbons (GNRs). GNRs are quasione-dimensional (quasi-1D) systems where the edges (boundaries) play an important role in
reducing thermal conductivity. Additionally, the thermal transport in GNRs is anisotropic
and depend on the GNR's chirality (GNR orientation and edge termination). We use phonon
Monte Carlo (PMC) with full phonon dispersions to describe two highly-symmetric types of
GNRs: the armchair GNR (AGNR) and the zigzag GNR (ZGNR). PMC tracks phonon in
real space and we can explicitly include non-trivial edge structures. Moreover, the relatively

low computational burden of PMC allows us to simulate samples up to 100 μ m in length and predict an upper limit for thermal conductivity in graphene.

We then investigate the thermal conductivity in III-V superlattices (SLs). SLs consist of alternating thin layers of different materials and III-V SLs are widely used in nanoscale thermoelectric and optoelectronic devices. The key feature in SLs is that it contains many interfaces, which dictates thermal transport. As III-V SLs are often fabricated using well-controlled techniques and have high-quality interfaces, we develop a model with only one free parameter—the effective rms roughness of the interfaces—to describe its twofold influence: reducing the in-plane layer thermal conductivity and introducing thermal boundary resistance (TBR) in the cross-plane direction. Both the calculated in-plane and cross-plane thermal conductivity of SLs agree with a number of different experiments.

Finally, we study thermal conductivity of ternary III-V alloys. In modern optoelectronic devices, ternary III-V alloys are used more often than binary compounds because one can use composition engineering to achieve different effective masses, electron/hole barrier heights, and strain levels. Ternary alloys are usually treated under the virtual crystal approximation (VCA) where cation atoms are assumed to be randomly distributed and possess an averaged mass. This assumption is challenged by a discrepancy between different experiments, as well as the discrepancy between experiments and calculations. We use molecular dynamics (MD) to study the ternary alloy system as both atom masses and atom locations are explicitly tracked in MD. We discover that the thermal conductivity is determined by a competition between mass-difference scattering and the short-range ordering of the cations.

Chapter 1

Introduction

1.1 Phonons

1.1.1 Bravais Lattice and Reciprocal Lattice

In solid-state physics, a Bravais lattice is an infinite array of lattice points arranged periodically. In two-dimensional (2D) space, lattice sites can be generated by:

$$\mathbf{R} = n_1 \mathbf{a_1} + n_2 \mathbf{a_2},\tag{1.1}$$

where n_1 and n_2 are integers and $\mathbf{a_1}$ and $\mathbf{a_2}$ are called the primitive vectors of the lattice. The primitive vectors determine the primitive cell, which is the minimum unit repeated in the lattice. There are 5 different Bravais lattices in 2D, among which the hexagonal lattice is of great importance in solid-state physics since stable 2D materials such as graphene have this lattice structure. Figure 1.1 is showing the schematic of a hexagonal lattice with one atom at each lattice site. In a hexagonal lattice, the two primitive vectors have the same length ($|\mathbf{a_1}| = |\mathbf{a_2}|$) and the angle between them is 120° ($\theta = 120^{\circ}$).

In three-dimensional (3D) space, lattice sites are generated using 3 primitive vectors:

$$\mathbf{R} = n_1 \mathbf{a_1} + n_2 \mathbf{a_2} + n_3 \mathbf{a_3},\tag{1.2}$$

and there are 14 Bravais lattices. The 3D materials we focus on in this thesis all have the face-centered cubic (fcc) Bravais lattice.

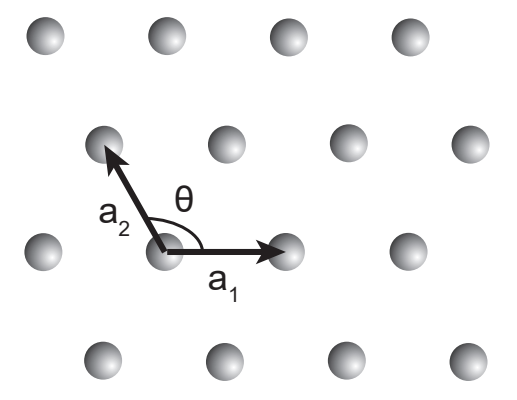


Figure 1.1: A schematic of the hexagonal lattice, $|\mathbf{a_1}| = |\mathbf{a_2}|, \theta = 120^{\circ}$.

Owing to the periodicity, it is useful to introduce the reciprocal lattice. In 3D, the primitive vectors of the reciprocal lattice is constructed as:

$$\mathbf{b_1} = 2\pi \frac{\mathbf{a_2} \times \mathbf{a_3}}{\mathbf{a_1} \cdot \mathbf{a_2} \times \mathbf{a_3}}; \qquad \mathbf{b_2} = 2\pi \frac{\mathbf{a_3} \times \mathbf{a_1}}{\mathbf{a_1} \cdot \mathbf{a_2} \times \mathbf{a_3}}; \qquad \mathbf{b_3} = 2\pi \frac{\mathbf{a_1} \times \mathbf{a_2}}{\mathbf{a_1} \cdot \mathbf{a_2} \times \mathbf{a_3}}. \tag{1.3}$$

A reciprocal lattice vector is of the form $\mathbf{G} = m_1 \mathbf{b_1} + m_2 \mathbf{b_2} + m_3 \mathbf{b_3}$ where m_1 , m_2 , and m_3 are integers. The Wigner-Seitz cell of the reciprocal lattice is known as the first Brillouin zone (1BZ) and all the physically significant wave vectors for elastic waves live in the 1BZ[31].

1.1.2 Lattice Waves and Phonon Dispersion

At finite temperatures, atoms vibrate about their equilibrium lattice. As the lattice is an elastic medium, the vibrations propagate and the material supports waves. Phonons are quanta of the normal modes of crystal wave excitations. For an atom in the crystal, its motion can be captured with Newton's second law of motion:

$$m_s \ddot{\mathbf{u}}_s = \sum_t \mathbf{K}^{st} (\mathbf{u_t} - \mathbf{u_s}),$$
 (1.4)

where $\mathbf{u_s}$ is the displacement of atom s and the sum is over all the neighboring atoms interacting with atom s with \mathbf{K}^{st} being the interaction force constant matrix between the two. Due to the underlying periodicity of the lattice, displacements have the form of a traveling plane wave:

$$\mathbf{u_s} = \mathbf{u_0} \exp(i\mathbf{q}\mathbf{R_s}) \exp(-i\omega(\mathbf{q})t),$$
 (1.5)

where \mathbf{q} and $\mathbf{R_s}$ are a vector from the 1BZ and a Bravais lattice vector, respectively. With the knowledge of all the force constant matrices, one can solve for the phonon dispersion relation $\omega(\mathbf{q})$.

Depending on the dimensionality of the physical system and the number of atoms per basis in the direct-space Bravais lattice, we get different number of branches for the dispersion relation. In a 3D crystal with 2 atoms per basis, there are $3 \times 2 = 6$ different branches, 3 acoustic branches and 3 optical branches. Among these there is 1 longitudinal acoustic (LA) branch, 1 longitudinal optical (LO) branch, 2 transverse acoustic (TA) branches, and 2 transverse optical (TO) branches.

From the phonon dispersion relation, one can extract the group velocity of a wave with wave vector \mathbf{q} from each branch b:

$$\mathbf{v}_{\mathrm{b},g} = \nabla_{\mathbf{q}} \omega_{\mathrm{b}}(\mathbf{q}). \tag{1.6}$$

The signature of an acoustic branch is often a linear dispersion as **q** approaches zero; the corresponding group velocity is referred to as the sound velocity in the material. On the other hand, optical branches are higher in energy and rather dispersionless compared to acoustic branches. Optical phonons carry large amount of energy while having small group velocities.

1.1.3 Phonon Distribution and Density of States (DOS)

Phonons are bosons and they follow the Bose-Einstein (BE) distribution in equilibrium

$$n_{\rm BE} = \frac{1}{\exp\left(\frac{\hbar\omega}{k_B T}\right) - 1},\tag{1.7}$$

where $\hbar \approx 1.05 \times 10^{-34}$ Js is the reduced Planck's constant, $k_B \approx 1.38 \times 10^{-23}$ J/K is the Boltzmann's constant, ω is the phonon angular frequency, and T is the temperature.

Since each phonon carries energy $\hbar\omega$, the average energy carried by a phonon mode is

$$\langle E \rangle = \hbar \omega \cdot n_{\text{BE}} = \frac{\hbar \omega}{\exp\left(\frac{\hbar \omega}{k_B T}\right) - 1},$$
 (1.8)

In a crystal, the density of states $(D(\omega)d\omega)$ measures the number of allowed sound modes in the frequency interval between ω and $\omega + d\omega$. The number can be obtained by enumerating the allowed reciprocal lattice vectors for phonons in the shell between the isoenergy surface ω and $\omega + d\omega$ in the dispersion relation:

$$D(\omega)d\omega = \frac{V}{(2\pi)^3} \int_{shell} d^3 \mathbf{q} = \frac{V}{(2\pi)^3} \int \frac{dS_\omega}{v_g(\mathbf{q})},$$
 (1.9)

where V is the volume of the physical system, S_{ω} is the area of the isoenergy surface, and $v_g(\mathbf{q})$ is the group velocity at each \mathbf{q} point. The DOS can be obtained analytically with some approximation of the dispersion relation, but is often obtained numerically in the realistic full-dispersion case.

1.2 Thermal Conductivity in Semiconductor Nanostructures

1.2.1 Fourier's Law

Thermal conductivity, often denoted with κ , quantifies the ability of a material to conduct heat. In solids, heat conduction is mediated by phonons or free electrons. In SI units, thermal conductivity is measured in watts per meter-kelvin (W/m·K). In experiments, thermal conductivity is primarily evaluated from the Fourier's law:

$$\mathbf{j_q} = -\kappa \nabla_{\mathbf{r}} T, \tag{1.10}$$

where $\mathbf{j_q}$ is the flux of thermal energy. The temperature gradient in the equation implies that the thermal energy transfer is a diffusive process and that κ is in general a tensor. Furthermore, the thermal conductivity tensor at a given temperature is in general an intrinsic property of the material.

In most bulk materials, thermal transport is isotropic, meaning the thermal conductivity has the same value along different directions. However, in nanostructures, the thermal transport can be anisotropic, and we often address the thermal conductivities along different directions separately. As a result, Fourier's law is often applied in its one-dimensional (1D)

form:

$$j_{qx} = -\kappa \frac{dT}{dx},\tag{1.11}$$

where x is the direction along which the thermal conductivity is measured.

In undoped or lightly doped semiconductors, the population of free electrons is small and the heat conduction is dominated by phonons. More specifically, heat flux is mainly carried by acoustic phonons as optical phonons are less excited (due to large energy) and less mobile (small group velocity). In this thesis, we only consider the acoustic phonon contribution to thermal conductivity and ignore electrons and optical phonons. In some special circumstances optical phonons can become important, and we will discuss it in more details then.

With increasing interests on measuring the thermal conductivity of nanostructures, Fourier's law has been generalized to non-diffusive regimes to calculate "size-dependent thermal conductivity." If the size of a nanostructure is smaller than the carrier mean free path (MFP) λ , thermal transport inside the structure is partially ballistic, and thermal conductivity extracted from Fourier's law increases with the structure size. In this generalized notation, a size-independent thermal conductivity calculated from Fourier's law indicates diffusive thermal transport while a size-dependent thermal conductivity is a signature of ballistic transport.

1.2.2 Phonon Scattering

As mentioned in Sec. 1.2.1, phonon transport on a large scale is a diffusive process rather than a ballistic one, and the main mechanisms of relaxing phonon momentum are scattering with structural imperfections and scattering with other phonons. The former arises from imperfections in the lattice; it is especially important in nanostructures where rough edges or interfaces can pose great resistance to thermal transport. Previously when we introduced the phonon dispersion relation, an implicit assumption is that the interatomic potential an atom feels is harmonic, or goes to as high as the second order in displacement. However, in

reality, an interatomic potential can be expanded as [32]

$$U(\mathbf{R} + \mathbf{dr}) = U(\mathbf{R}) + \mathbf{dr} \cdot \nabla U(\mathbf{R}) + \frac{1}{2!} (\mathbf{dr} \cdot \nabla)^2 U(\mathbf{R}) + \frac{1}{3!} (\mathbf{dr} \cdot \nabla)^3 U(\mathbf{R}) + \cdots, \quad (1.12)$$

where **R** is the equilibrium position and all terms with the third-order or higher in displacement represent anharmonicity. Due to this anharmonicity, phonons with different wave vectors can collide with each other and change momentum. The dominant form of phonon-phonon scattering is the three-phonon process where two incoming phonons collide and scatter into one outgoing phonon or one incoming phonon scatters into two outgoing phonons. There are two processes for three-phonon scattering, the normal (N) process and the Umklapp (U) process.

Take the case where two phonons scatter into one as an example. In the N process, both the phonon momentum and the phonon energy are conserved

$$\begin{cases} \mathbf{q_1} + \mathbf{q_2} &= \mathbf{q_3}, \\ \omega_1 + \omega_2 &= \omega_3, \end{cases}$$
 (1.13)

where ω_i represent phonon frequencies and $\mathbf{q_i}$ are wave vectors in the 1BZ. As a result of the momentum and energy conservation, the phonon flux is unchanged before and after the scattering event, thus the thermal resistivity from the N process is zero.[31]

On the other hand, U processes conserve energy exactly and momentum up to a reciprocal lattice vector

$$\begin{cases} \mathbf{q_1} + \mathbf{q_2} &= \mathbf{q_3} + \mathbf{G}, \\ \omega_1 + \omega_2 &= \omega_3, \end{cases}$$
 (1.14)

where G can be any reciprocal lattice vector. Due to the nonzero G, the phonon flux will change after the scattering event, leading to thermal resistance.

1.3 Phonon Transport

As heat is mainly carried by phonons, modeling thermal conductivity in bulk materials and their nanostructures depends on studying the phonon transport inside the structure. In different environments, phonon transport can be coherent (wavelike) or incoherent (particle-like) or partially coherent which is somewhere in between.

1.3.1 Coherent Phonon Transport

In the coherent transport regime, phonons behave like waves, meaning phonons can survive a long time traveling inside the material without suffering any phase-changing scattering events, thus able to maintain wave behavior. To observe this, one must minimize phonon scattering by using very pure materials and low temperatures. Because of the wave nature, a signature of coherent phonon transport is linear dependence of thermal conductivity on the sample size.

Here we talk about coherent phonon transport in the context of superlattices (SLs) consisting of periodic alternating layers. The interfaces between neighboring layers have been believed to destroy phonon coherence completely[33], making the cross-plane thermal conductivity of SLs independent of the number of period in the SL. The first experimental evidence of coherent phonon transport across SL interface was reported in 2012 by Luckyanova et al. [34] in a GaAs/AlAs superlattice over the temperature range of 30 to 150 kelvin.

Modeling coherent phonon transport requires a method that is able to capture its wave nature.

1.3.2 Semiclassical Phonon Transport

In the semiclassical transport regime, phonons behave like (classical) particles due to frequent scattering events. This typically holds for thermal transport at high temperatures (room temperature or higher) or in nanostructures with a lot of boundary roughness in it.

In this picture, we can assume phonons are pointlike particles and we can know its location and momentum at the same time. Transport is governed by the phonon Boltzmann

transport equation (pBTE)

$$\frac{\partial n_{\rm b}(\mathbf{r}, \mathbf{q}, t)}{\partial t} + \mathbf{v}_{\rm b, \mathbf{q}} \cdot \nabla_{\mathbf{r}} n_{\rm b}(\mathbf{r}, \mathbf{q}, t) = \left. \frac{\partial n_{\rm b}(\mathbf{r}, \mathbf{q}, t)}{\partial t} \right|_{\rm scat}.$$
 (1.15)

Here, $n_{\rm b}({\bf r},{\bf q},t)$ is the time-dependent phase space distribution of the phonons in branch b and ${\bf v}_{\rm b,{\bf q}} = \nabla_{\bf q}\omega_{\rm b,{\bf q}}$ is the phonon group velocity. The means by which a phonon can leave its current phase space location is drifting to a new location (second term on the left) or scatter into a different momentum (term on the right). Modeling thermal conductivity in the semiclassical regime often involves solving the pBTE under some approximations.

1.3.3 Phonon Transport in Semiconductor Nanostructures

As Moore's law predicts, the size of semiconductor devices keeps decreasing while increasing the operation speed and frequency keep increasing. The thermal stress devices face are more severe than ever. The advanced techniques that allowed the shrinking of the devices [35, 36] routinely rely on heterostructuring, doping, alloying, and the growth of intentionally strained layers to achieve the desired electronic and optical properties. At the same time, nanoscale imperfections such as boundaries, interfaces, point defects, and strain are inevitably introduced and will all impact the thermal transport in these devices. In order to address the thermal stress problem in nanoscale devices, it is essential to study the thermal transport in nanostructures, especially in the presence of these disorders.

1.4 Overview of This Dissertation

Three projects under the umbrella of semiclassical simulation of thermal transport in semiconductor nanostructures are discussed in this thesis:

- 1. Two-dimensional (2D) Phonon Monte Carlo (PMC) simulation of thermal conductivity of graphene nanoribbons (GNRs) using full phonon dispersion.
- 2. Thermal conductivity of III-V superlattices (SLs).

- (a) Bulk thermal conductivity of III-V compound semiconductors from solving the phonon Boltzmann transport equation (PBTE) under the relaxation time approximation (RTA) using full phonon dispersion.
- (b) Thermal boundary resistance (TBR) from interpolating between the acoustic mismatch model (AMM) and the diffusive mismatch model (DMM) with a single free parameter.
- 3. Molecular dynamics (MD) simulation of thermal conductivity in III-V ternary alloys.

1.4.1 Organization of Chapters

In Chapter 2, we provide a brief introduction to all the simulation techniques used to predict thermal conductivity in this work, i.e., solving the PBTE under the RTA, solving the PBTE with the PMC method, and obtaining thermal conductivity through MD simulations.

In Chapter 3, we present the 2D PMC simulation of GNRs with full phonon dispersion. We discuss in detail the implementation of the algorithm to generate and scatter phonons according to the full phonon dispersion. We address the special concern of conserving energy inside the simulation domain. We validate the simulation technique by benchmarking the results against a number of experiments. We predict an upper limit of thermal conductivity in graphene and conclude samples larger than 100 μ m in size are needed to observe the limit.

Chapter 4 introduces the model for bulk thermal conductivity of III-V compound semiconductors and their ternary alloys. Here we solve the PBTE under the RTA together with the full phonon dispersion. We present the scattering rates as well as all the parameters used in the model. We show the calculated temperature-dependent thermal conductivity of binary compounds in comparison with experimental data. We calculate the thermal conductivity of ternary alloys AlGaAs, InGaAs, and InAlAs under the virtual crystal approximation (VCA) at room temperature (RT) and compare with experiments.

Chapter 5 builds on Chapter 4 and presents a model for describing thermal conductivity in III-V superlattices (SL) with just one free parameter–effective interface roughness Δ

between layers. We discuss the twofold influence the interface roughness has on the thermal transport, along both in-plane and cross-plane directions. We show the formula for calculating thermal conductivity and results for multiple GaAs/AlAs SLs and InGaAs/InAlAs superlattice (SL) structures. We also comment on the agreement with existing experiments and the discrepancies which inspired further investigation.

Chapter 6 summarizes the process of modeling thermal conductivity of III-V ternary alloys using equilibrium molecular dynamics (EMD). We present the process of optimizing the Tersoff interactive potential for binary III-As compounds and apply them to ternary alloys. We explore the competing influence mass-difference scattering and short-range order have on the thermal conductivity of ternary alloys.

1.4.2 Research Accomplishments

The work presented in this thesis are based on three published peer-reviewed journal papers (Mei et al., 2014; Mei and Knezevic, 2015; Mei et al., 2017)[37, 38, 39], one submitted journal paper (Mei and Knezevic, 2017)[40], three conference presentations (Mei et al., 2014; Mei, Aksamija, and Knezevic, 2015; Mei and Knezevic, 2017), and one book chapter (Maurer, Mei, and Knezevic, 2017)[41].

During the PhD study, the author also worked on electrothermal simulation of quantum cascade lasers (QCLs), which is not included in this thesis. That work resulted in two peer-reviewed journal paper (Jonasson, Mei, et al., 2015; Shi, Mei, et al., 2017)[42, 43], one conference presentation (Shi, Mei, and Knezevic, 2015), and one book chapter (Mei, et al., 2017)[44].

Ongoing projects include combined experimental and theoretical characterization of thermal conductivity in InAlAs that is lattice-matched to InP ($In_{0.52}Al_{0.48}As$) and electrothermal simulation of QCL in the density matrix formalism. These projects will yield two peer-reviewed journal papers.

Chapter 2

Semiclassical Techniques for Predicting Thermal Conductivity

In this chapter, we will briefly survey a few semiclassical simulation techniques commonly used to calculate thermal conductivity. We are focusing on the techniques utilized in this thesis to facilitate the understanding of following chapters.

One avenue to predicting thermal conductivity starts from the phonon Boltzmann transport equation (PBTE) (Equation 1.15) in a steady state. In general, the PBTE cannot be solved analytically because of the scattering term. With the help of powerful computers, we can solve the PBTE numerically using both deterministic and stochastic approaches. Short of resorting to large scale computations, various of approximations can be made to the scattering term in order to solve the PBTE, the relaxation time approximation (RTA) is the most common and successful one. Phonon Monte Carlo (PMC) treats the scattering term stochastically by using random numbers to determine scattering events.

Another popular branch of techniques is based on molecular dynamics (MD) simulations. In an MD simulation, a set of atoms are tracked in real space with initial positions and momenta. The motion of the atoms are governed by the Newton's second law while the forces applied to atoms are captured using some empirical interatomic potential. Thermal conductivity can be extracted from both an equilibrium MD (EMD, the whole system is at the same temperature and no macroscopic flux flows) via the fluctuation-dissipation theorem or an nonequilibrium MD (NEMD) via the Fourier's law.

2.1 The Relaxation Time Approximation (RTA)

At steady state, in the presence of thermal gradient, the PBTE becomes

$$\mathbf{v}_{\mathrm{b},\mathbf{q}} \cdot \nabla_{\mathbf{r}} T \frac{\partial n_{\mathrm{b}}(\mathbf{r}, \mathbf{q}, t)}{\partial T} = \left. \frac{\partial n_{\mathrm{b}}(\mathbf{r}, \mathbf{q}, t)}{\partial t} \right|_{\mathrm{scat}}.$$
 (2.1)

In the case of a small temperature gradient, PBTE can be linearized by assuming the phonons mainly follows the equilibrium BE distribution with only a small correction:

$$n_{\rm b}(\mathbf{r}, \mathbf{q}, t) = n_{\rm BE}(\omega_{\rm b, \mathbf{q}}, T_{\mathbf{r}}) + n_{\rm b}'(\mathbf{r}, \mathbf{q}, t). \tag{2.2}$$

Here $n'_{\rm b}({\bf r},{\bf q},t)$ describes the small deviation from the equilibrium distribution. It is worth noting that this deviation alone brings the thermal transport since the equilibrium distribution is symmetric with respect to the wave vector ${\bf q}$ and will lead to zero heat flux. Under the RTA, it is assumed that the rate at which phonon distribution changes due to scattering is proportional to its deviation from equilibrium through a constant relaxation rate

$$\frac{\partial n_{\rm b}(\mathbf{r}, \mathbf{q}, t)}{\partial t} \bigg|_{\rm scat} \approx \frac{n'_{\rm b}(\mathbf{r}, \mathbf{q}, t)}{\tau_{\rm b, q}}.$$
 (2.3)

Here the relaxation rate $\tau_{b,\mathbf{q}}^{-1}$ is often defined as a combined rate of all possible scattering mechanisms

$$\tau_{\mathbf{b},\mathbf{q}}^{-1} = \sum_{i} \tau_{\mathbf{b},\mathbf{q},i}^{-1}.$$
 (2.4)

To calculate thermal conductivity along a certain direction, we further reduce the PBTE to an 1D equation. Substituting Eq. (2.3) to the reduced PBTE, we obtain

$$\mathbf{v}_{\mathrm{b},\mathbf{q}} \cdot \hat{\mathbf{x}} \frac{\Delta T}{L} \frac{\partial n_{\mathrm{BE}}(\omega_{\mathrm{b},\mathbf{q}}, T)}{\partial T} = \frac{n_{\mathrm{b}}'(\mathbf{r}, \mathbf{q})}{\tau_{\mathrm{b},\mathbf{q}}}, \tag{2.5}$$

Here $\hat{\mathbf{x}}$ is the unit vector along the temperature gradient direction, ΔT is the temperature difference between the two ends separated by length L. Note we assume a constant temperature and the equilibrium distribution in the derivative part on the left hand side because of the small gradient. Heat flux is then calculated from

$$\mathbf{j}_{\mathbf{q}} = \frac{1}{V} \sum_{\mathbf{b}, \mathbf{q}} n_{\mathbf{b}}(\mathbf{r}, \mathbf{q}) \hbar \omega_{\mathbf{b}, \mathbf{q}} \mathbf{v}_{\mathbf{b}, \mathbf{q}} \cdot \hat{\mathbf{x}}$$

$$= \frac{1}{V} \sum_{\mathbf{b}, \mathbf{q}} n'_{\mathbf{b}}(\mathbf{r}, \mathbf{q}) \hbar \omega_{\mathbf{b}, \mathbf{q}} \mathbf{v}_{\mathbf{b}, \mathbf{q}} \cdot \hat{\mathbf{x}}$$

$$= \frac{1}{V} \sum_{\mathbf{b}, \mathbf{q}} \tau_{\mathbf{b}, \mathbf{q}} \hbar \omega_{\mathbf{b}, \mathbf{q}} (\mathbf{v}_{\mathbf{b}, \mathbf{q}} \cdot \hat{\mathbf{x}})^{2} \frac{\partial n_{\mathrm{BE}}(\omega_{\mathbf{b}, \mathbf{q}}, T)}{\partial T} \frac{\Delta T}{L}.$$
(2.6)

Comparing Eq. (2.6) with Eq. (1.10), thermal conductivity can be evaluated as

$$\kappa = \frac{1}{V} \sum_{\mathbf{b}, \mathbf{q}} \tau_{\mathbf{b}, \mathbf{q}} \hbar \omega_{\mathbf{b}, \mathbf{q}} \left(\mathbf{v}_{\mathbf{b}, \mathbf{q}} \cdot \hat{\mathbf{x}} \right)^2 \frac{\partial n_{\mathrm{BE}}(\omega_{\mathbf{b}, \mathbf{q}}, T)}{\partial T}.$$
 (2.7)

Here the term $\hbar\omega_{\mathbf{b},\mathbf{q}}\frac{\partial n_{\mathrm{BE}}(\omega_{\mathbf{b},\mathbf{q}},T)}{\partial T}$ is also known as the specific heat capacity for the phonon branch and wave vector.

2.2 Phonon Monte Carlo (PMC)

Monte Carlo (MC) methods use computer-generated random numbers to simulate a complicated system and obtain statistical results. PMC uses MC to treat the scattering term in the PBTE. PMC is a semiclassical method as in that phonons are point-like and have specific locations as well as momenta. An ensemble of phonons with certain distribution are tracked in real space in the simulation domain: they drift according to their group velocity, they reflect from domain boundaries when they reach them, and they encounter scattering events according to their scattering probabilities. Two ends of the simulation domain are connected to slightly different heat baths to develop a temperature gradient as well as heat flux inside the domain. Thermal conductivity is then extracted from the 1D Fourier's law. Considering the setup, the typical simulation domain in PMC is a cuboid (in 3D) or a rectangle (in 2D). An advantage with PMC is it is straight forward to include nontrivial geometries to these simulation domain such as edge structures or internal defects.

In terms of simulation capability, PMC is a middle ground between the simplistic RTA and the complicated full atomistic simulations. With the stochastic treatment of scattering events, PMC provides a much more realistic description of phonon transport than the RTA

and thus gives more accurate results. Further, the geometry of the structure can be treated explicitly rather than phenomenologically as in RTA. On the other hand, without describing explicitly and being limited by the underlying lattice of the material, PMC can simulate relatively large ($\sim \mu \text{m}$ in size) without too much computational burden. In the phonon ensemble, a simulation particle can represent multiple phonons, which further reduces the storage and computation requirements.

In PMC, the phonon ensemble evolves according to the PBTE with time discretized into small steps. The phase space distribution $n_{\rm b}(\mathbf{r},\mathbf{q},t)$ is obtained from a snapshot of the histogram at a certain time step. The initial distribution is often assigned as the equilibrium one $n_{\rm BE}(\omega_{\rm b,q},T)$ since we are again not too far from equilibrium. At each step, phonon drift with their group velocities, which are obtained from their dispersion relations. Phonons can then scatter and change accordingly at the end of each step. The drift-and-scatter loop continues until the end of the simulation. Figure 2.1 shows a typical PMC simulation flow where the dashed box encloses the transport kernel.

To implement PMC as shown in Fig 2.1, a few things need to be considered. First and foremost, this scheme implicitly assumes that phonons will encounter at most 1 scattering event in a step and scatter always comes at the end of the step. Both these assumptions require the time step to be sufficiently small (relative to the typical phonon relaxation time) to be valid. Secondly, one need the knowledge of phonon dispersion relation and phonon DOS for the branches of interest to calculate the proper group velocities and generate the initial equilibrium distribution. Usually only acoustic phonon branches are included in PMC and an isotropic approximation to the dispersion can be adopted to simplify the simulation. [45, 46] When phonon transport is anisotropic, full dispersion needs to be considered to capture the special behavior. [47, 37] The reinitialization step is added here in an effort to conserve energy on an average sense without violating the phonon distribution. Last but not the least, one need to come up with some criterion to terminate the simulation. Because of the stochastic nature of the method, any result from PMC needs to be averaged over some period of time

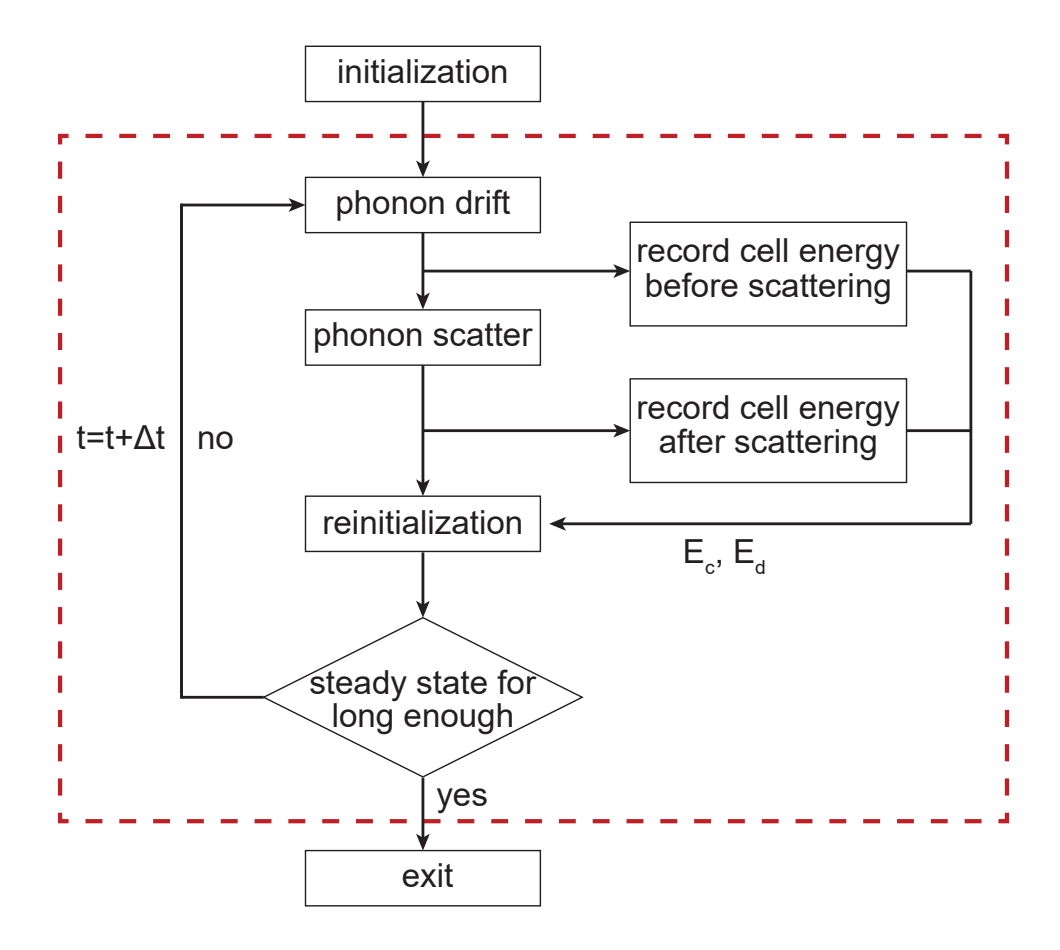


Figure 2.1: Flowchart of the PMC simulation. Transport kernel is inside the dashed box.

after the system reaches steady state. A detailed implementation of a 2D PMC with full dispersion is described in Sec. 3.

2.3 Molecular Dynamics (MD)

Molecular dynamics (MD) is a classical atomistic simulation technique where the atoms making up a material are explicitly tracked in real space. In semiconducting materials where phonons dominate the thermal transport, it is suitable to use MD to describe thermal transport at a finite temperature. In a MD simulation, time is also discretized into small steps. The size of the step should preferably be larger to allow for the capability of longer simulation; on the other hand, it also needs to be small enough for the system properties to converge. The trajectory of an atom is predicted with an empirical interatomic potential (EIP), which has an analytical form. The most simple interatomic potentials accounts for only two-body interaction while more sophisticated potentials can include many-body interactions. The choice of potential ultimately dictates all results obtained from a MD simulation because everything depends on it: the minimum point in the potential determines the equilibrium lattice constant and the cohesive energy, the gradient of the potential gives the force applied to an atom, the second derivative of the potential governs the phonon dispersion, and higher orders derivatives of the potential describes the anharmonicity in the material. As a result, it is important to choose a potential that at is accurate at least up to the 3rd order to accurately describe thermal conductivity using MD.

Given that we have chosen a proper potential, there are two main techniques to predict thermal conductivity using MD. The equilibrium MD (EMD) approach keeps the system equilibrated at the given temperature and uses the Green-Kubo (GK) formula to predict thermal conductivity depending on how fast instantaneous heat fluctuations dissipates in the system. In a 3D isotropic case,

$$\kappa = \frac{1}{k_B V T^2} \int_0^\infty \frac{\langle \mathbf{S}(t) \mathbf{S}(0) \rangle}{3} dt, \tag{2.8}$$

where $\mathbf{S}(t)$ is the instantaneous heat flux calculated from atom velocities and local potentials and $\langle \mathbf{S}(t)\mathbf{S}(0)\rangle$ is the heat flux autocorrelation function (HFACF). In anisotropic cases, thermal conductivity along certain directions can be calculated from the HFACF along that direction.

The non-equilibrium (NEMD) approach has a similar simulation domain to that of PMC. Two ends of the simulation domain are equilibrated at slightly different temperatures to induce a temperature gradient and a macroscopic heat flux. The Fourier's law (Eq. (1.10)) is then applied to extract the thermal conductivity along the direction where heat is flowing. Since the Fourier's law is directly used in predicting thermal conductivity, NEMD is also referred to as the direct method. In implementing NEMD, one can either impose temperature difference to induce heat flux or impose heat flux to induce temperature difference, the latter is also sometimes referred to as the reverse NEMD (RNEMD). Figure 2.2 describes the typical simulation domain of NEMD with fixed and periodic boundary conditions in 3D.

Apart from predicting bulk thermal conductivity, NEMD is also capable of predicting thermal boundary resistance (TBR). Figure 2.3 depicts a typical simulation domain for extracting TBR. At steady state, heat flows from material 1 to material 2 and there will be an abrupt temperature drop at the interface between two materials because of the TBR. With the knowledge of temperature drop ΔT and the heat flux j_q , TBR can then be calculated from

$$R_q = \frac{\Delta T}{j_q}. (2.9)$$

Compared to other techniques to describe TBRs, NEMD method has the advantage that one can explicitly add structure such as atom mixing or roughness to the interface easily. This is very important to study the behavior of realistic interfaces.

As has briefly touched on previously, two main drawbacks of using MD for thermal transport are: (1) the quality of the results depend on the quality of the choice of interatomic potential and (2) size of the simulation domain is small as limited by the number of atoms, thus size effect might emerge. In EMD, the size effect primarily comes from the fact that the system does not support phonon modes with wavelength longer than twice the system size,

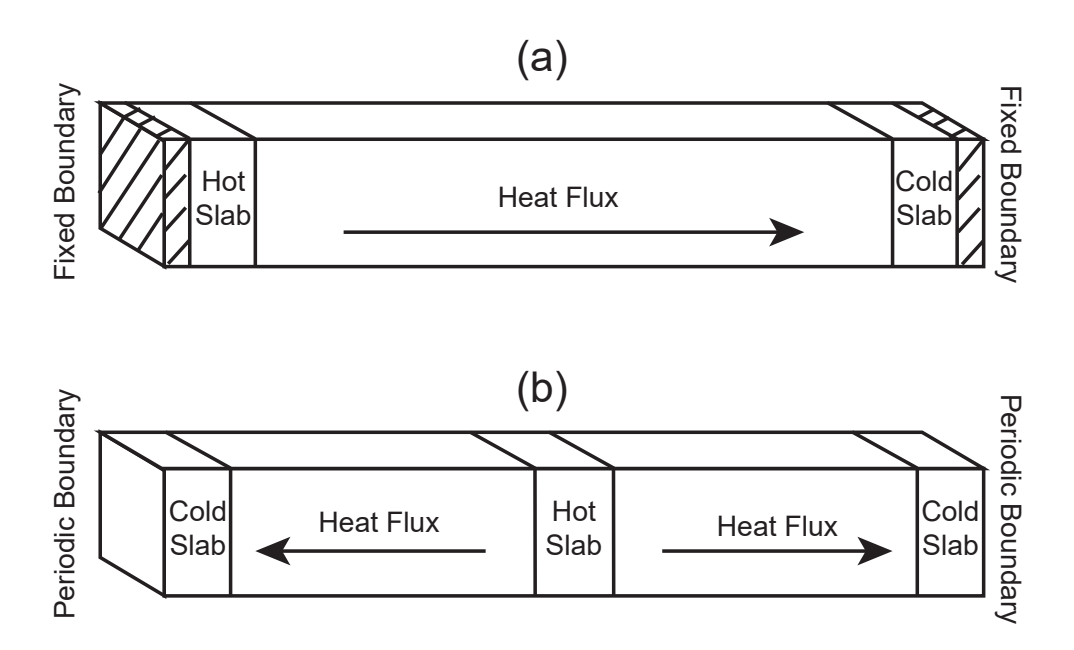


Figure 2.2: Simulation domain of NEMD method for extracting thermal conductivity using (a) fixed boundary conditions and (b) periodic boundary conditions.

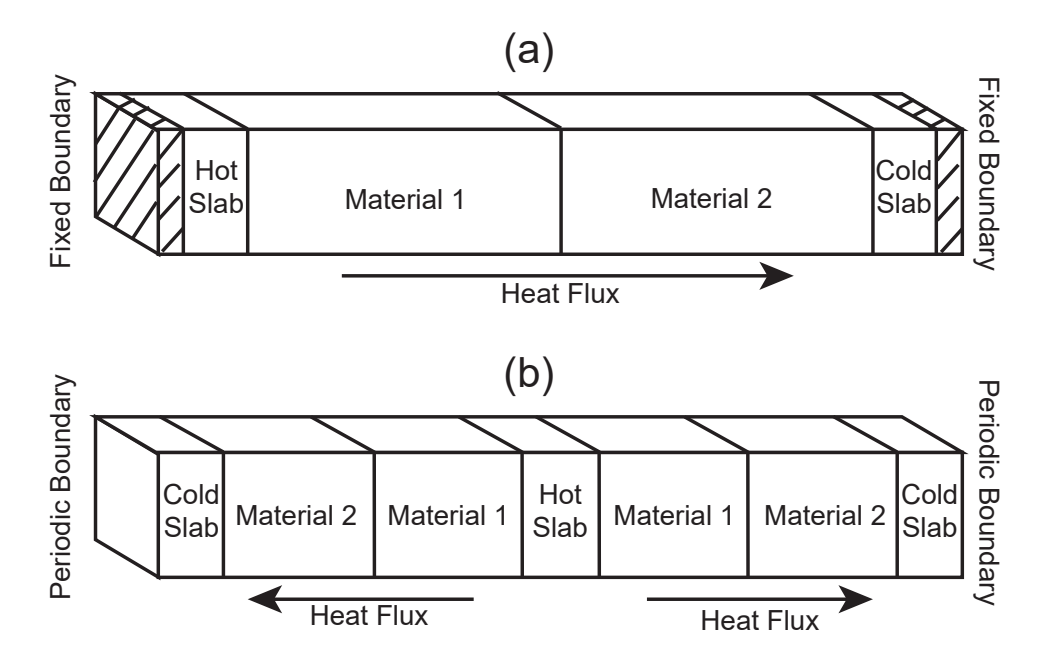


Figure 2.3: Simulation domain of NEMD method for extracting thermal boundary resistance (from material 1 to material 2) using (a) fixed boundary conditions and (b) periodic boundary conditions.

thus the contribution from these phonons are cutoff. In NEMD, on the other hand, the size effect is likely the result of partial ballistic thermal transport along the heat flux direction. A lot of effort has been devoted to developing potentials that accurately capture the thermal properties and eliminating size effects in both EMD and NEMD simulations. The thesis has more details on these in Sec. 1.

Chapter 3

Thermal Conductivity of Graphene Nanoribbons (GNRs): 2D PMC with Full Dispersion

This chapter details the 2D PMC solver we developed to extract thermal conductivity in 2D materials with anisotropic thermal transport properties. While we use graphene nanoribbons (GNRs) as the sample system, the technique developed here is suitable for any 2D material whose thermal transport is largely semiclassical [48, 49]. The contents of this chapter closely resemble Ref. [37].

3.1 Phonon Properties of Graphene

A main purpose of this work is to accurately describe the size-dependent thermal conductivity of graphene measured in experiment by Chen *et al.*[7, 9] and Xu *et al.*[8] in experiments. As a result, we are interested in GNRs on the larger side where the confinement has little influence on phonon properties. To simplify things without losing accuracy, we use the phonon properties of bulk graphene in the simulation.

3.1.1 Phonon Dispersion with Dynamical Matrix Method

Phonon dispersion relation of graphene is accurately captured with the empirical dynamical matrix method including fourth-nearest-neighbors (4NN) proposed by Saito *et al.*[50]. Recall Eq. (1.4) and Eq. (1.5) for describing the atom motion and displacement. Although

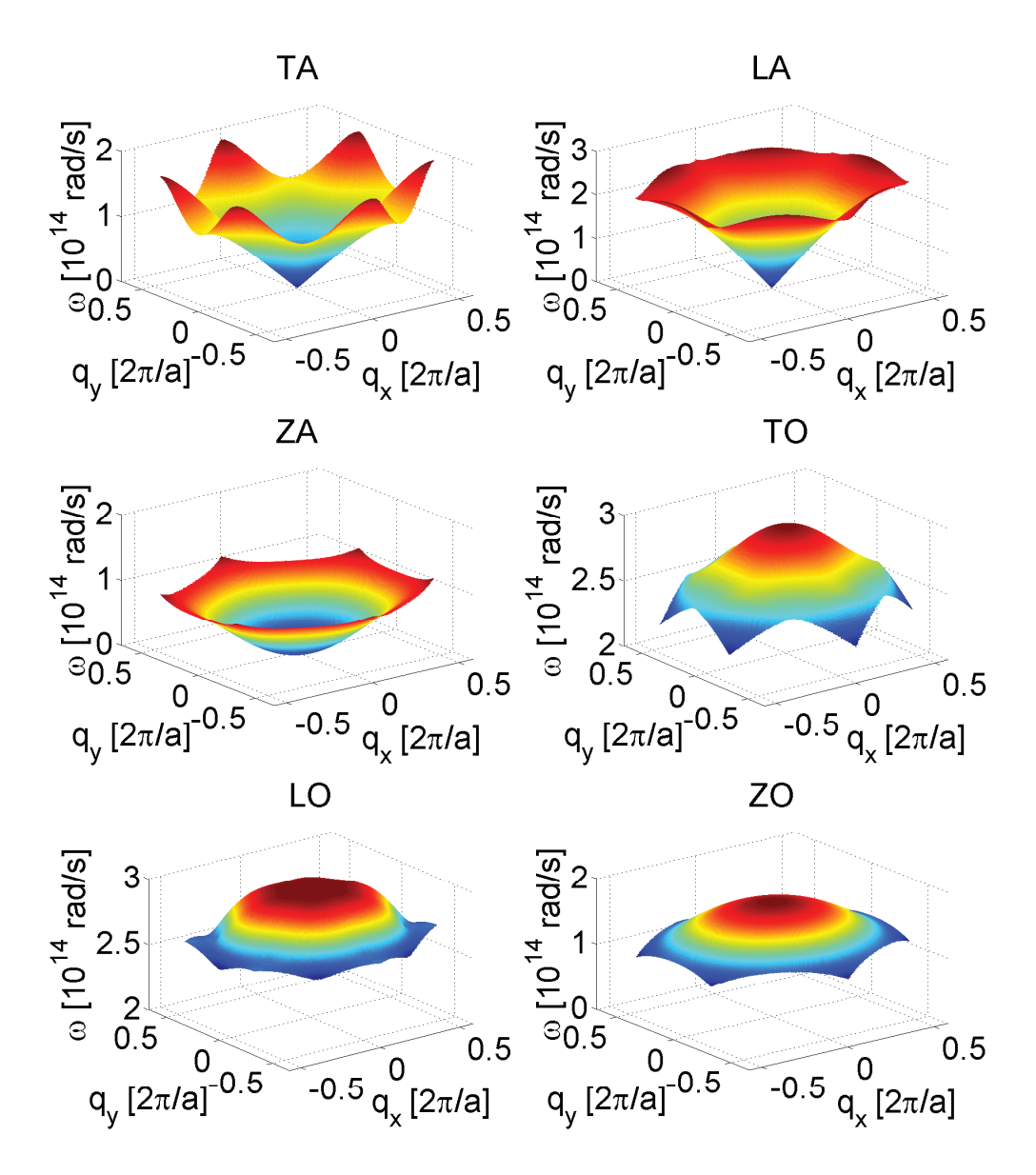


Figure 3.1: Dispersion curves in the 1BZ for the TA, LA, ZA, TO, LO, and ZO phonon branches in single-layer graphene, calculated from the empirical dynamical matrix method including 4th nearest neighbors.

Radial	In-plane	Out-of-plane
$\phi_r^{(1)} = 41.800$	$\phi_{ti}^{(1)} = 15.200$	$\phi_{to}^{(1)} = 10.200$
$\phi_r^{(2)} = 7.600$	$\phi_{ti}^{(2)} = -4.350$	$\phi_{to}^{(2)} = -1.080$
$\phi_r^{(3)} = -0.150$	$\phi_{ti}^{(3)} = 3.390$	$\phi_{to}^{(3)} = 0.995$
$\phi_r^{(4)} = 0.690$	$\phi_{ti}^{(4)} = -0.190$	$\phi_{to}^{(4)} = -0.550$

Table 3.1: Force constants for 2D graphene in units of 10 N/m. The subscripts r, ti, and to refer to the radial, transverse in-plane, and transverse out-of-plane directions, respectively.

graphene is a 2D material, atoms in suspended graphene can move along the direction perpendicular to the graphene plane. The force constants for radial, transverse in-plane, and transverse out-of-plane directions for the *n*th nearest neighbor $(\phi_r^{(n)}, \phi_{ti}^{(n)}, \text{ and } \phi_{to}^{(n)}, \text{ respectively})$ are given in Table 3.1.[50] As there are two atoms per basis in graphene, we get 6 phonon branches. Apart from the typical TA, LA, TO, and LO branches, the out-of-plane modes are given special names as the flexural acoustic (ZA) and the flexural optical (ZO) modes to signify that the motion is perpendicular to graphene plane. Figure 3.1 displays all 6 branches obtained from our calculation in the 1BZ. As can be confirmed, optical branches have higher energy and are relatively dispersionless, thus making negligible contributions to the thermal conductivity. One other observation is that ZA branch behaves differently than TA or LA branch (or any other typical acoustic branch): instead of having a linear dispersion close to the Γ point ($\mathbf{q} = 0$), ZA branch has a quadratic dispersion. This behavior origins from the fact that it is associated with motion along the direction where the lattice does not extend. The direct result of this is a reduced sound velocity for ZA phonons and a large DOS near zero energy (details in Sec. 3.1.2).

3.1.2 Phonon DOS from Full Dispersion

In a 2D reciprocal lattice, Eq. (1.9) reduces to

$$D_{\rm b}(\omega)d\omega = \frac{1}{(2\pi)^2} \int \frac{dL_{\rm b,\omega}}{v_{\rm b,g}(\mathbf{q})}.$$
 (3.1)

Here the DOS is normalized per unit area and subscript b represents a certain branch. $L_{b,\omega}$ denote the length of the isoenergy curve for branch b and energy $\hbar\omega$. With full dispersion, we can only obtain the energy and group velocity information at discrete reciprocal lattice points, so Eq. (3.1) must be evaluated numerically. The method proposed by Gilat and Raubenheimer[6] is modified here for 2D where the 1BZ is partitioned into grids and the isoenergy curve inside a grid is assumed to be a straight line segment while the group velocity inside the grid is constant. The associate error can be arbitrarily small as we reduce the grid size. Figure 3.2 shows the calculated phonon DOS for the three acoustic branches to be included in the PMC solver. Note that the ZA phonon DOS is overwhelmingly larger than that of TA and LA at very small energy range, making it the most numerous among all.

3.2 Single Phonon Generation

From Sec. 1.1.3, we now have all the information needed to generate an ensemble of phonons in graphene following the equilibrium BE distribution at a given temperature T. In practice, we generate one phonon at a time. To uniquely identify a phonon, we need to specify its energy $\hbar\omega$, branch b, wave vector \mathbf{q} , and group velocity $\mathbf{v}_{b,g}$. Note these properties are not entirely independent of each other: the group velocity is fixed once the other three are fixed. To generate a phonon, we first determine the environment temperature T (details in Sec. 3.3 and then choose $\hbar\omega$, b, and \mathbf{q} in the specified order. Figure 3.3 shows the generating process of a single phonon; arrows with dice next to it indicate random numbers are involved.

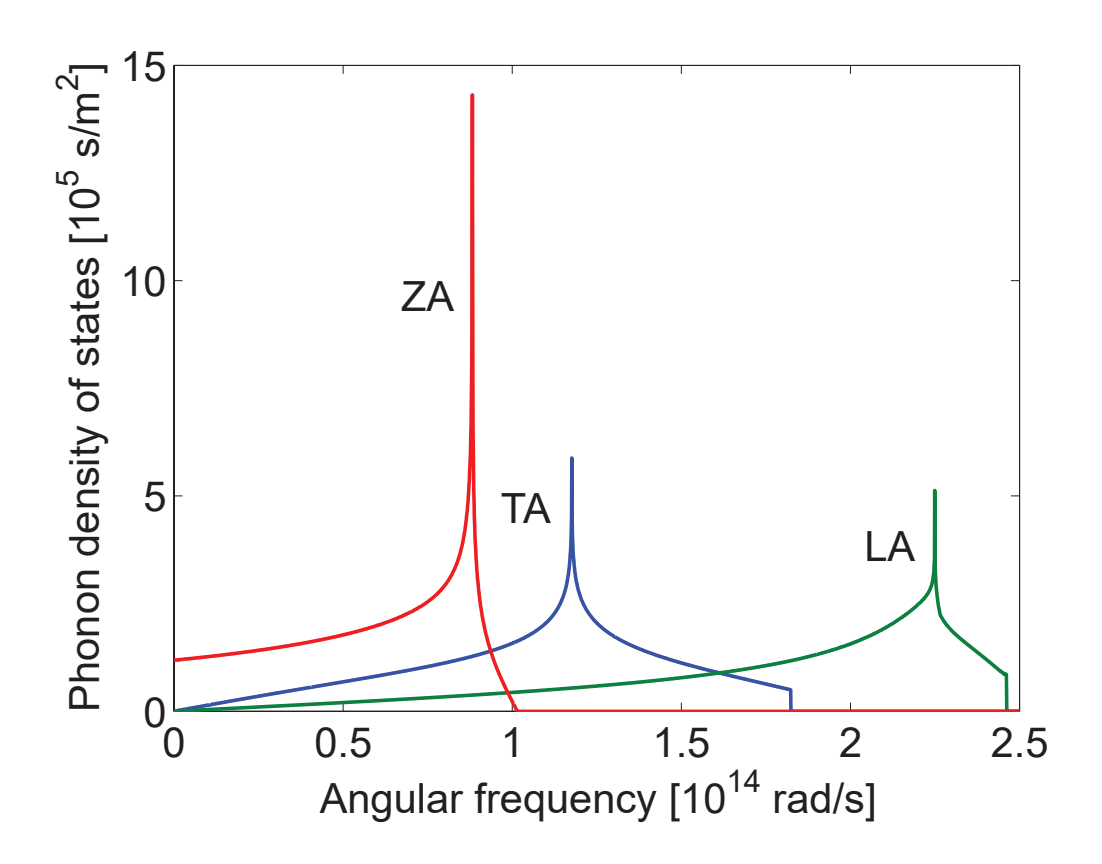


Figure 3.2: Phonon density of states (PDOS) for TA, LA, and ZA branches in graphene, calculated following the Gilat-Raubenheimer method.[6]

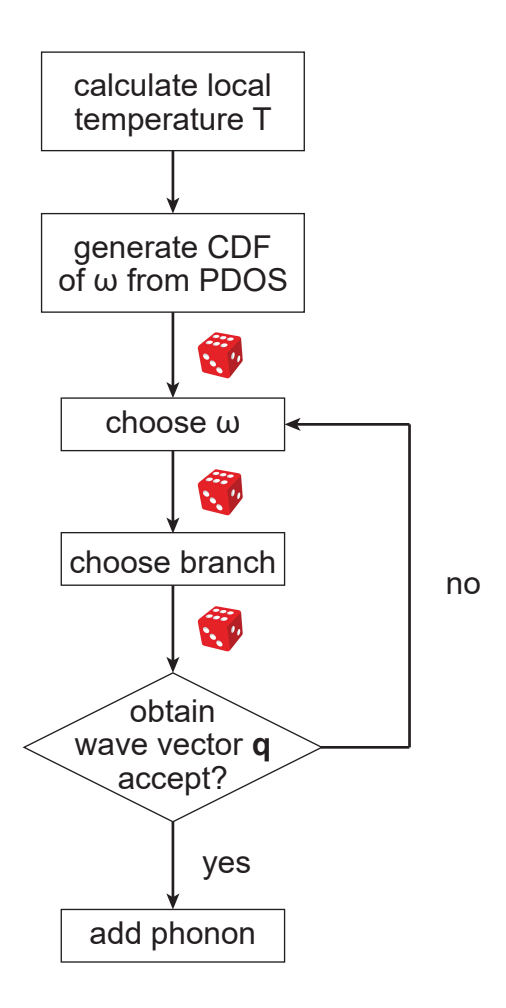


Figure 3.3: Flowchart showing the steps for generating a single phonon in the numerical ensemble of a cell at a given temperature. Dice indicate the use of random numbers.

3.2.1 Choosing Energy

In choosing $\hbar\omega$, we numerically inverse the cumulative distribution function (CDF) of ω . The total number of phonons with energy within $(0, \hbar\omega)$ is at temperature T is

$$N(\omega' < \omega) = \sum_{\mathbf{b}} \int_0^{\omega} n_{\mathrm{BE}}(\omega', T) D_{\mathbf{b}}(\omega') d\omega'. \tag{3.2}$$

To obtain the CDF, we normalize this with the total number of phonons in the system $N(\omega' < \omega_{\text{max}})$. In practice, we divide $(0, \omega_{\text{max}}]$ into N_{int} intervals separated by a small frequency $\Delta \omega$; the central frequency in the *i*th interval is $\omega_{\text{c},i}$. In addition, we use a branch-dependent phonon weight W_{b} (one simulation particle represents W_{b} real phonons) to save computation time. With everything in place, we form a CDF table with N_{int} entries

$$F_{i}(T) = \frac{\sum_{b} \sum_{j=1}^{i} \langle n_{BE}(\omega_{c,j}, T) \rangle D_{b}(\omega_{c,j}) / W_{b}}{\sum_{b} \sum_{j=1}^{N_{int}} \langle n_{BE}(\omega_{c,j}, T) \rangle D_{b}(\omega_{c,j}) / W_{b}}.$$
(3.3)

To complete the table, we set $F_0(T) = 0$, meaning that all phonons should have positive energy. It is easy to verify $F_i(T) \in [0,1]$. Figure 3.4 is a typical CDF for graphene at 300 K.

To choose phonon frequency, we draw a random number R_1 and look for the interval i satisfying $F_{i-1} < R_1 < F_i$ with the bisection algorithm. We decide the frequency of this phonon falls in the ith interval and the actual frequency is determined with another random number R_2 , $\omega = \omega_{c,i} + (2R_2 - 1)\frac{\Delta\omega}{2}$.

3.2.2 Choosing Branch

After an ω is chosen, we draw a third random number R_3 to choose the phonon branch b. The probability of a phonon with ω being in branch b is proportional to $D_b(\omega)$, therefore we have

$$b = \begin{cases} \text{TA}, & R_3 < f_{\text{TA}}(\omega) \\ \text{LA}, & f_{\text{TA}}(\omega) < R_3 < f_{\text{TA}}(\omega) + f_{\text{LA}}(\omega) \end{cases}$$

$$\text{ZA}, \quad \text{otherwise.}$$
(3.4)

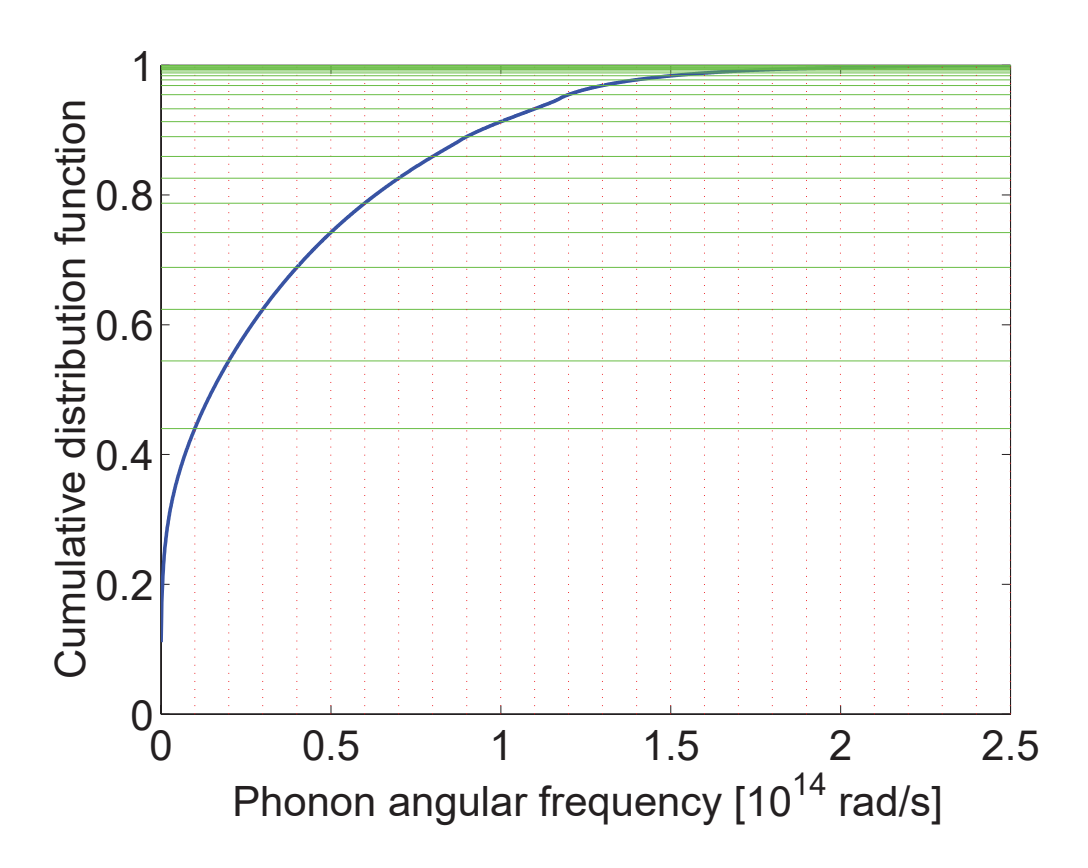


Figure 3.4: Cumulative distribution function of phonon frequency at 300 K. The frequency range $\omega \in [0, 2.5 \times 10^{14}] \text{rad/s}$ was divided into $N_{\text{int}} = 2500$ equal intervals in the numerical calculation.

where $f_{\rm b}(\omega) = \frac{D_{\rm b}(\omega)}{W_{\rm b}} / \sum_{b'} \frac{D_{\rm b'}(\omega)}{W_{\rm b'}}$ is the normalized probability of being in branch b for the chosen frequency ω with the weighting taken into consideration.

3.2.3 Choosing Wave Vector

After the phonon energy and branch are chosen, we are now limited to a specific isoenergy curve inside the 1BZ. We use a set of lookup tables together with the rejection technique to find a proper \mathbf{q} for the chosen phonon with energy $\hbar\omega$ and branch b, the detailed algorithm is documented in Appendix A. Note that we do not explicitly use \mathbf{q} in the simulation; it serves as a bridge to help us find the group velocity $\mathbf{v}_{b,g}(\mathbf{q})$ (in general not parallel to \mathbf{q}).

After obtaining $\mathbf{v}_{b,g}(\mathbf{q})$, the phonon generation process is complete and the generated phonon is put into a random location \mathbf{r} inside a certain cell (more details in Sec. 3.5.1). A complete phonon in our simulation has the following properties: ω , b, $\mathbf{v}_{b,g}(\mathbf{q})$, and \mathbf{r} ; these properties are maintained throughout the simulation.

3.3 Simulation Domain

The simulation domain is a 2D ribbon with width W and length L. We are mostly interested in the thermal transport in the two highly symmetric GNR orientations: AGNR and ZGNR. Figure 3.5 shows the schematic of an AGNR (top) and a ZGNR (bottom), respectively. Besides these two edge structures, a ribbon with perfectly smooth edges is used to recover the bulk graphene limit in the simulation.

As mentioned in Sec. 2.2, two ends of the simulation domain are held at slightly different temperatures $T_{\rm h}$ (hot end) and $T_{\rm c}$ (cold end). Following previous PMC work [51, 52, 53, 54, 55, 56], the simulation domain is divided into $N_{\rm c}$ cells along the length direction (longitudinal direction) and each cell i is assumed to be at a local equilibrium temperature T_i . In a typical simulation, $\Delta T = T_{\rm h} - T_{\rm c}$ is 20 – 40 K and $N_{\rm c}$ varies from 50 to 100, depending on the ribbon length. We make sure that the temperature drop in each cell is small ($\frac{\Delta T}{N_{\rm c}} < 0.5$ K) so that the local equilibrium approximation is valid. In each simulation, we initially assign temperatures in each cell so the temperature profile inside the ribbon is linear.

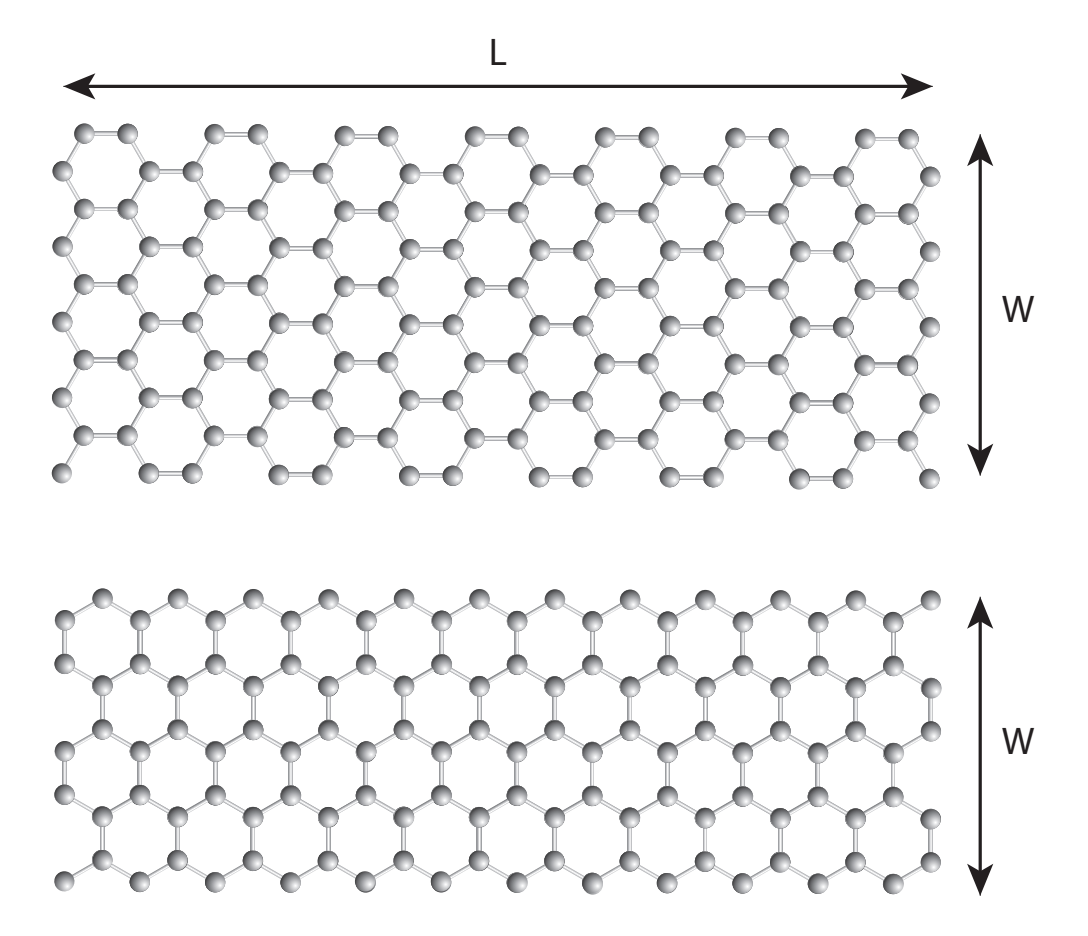


Figure 3.5: Schematic of the simulation domain of width W and length L. (Top) Armchair GNR. (Bottom) Zigzag GNR.

3.3.1 Boundary Conditions and Contacts

Since the simulation domain is finite, phonons might drift out and end up outside its boundaries. In our simulations, the boundaries along the longitudinal direction are reflecting boundaries: a phonon is reflected back inside if drifting into these boundaries. When the boundaries are perfectly smooth, all the reflections are specular, thus a ribbon with any width would restore the thermal conductivity of an infinite width ribbon.

The boundaries along the transverse direction (or at the two ends) are connected to heat baths and any phonon coming in is thermalized by the contact. The easiest way to implement the thermal contacts is to make the first cell at each end a "black-body cell".[45] After the drift and scattering process, all the phonons inside these two end cells or left from either end of the ribbon are deleted. At the end of each step, a new ensemble of phonons are generated according to the appropriate reservoir temperature to fill the end cell.

3.4 The Transport Kernel

The transport kernel is the main loop of the PMC solver. Time is discretized into small steps Δt ; the criterion for "small" is elaborated in Sec. 3.4.3. As time evolves, the phonon ensemble will first reach steady state and then stay at the steady state until the end of the simulation. Recall the Fourier's law (Eq. (1.10)), we are most interested in the heat flux j_q . The instantaneous value of j_q can be obtained by sitting at a cell boundary and count the energy taken across the boundary by all phonons at a certain time step. To detect the steady state, we take advantage of the fact that heat flux going into the ribbon must be the same as that coming out of the ribbon (so the energy inside stays constant). We compare the average heat flux coming in and going out at the two ends and claim steady state once their values are within 0.1% of each other. As briefly mentioned in Sec. 2.2, after steady state, we keep recording the instantaneous j_q at chosen cell boundaries over a period of time (~ 1 ns) to get a stable averaged heat flux value.

3.4.1 Phonon Drift and Edge Scattering

In the current algorithm, each phonon drift according to their own group velocity for the full time step in each loop. The target phonon position at the end of the step is

$$\mathbf{r}_{\text{end}} = \mathbf{r}_{\text{start}} + \mathbf{v}_g \Delta t. \tag{3.5}$$

In case of the perfectly smooth edge ribbon, updating the end location of the phonon is straightforward. If \mathbf{r}_{end} falls inside of the simulation domain, \mathbf{r}_{end} is updated directly; otherwise, the time δt when first contact happened is calculated by setting the y component of \mathbf{r}_{end} to that of the boundary being crossed. Then the new starting location is updated as the crossing location, the y component of the group velocity is flipped $(v_{y,g} = -v_{y,g})$, and the remaining drift time is updated as $\Delta t - \delta t$. The process is repeated until the drift time reduces to zero.

In case of the GNRs with real-space edges, we need to pay special attention to the edge scattering events. Although both the structures are perfectly periodic, these edges effectively introduce back-scattering of phonons and will reduce the thermal conductivity, similar to rough edges. In treating edge scattering, we need to make sure that: (1) the old phonon scatter into a legit new phonon according to the phonon dispersion relation, (2) the scattering is elastic (new phonon has the same energy as the old phonon), and (3) the distribution of phonons coming in the boundary should be the same as that going out. To satisfy these conditions simultaneously, we specifically chose edge-structures that possess the same symmetry as the phonon dispersion, therefore by simply specularly reflect a phonon at the boundary, all the requirements are automatically satisfied.

Even the boundary scattering is still specular, it is more complicated with real-space edges because of the shadowing effect. Figure 3.6 illustrates this effect in both armchair and zigzag edge structures. According to Eq. (3.5), the target end position is at point A, which is inside the ribbon. It is tempting to update the end location directly to A as previously done in the perfectly smooth ribbon. However, with closer analysis, an edge-scattering event should have happened at point B and the real end point is A'. To account for this effect,

a "soft wall" (red dashed line in Fig. 3.6) is introduced. The phonon drift will always stop whenever it hit the "soft wall", then we calculate the time it takes to get to all the (real) boundaries close by. The shortest time corresponds with the location where boundary scattering happens. This is repeated until the phonon leaves the region enclosed by the "soft wall" and the real boundaries.

3.4.2 Phonon Scattering Rate in Graphene

With the conditions we are interested in for suspended graphene, the following scattering mechanisms are considered: three-phonon (Umklapp and Normal), isotope, and grain boundary scattering. The total scattering rate for a given ω and b follows

$$\tau_{\mathbf{b}}^{-1}(\omega) = \sum_{i} \tau_{\mathbf{b},i}^{-1}(\omega), \tag{3.6}$$

where $\tau_{\rm b}^{-1}$ is the total scattering rate and $\tau_{\rm i,b}^{-1}$ is the contribution from the *i*th mechanism.

3.4.2.1 Phonon-Phonon Scattering

Phonon-phonon scattering dominates in the temperature range of our interest (300 – 600 K) for suspended graphene and three-phonon interactions are the most important form of phonon-phonon scattering in thermal conductivity calculation.[57, 47] As mentioned in Sec. 1.2.2, there are the non-resistive N process and the resistive U process. Considering the 3-phonon interactions explicitly is too computationally expensive and the accuracy still depends on how often we check the positions and the resolution of the dispersion. Therefore, we follow previous work [51, 45, 46] and treat the 3-phonon interactions as an effective inelastic 2-phonon process through a scattering rate[47]

$$\tau_{\mathrm{b,U}}^{-1}(\omega) = \frac{\hbar \gamma_{\mathrm{b}}^2}{\overline{M}\Theta_{\mathrm{b}} v_{\mathrm{s,b}}^2} \omega^2 T e^{-\Theta_{\mathrm{b}}/3T}.$$
(3.7)

Here $v_{\rm s,b}$ is the mode-dependent sound velocity, determined from the average slope of the dispersion curve near the Γ point ($v_{\rm s,TA}=1.17\times10^4$ m/s, $v_{\rm s,LA}=2.19\times10^4$ m/s, and

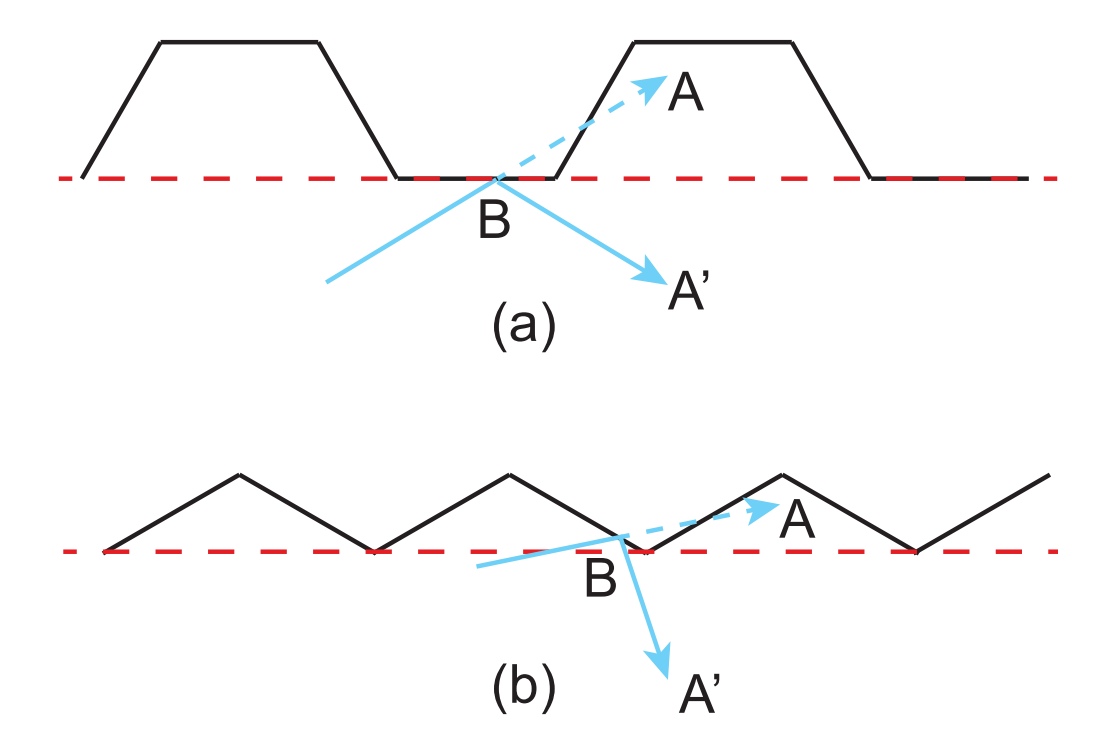


Figure 3.6: Illustration of the shadowing effect in treating boundary scattering in (a) armchair and (b) zigzag edges. By direct calculation, end-point location A is inside the ribbon. However, an edge-scattering event should have happened at point B and the real end-point location should be A'.

 $v_{\rm s,ZA} = 2.28 \times 10^3$ m/s). \overline{M} is the average atomic mass in graphene and $\Theta_{\rm b}$ is the mode-specific Debye temperature obtained from

$$\Theta_{\rm b}^2 = \frac{5\hbar^2}{3k_{\rm B}^2} \frac{\int \omega^2 D_{\rm b}(\omega) \ d\omega}{\int D_{\rm b}(\omega) \ d\omega}.$$
 (3.8)

In our case, Eq. (3.8) is numerically evaluated and the Debye temperature for three branches are $\Theta_{TA} = 1126.18$ K, $\Theta_{LA} = 1826.39$ K, and $\Theta_{ZA} = 623.62$ K, respectively. The strength of the scattering process is also controlled by the Grüneissen parameter γ_b , here we take $\gamma_{LA} = 2$, $\gamma_{TA} = \frac{2}{3}$, and $\gamma_{ZA} = -1.5.[47]$ The first half of the rate is the standard Umklapp interaction strength [57] and the exponential term adds the effective contribution from the redistribution via the N processes.

3.4.2.2 Isotope Scattering

The essence of isotope scattering is mass-difference scattering, thus the rate of which can also be used to treat impurity scattering. We deal with pristine graphene without impurities, so phonons scatter from the mass difference due to the naturally present isotopes. For carbon, the natural abundance is 98.9% for ^{12}C and 1.1% for ^{13}C . The mode-dependent isotope scattering rate is [58]

$$\tau_{\rm b,I}^{-1}(\omega) = \frac{\pi}{2} \Gamma \Omega_0 \omega^2 D_{\rm b}(\omega), \tag{3.9}$$

where

$$\Gamma = \sum_{i} f_i (1 - M_i / \overline{M})^2 \tag{3.10}$$

is the mass-difference constant and f_i is the abundance of the *i*th isotope. $\Omega_0 \approx 2.62 \times 10^{-20}$ m² is the average area occupied by one carbon atom. In our simulation, we consider both natural abundance and the isotropically modified graphene samples. As a matter of fact, from Sec. 1.1.2 we know the percentage of isotopes would also slightly modify the dispersion relation through the average atomic mass \overline{M} . Note this does not change the general shape of the dispersion, but we use the modified dispersion to generate tables for more accuracy. Isotope scattering is an elastic process.

3.4.2.3 Grain Boundary Scattering

Single-crystal graphene samples are obtained through exfoliation, which is not scalable. Chemical vapor deposition (CVD) on transition metal substrates such as copper has been used to synthesize good-quality large-area graphene, [59] yet CVD-fabricated graphene is always polycrystalline so phonons scatter from the grain boundaries, which yield as extra resistance. The expression for the grain-boundary scattering rate [60] is

$$\tau_{\rm GB}^{-1} = \frac{v}{l_{\rm G}} \Xi(\omega) \tag{3.11}$$

It is intuitive that the rate should be proportional to the phonon group velocity and inversely proportional to the average grain size $l_{\rm G}$. $\Xi(\omega) = \frac{1}{t_{\rm GB}(\omega)} - 1$ describes the influence of transmission coefficient $t_{\rm GB}(\omega)$ at the boundary. This matters because when a phonon hits the grain boundary, it could either transmit as if nothing was there or be reflected, and the probability of transmission is dependent on the energy, represented by $t_{\rm GB}(\omega)$. One can get the transmission coefficient from first principle calculations, but usually, for simplicity, we ignore the ω dependence of the transmission, and $\Xi(\omega)$ reduces to a coefficient describing the influence of the average transmission. We treat the grain boundary scattering as an elastic scattering process just like isotope scattering. Another reason why we could ignore the ω dependence is that, with the CVD technique, the average grain size in polycrystalline graphene could be quite large and the grain boundary scattering rate is fairly small compared to other intrinsic scattering events. This is also why CVD graphene shares a lot of extraordinary properties of exfoliated graphene in experiment. [61, 62, 63] A recent account of phonon transport in polycrystalline suspended graphene, considering the grain-size distribution, can be found in Ref. [64].

3.4.3 Phonon Scattering and Time Step

In our transport kernel, edge scattering events are explicitly considered in the drifting step (Sec. 3.4.1) and other mechanisms are considered in scattering step. As mentioned in Sec. 2.2, we consider at most one scattering event at each step, the probability of scattering

after time Δt is [32]

$$p_{\text{b,scat}}(\omega) = 1 - \exp[-\Delta t \cdot \tau_{\text{b}}^{-1}(\omega)]. \tag{3.12}$$

Since we use a single time step for all phonons, it must be small enough so that the average probability of scattering for all phonons, $\overline{p_{\rm scat}}$, is sufficiently small. In practice, we tested out several choices and found that $\overline{p_{\rm scat}} < 1\%$ is a good criterion for choosing the time step Δt . As a result, the time step would vary for simulations at different temperatures, as the rates are temperature dependent. For suspended graphene at 300 K, we use $\Delta t = 0.1$ ps.

Upon completion of the drift routine in each step, we calculate for each phonon the probability of having been scattered during the previous step from Eq. (3.12). Note that scattering rates are temperature-dependent, so we should update the temperature in each cell after the drift before calculating the probabilities. We then use a random number r_1 to decide whether the phonon would actually scatter. If $r_1 > p_{\rm b,scat}$, nothing happened and we move on to the next phonon. If $r_1 \leq p_{\rm b,scat}$, the phonon scattered and we go on to choose the mechanism. As Δt is small, the probability for mechanism i is proportional to its scattering rate

$$p_{\mathrm{b,scat},i}(\omega) = 1 - \exp[-\Delta t \cdot \tau_{\mathrm{b},i}^{-1}(\omega)] \approx \Delta t \cdot \tau_{\mathrm{b},i}^{-1}(\omega). \tag{3.13}$$

Similar to choosing phonon branch in Sec. 3.2.2, another random number r_2 to choose the mechanism.

Once the mechanism is chosen, we scatter the phonon according to whether the scattering event is inelastic (phonon-phonon scattering) or elastic (isotope and grain-boundary scattering). For elastic process, we keep the phonon branch and energy, but randomly find a new wave vector and group velocity according to the dispersion relation following the same algorithm as in Sec. 3.2.3. For inelastic process, we replace the phonon with a random new phonon from the phonon pool. We make sure that phonons being replaced and added have the same distribution, so the energy is conserved collectively among the ensemble. A caveat is that this distribution is different from the equilibrium BE distribution we used in Sec. 3.2.1, because the scattering rate is energy-dependent and phonons with large energy has a higher probability of being replaced. As a result, we need a modified CDF to generate

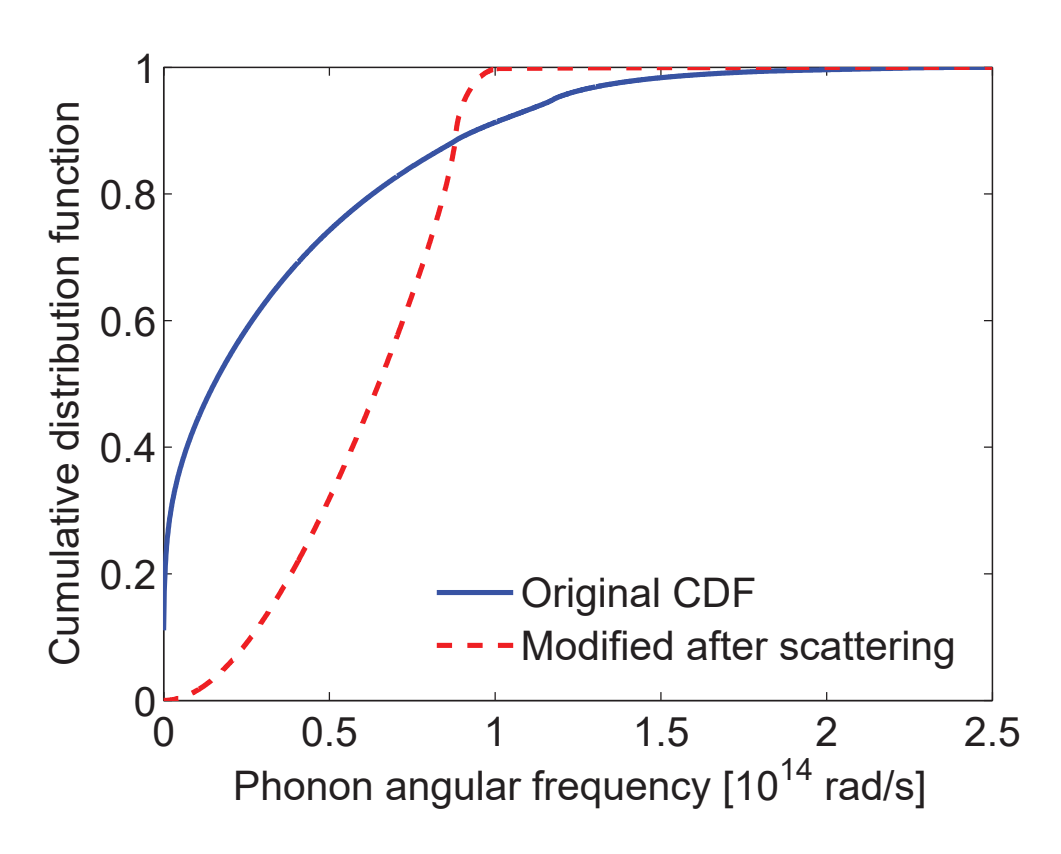


Figure 3.7: A typical modified (post-scattering) CDF, Eq. (3.14), and the original CDF, Eq. (3.3), at 300 K.

phonons after the phonon-phonon interaction:

$$F_{\text{mod},i}(T) = \frac{\sum_{b} \sum_{j=1}^{i} N_{j}(T) \cdot p_{b,U}(\omega_{c,j})}{\sum_{b} \sum_{j=1}^{N_{\text{int}}} N_{j}(T) \cdot p_{b,U}(\omega_{c,j})},$$
(3.14)

where $N_j(T) = \langle n_{\rm BE}(\omega_{{\rm c},j},T) \rangle D_{\rm b}(\omega_{{\rm c},j})/W_{\rm b}$ is the average number of simulation particles in the jth energy interval and $p_{\rm b,U}(\omega_{{\rm c},j})$ is the probability of a phonon in branch b suffering from phonon-phonon scattering during the step. A typical modified CDF is shown in Fig. 3.7 for 300 K and $\Delta t = 0.1$ ps.

3.5 Energy Conservation

At steady state, the total phonon energy inside the simulation domain must be conserved. Since we are deleting and generating phonons at each step (thermal contacts and inelastic scattering), we need to make sure energy is conserved.

3.5.1 Initialization

The initialization process refers to filling a cell with phonons according to an assigned temperature T. It happens before we enter the transport kernel and at the thermal contacts each step (Sec. 3.3). For a cell with area A and temperature T, the expected total phonon energy is

$$E_{\text{target}} = A \sum_{\mathbf{b}} \int D_{\mathbf{b}}(\omega) \langle n_{\text{BE}}(\omega, T_i) \rangle \hbar \omega \ d\omega. \tag{3.15}$$

As we generate phonons one by one and put them into a random location inside the cell, we keep track of the phonon energy already added to the cell

$$E_{\text{current}} = \sum_{i} \hbar \omega_i W_{b_i}, \tag{3.16}$$

where i runs through all the phonons inside the cell. We call the maximum energy carried by a numerical particle $E_{\text{max}} = \max(\hbar \omega_i W_{b_i})$. Since we have no control over the energy of phonon to be generated (Sec. 3.2), we cannot meet $\mathcal{E}_{\text{target}}$ exactly. Instead, we stop generating phonons when

$$E_{\text{current}} \in [E_{\text{target}} - E_{\text{max}}/2, E_{\text{target}} + E_{\text{max}}/2]$$
 (3.17)

while keeping track of

$$E_{\text{residue}} = E_{\text{target}} - E_{\text{current}}.$$
 (3.18)

The next time we want to enforce energy conservation in the cell, the residue energy is added to the calculated target energy

$$E_{\text{target}} = E_{\text{target}}^{\text{cal}} + E_{\text{residue}}.$$
 (3.19)

3.5.2 Reinitialization

The reinitialization process happens after the scattering step. The way we treat inelastic scattering (Sec.3.4.3) events only conserves energy on an average sense when lots of phonons are being replaced. However, sometimes scattering events are rare and it takes a long time to achieve steady state. Reinitialization is added to expedite the process; the idea is similar to that in the initialization process (Sec. 3.5.1). Before scattering, the exact total energy inside a cell is recorded as $E_{prescat}$, which makes the target energy after scattering

$$E_{\text{target}} = E_{\text{prescat}} + E_{\text{residue}}.$$
 (3.20)

After scattering, we compare the actual cell energy $E_{\text{afterscat}}$ with E_{target} . If $E_{\text{afterscat}}$ is too large, we randomly choose phonons one by one inside the cell to delete. If $E_{\text{afterscat}}$ is too small, we generate new phonons (from the original CDF) to add to the cell. Both the deletion and addition ends when

$$E_{\text{current}} \in [E_{\text{target}} - E_{\text{max}}/2, E_{\text{target}} + E_{\text{max}}/2],$$
 (3.21)

and the new residue energy is updated afterwards.

3.6 Simulation Results

The goals we want to achieve with the 2D PMC solver are: (1) accurately describe thermal conductivity of graphene, (2) capture the experimentally measured size-dependent thermal conductivity or the ballistic to diffusive crossover, (3) understanding why the crossover exists and predict the thermal conductivity at the diffusive limit, and (4) study orientation-dependent thermal conductivity of GNRs. In this section, we show the simulation results for all the entires mentioned.

3.6.1 Reliability Test

A good reliability test for PMC is a comparison of the steady-state temperature profile between the diffusive and ballistic limits. Purely diffusive transport should lead to a linear temperature profile while ballistic transport would result in a constant temperature $T_{\text{ballistic}} = (\frac{T_{\text{h}}^4 + T_{\text{c}}^4}{2})^{1/4}$ inside the ribbon, with abrupt changes at the two ends.[65] For situations in between – the quasiballistic regime – the temperature profile is expected to have both features: a linear drop inside the ribbon, with an abrupt change at the two ends. We accurately capture all three regimes in the PMC simulation: calculations in the diffusive and ballistic limits are presented in the inset to Fig. 3.8, while the quasiballistic regime is depicted in Fig. 3.9).

Further, in order to validate our assumption of local equilibrium, especially in the ballistic regime, we made a phonon distribution histogram inside the ribbon in steady state. The normalized histogram (main panel of Fig. 3.8) falls right on top of the theoretically calculated BE distribution, proving that our local equilibrium assumption stands even in the ballistic limit. Therefore, the PMC algorithm is reliable from the ballistic all the way to the diffusive regime. In the quasiballistic regime, we extend the definition of thermal conductivity and use the slope of the linear region inside the ribbon as the gradient ∇T in Eq. 1.10 to calculate the "size-dependent" thermal conductivity.

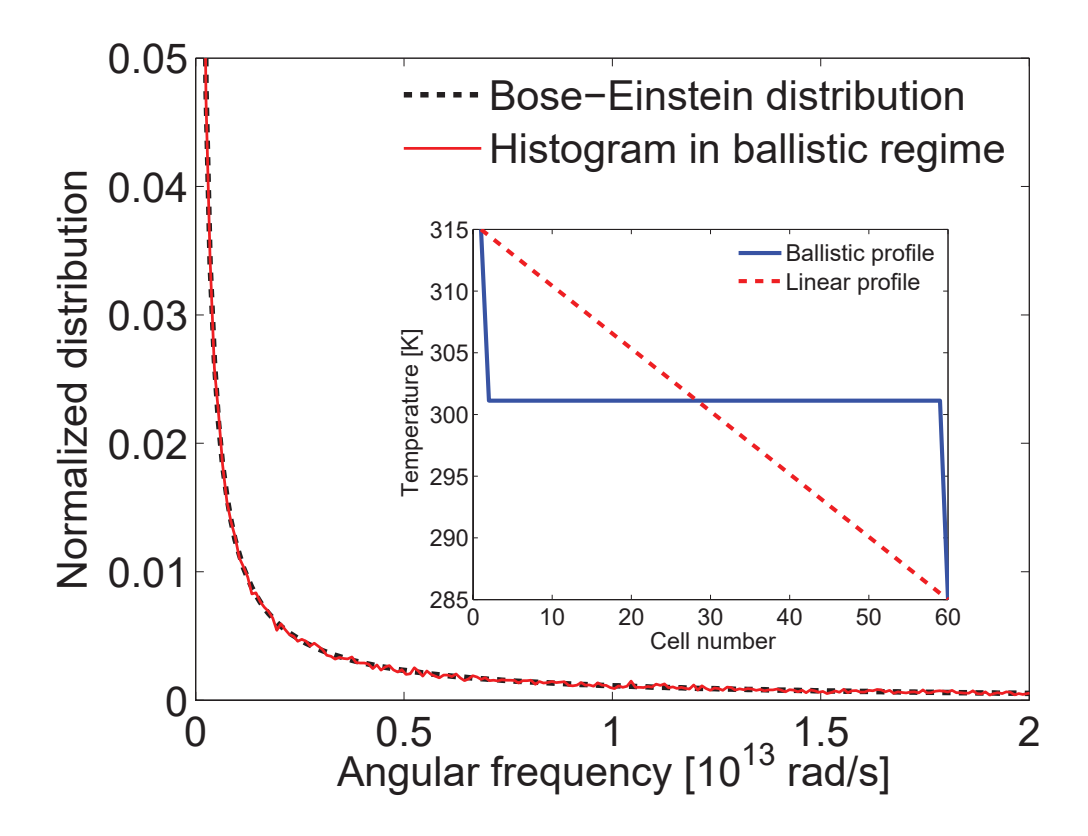


Figure 3.8: (Main panel) Normalized phonon distribution histogram in the ballistic transport regime compared with the Bose-Einstein distribution. The histogram is obtained by running the simulation with all the scattering mechanism turned off and recording the energies of all the phonons inside the GNR after the steady state is established; $T_{\rm h}=315~{\rm K}$ and $T_{\rm c}=285~{\rm K}$ in this case. The Bose-Einstein distribution is obtained based on temperature $T_{\rm ballistic}=301.12~{\rm K}$ inside the ribbon. (Inset) The calculated temperature profile inside the ribbon in the ballistic limit. The linear profile is also depicted for comparison.

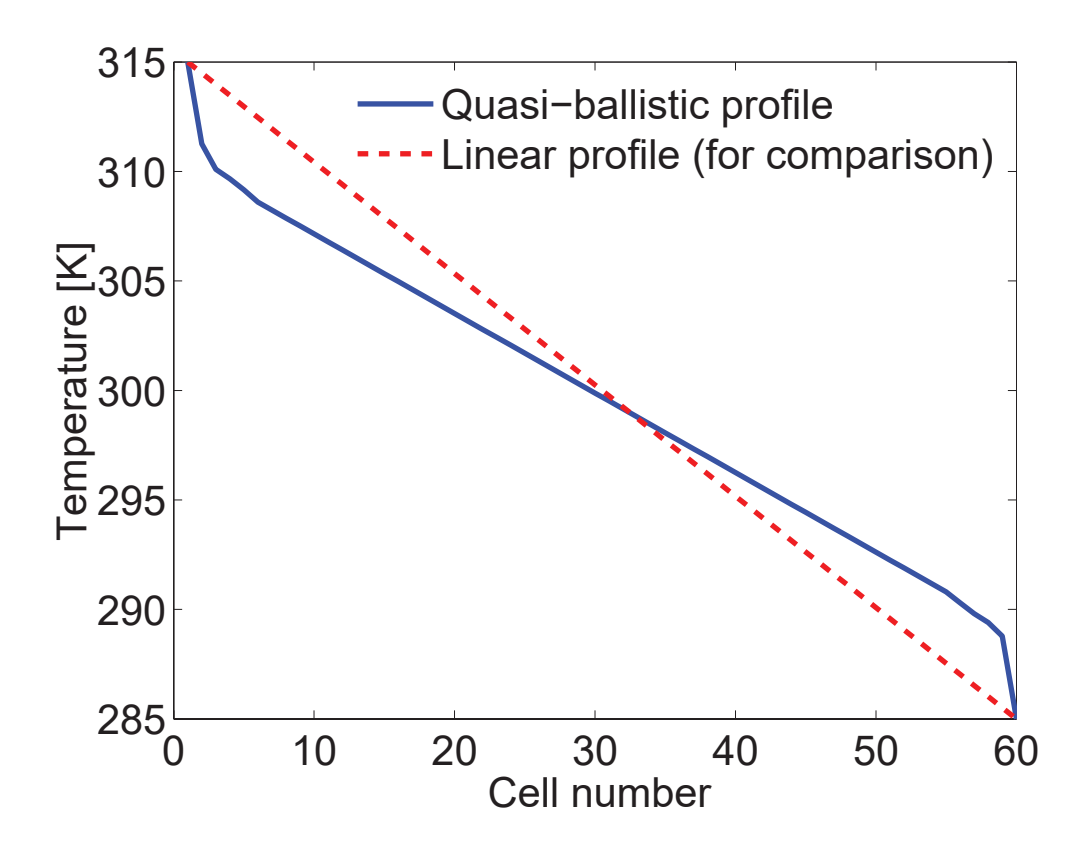


Figure 3.9: A typical temperature profile along the ribbon in the quasiballistic transport regime. Here the temperature at two ends are $T_{\rm h}=315$ K and $T_{\rm c}=285$ K and the number of cells $N_{\rm c}=60$.

3.6.2 Length-Dependent Thermal Conductivity

We look at the thermal conductivity of graphene and GNRs from 300 K to 600 K, the range where most experiments are carried out. [66, 67, 68, 69, 7, 9, 70, 8, 71] Thermal conductivity of suspended GNRs generally depends on both width and length. [47, 7, 8] The width dependence comes from the relative importance of edge scattering to internal mechanisms; for wide enough GNRs, thermal conductivity no longer depends on the width. [70, 8] We use perfectly smooth boundary GNRs with small width to mimic transport in very wide GNRs where there is no width dependence in their thermal conductivity (Sec. 3.3).

3.6.2.1 Comparison with Experiment

Chen et al. [7] fabricated large-area graphene using the CVD technique and transferred it onto a low-stress silicon-nitride-membrane substrate, with several holes of diameters $D_{\rm h}$ ranging from 2 to 10 μ m. Thereby, they obtained suspended circular graphene samples of given diameters and measured their thermal conductivities using Raman spectroscopy. There is no edge roughness and the characteristic length associated with the heat-flow direction is the hole diameter. We do not simulate circular samples here, but we can set the ribbon length L to match D_h , and the resulting thermal conductivity should be comparable to the experimental data. In Fig. 3.10, we present the calculated thermal conductivity for GNRs with lengths comparable to the sample diameters in the experiments of Chen et al. [7] As the experiments were performed on CVD-grown, polycrystalline graphene, we have included grain-boundary scattering in the calculation. The simulation results agree well with the measurement from 300 K to 600 K and for various sizes. Based on our simulations, phonon transport in all these samples is still in the quasiballistic regime: the thermal conductivity monotonically increases with increasing sample length. Chen et al. observed a size dependence for samples from 2 to 8 μ m, but, owing to a large uncertainty in the measurements, they could not accurately extract a monotonic dependence over the size range.

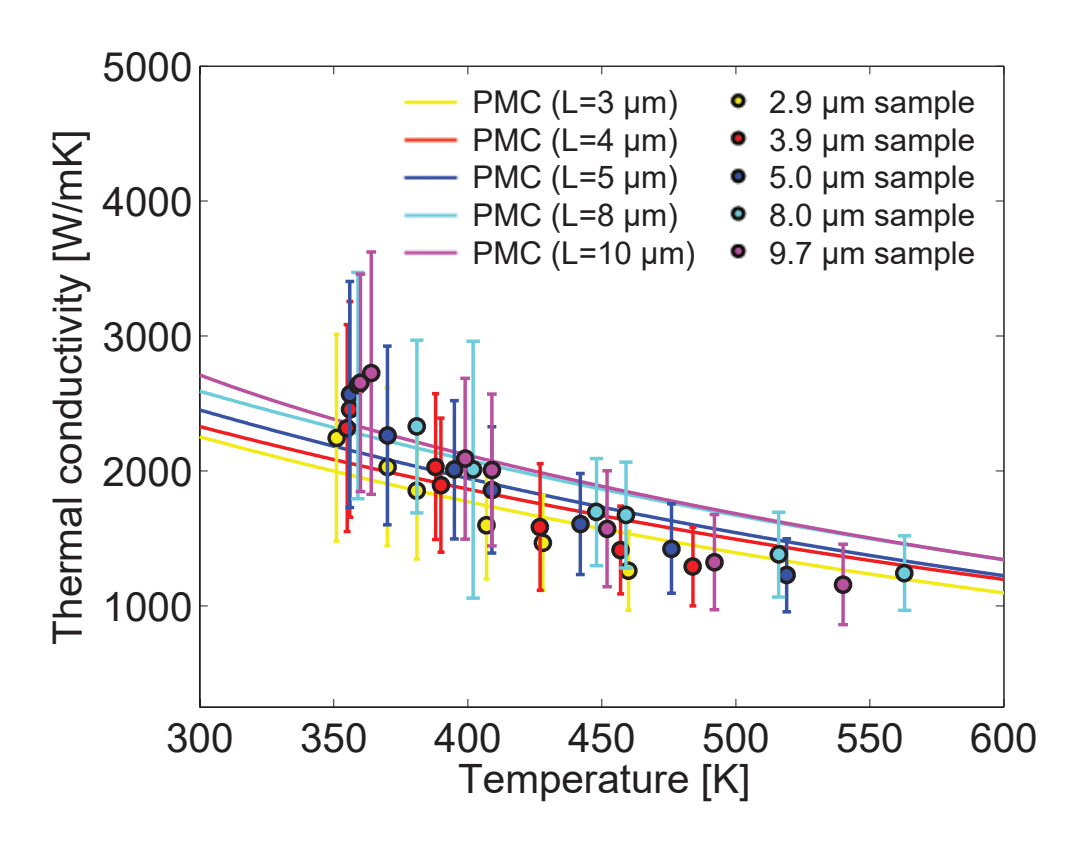


Figure 3.10: Thermal conductivity of graphene for different lateral dimensions, as obtained by Chen *et al.*[7] in the circular geometry (symbols) and from our simulation in the rectangular GNR geometry (lines).

3.6.2.2 Ballistic-to-Diffuse Crossover

Length-dependence of thermal conductivity comes from the relative magnitude of the phonon mean free path (MFP) Λ and the ribbon length L; for long enough GNRs, transport would be diffusive and the length dependence would vanish. Ghosh et~al.[72] estimated the MFP of graphene to be $\Lambda \sim 800$ nm near room temperature. However, in our simulations, we find that Λ for phonons in different branches and energy ranges from a few nanometers all the way up to hundreds of microns. Figure 3.11 shows the cumulative distribution function of phonon mean free path Λ for suspended graphene at 300 K. Note that about 20% of phonons have $\Lambda > 100~\mu m$ and more than 10% have $\Lambda > 200~\mu m$. Figure 3.12 shows the calculated thermal conductivity of wide GNRs over a range of lengths L at room temperature. The thermal conductivity keeps increasing with increasing length up to $L \sim 100~\mu m$, which is to be expected considering that nearly 20% of phonons have a mean free path longer than that (see Fig. 3.11). This length is larger than any of the measured samples, therefore, all the existing experiments on suspended graphene [66, 68, 67, 69, 7, 8] were carried out in the quasiballistic regime, so the maximal thermal conductivity of suspended bulk graphene could be higher than what experiments indicate.

This simulation captures the ballistic-to-diffusive crossover of phonon transport in suspended graphene. [70] In the purely ballistic transport regime, the thermal conductance G tends to a constant, while in the purely diffusive transport regime, the thermal conductivity κ is constant. G and κ are related through $G = \kappa \frac{A}{L}$ where A is the cross-sectional area perpendicular to the heat-flow direction and L is the length. We denote the constant thermal conductance in the ballistic regime as G_{ball} and the constant thermal conductivity in the diffusive regime as κ_{diff} . As $L \to 0$,

$$\kappa \approx G_{\text{ball}} \cdot \frac{L}{A}.$$
(3.22a)

As $L \to \infty$, we have

$$\kappa \to \kappa_{\text{diff}}.$$
 (3.22b)

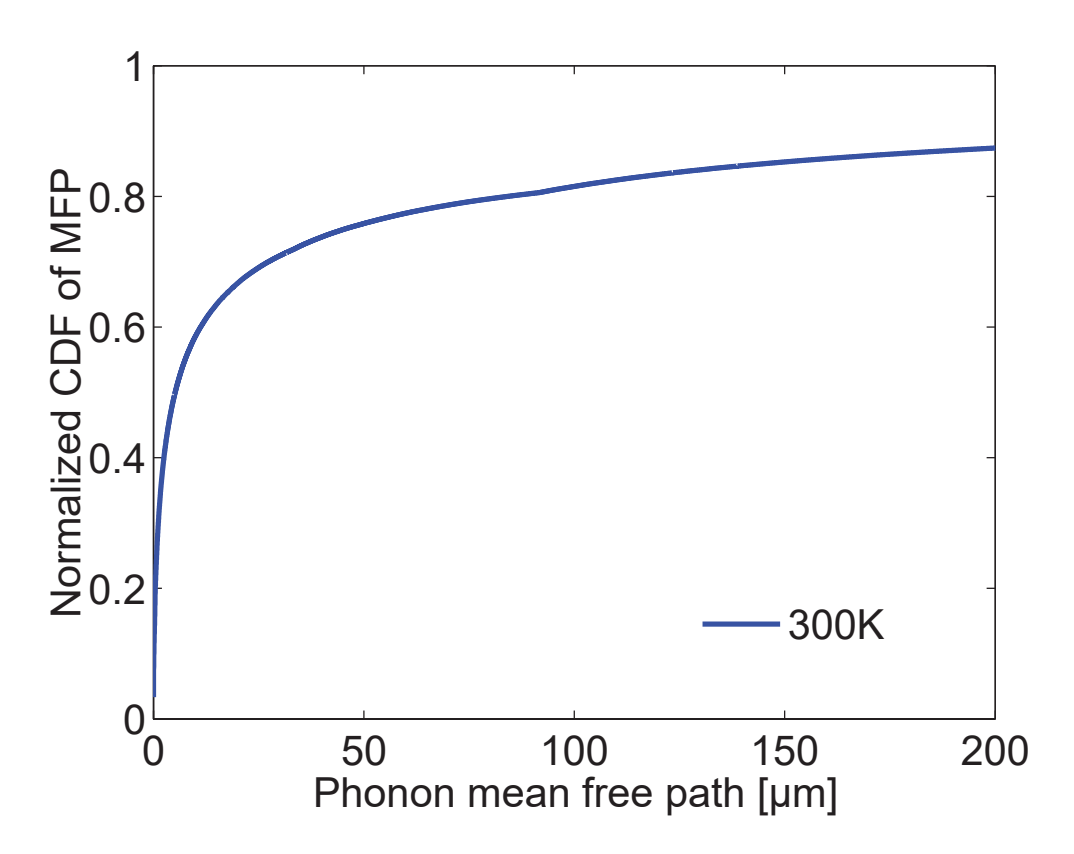


Figure 3.11: Normalized cumulative distribution function of phonon mean free path for suspended graphene at 300 K. About 20% of phonons have a mean free path greater than 100 μ m.

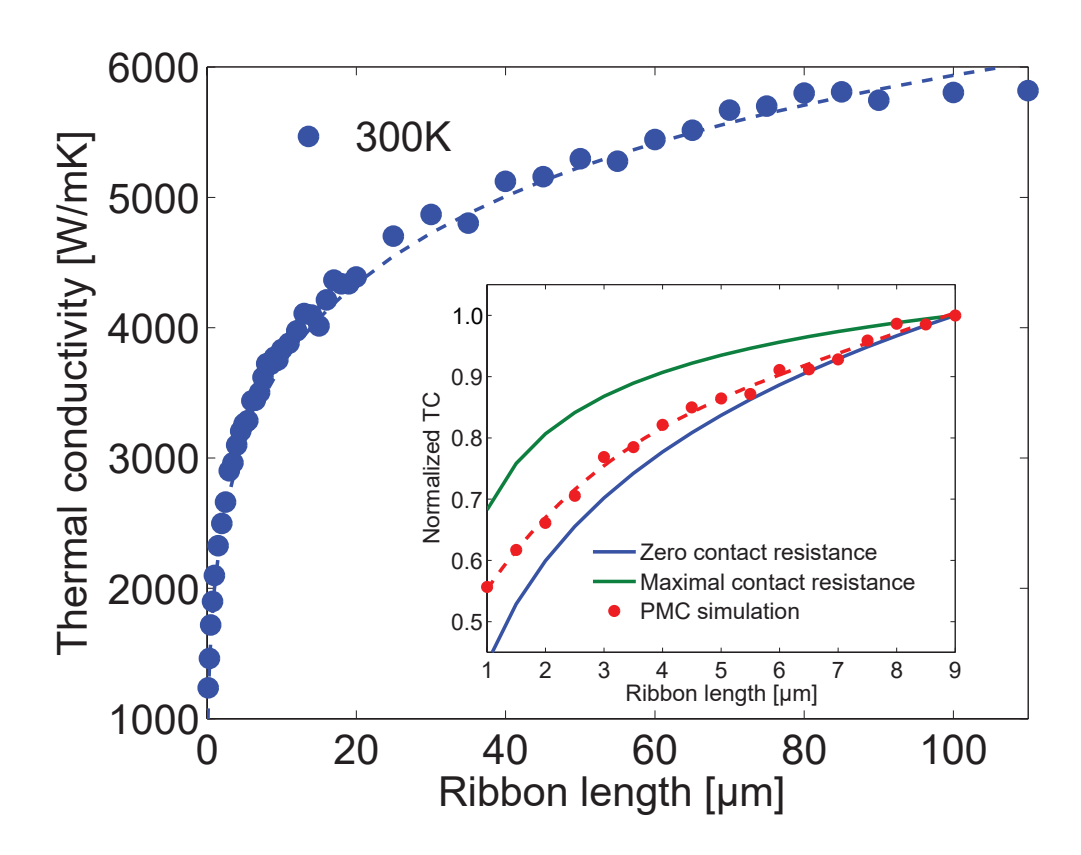


Figure 3.12: Length-dependent thermal conductivity of wide GNRs at room temperature, obtained from the PMC simulation. Dashed line is a guide for the eye. (Inset) Comparison of normalized thermal conductivity from our simulation (red dots) and the experimentally obtained data of Xu et al.[8] The blue curve shows the thermal conductivity estimated with maximal contact resistance, the green one corresponds to the value with no contact resistance.

At the left end of Fig. 3.12, thermal conductivity varies almost linearly with length, indicating ballistic transport. $G_{\rm ball}$ of GNR depends on width,[73, 74, 75] and from our simulation we extract the room-temperature ballistic conductance per unit cross section as $G_{\rm ball}/A \approx 5 \times 10^9$ W/m²K, which is close to the theoretical value of 5.28×10^9 W/m²K obtained by Muñoz, Lu, and Yakobson.[74] At the right end, thermal conductivity does saturate at very large lengths (around 100 μ m at room temperature). For the quasiballistic region in between, it is often assumed that the ballistic and diffusive transport channels can be connected "in series", which would give $\kappa^{-1} = \kappa_{\rm diff}^{-1} + G_{\rm ball}^{-1} A/L$.[70] We find it impossible to fit the data using this expression; any such fit that is reasonable at low L drastically underestimates the diffusive limit. A dashed curve numerical fit in the main panel of Fig. 3.12, to guide the eye, follows $\ln \kappa = 7.6 + 0.3 \ln L - 0.013 (\ln L)^2$, i.e. $\kappa \approx 1998 L^{0.3} L^{-0.013 (\ln L)}$. It is clear that this fit is poor in the diffusive limit, as it does not saturate, but may be appropriate for a number of experiments with GNRs shorter than $100 \, \mu$ m.

Recently, Xu et al. [8] observed a length dependence of thermal conductivity in their suspended wide GNR samples. However, their measured thermal conductivity is much smaller than our simulation results as well as other experimental ones; [7, 9] the offset is likely related to sample-preparation specifics. In order to compare with their length-dependence trend, we scaled their data and ours to 1 at the maximal length they measured. The inset to Fig. 3.12 shows a comparison between the scaled data from our PMC simulation and the experiment of Xu et al. [8] (experimental results are presented here via best quadratic fits to the data, green and blue curves). The green line and the blue line are the estimated maximal and minimal possible thermal conductivities, and our simulation falls right in between.

3.6.3 Isotope effect

Thermal conductivity of graphene could be largely influenced by isotopes. Chen et al.[9] measured thermal conductivity of graphene with different ¹³C compositions. From the simulation point of view, phonon dispersion, DOS, and scattering rates all change as the abundance of ¹³C changes. We choose GNRs with $L = 2.8 \mu m$ following experiment.[9]

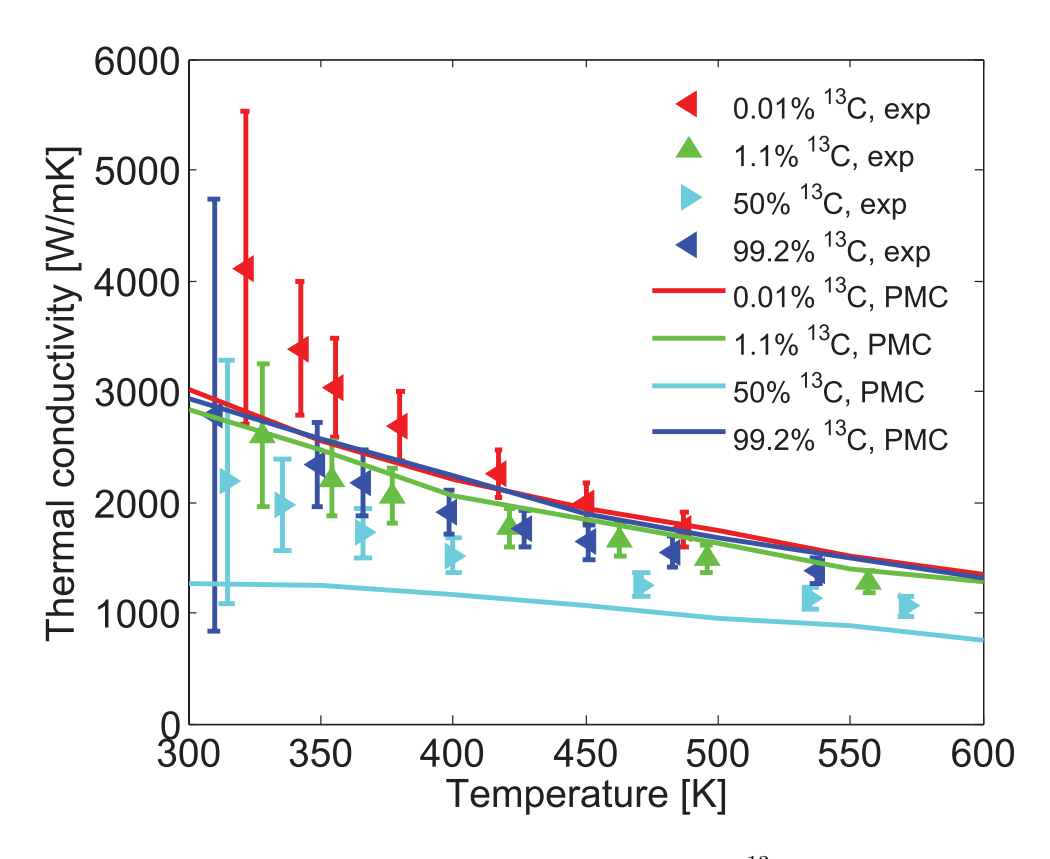


Figure 3.13: Thermal conductivity of graphene with different ¹³C abundance as a function of temperature. Symbols represent the experimental data from Chen *et al.*[9] and lines show our PMC simulation results.

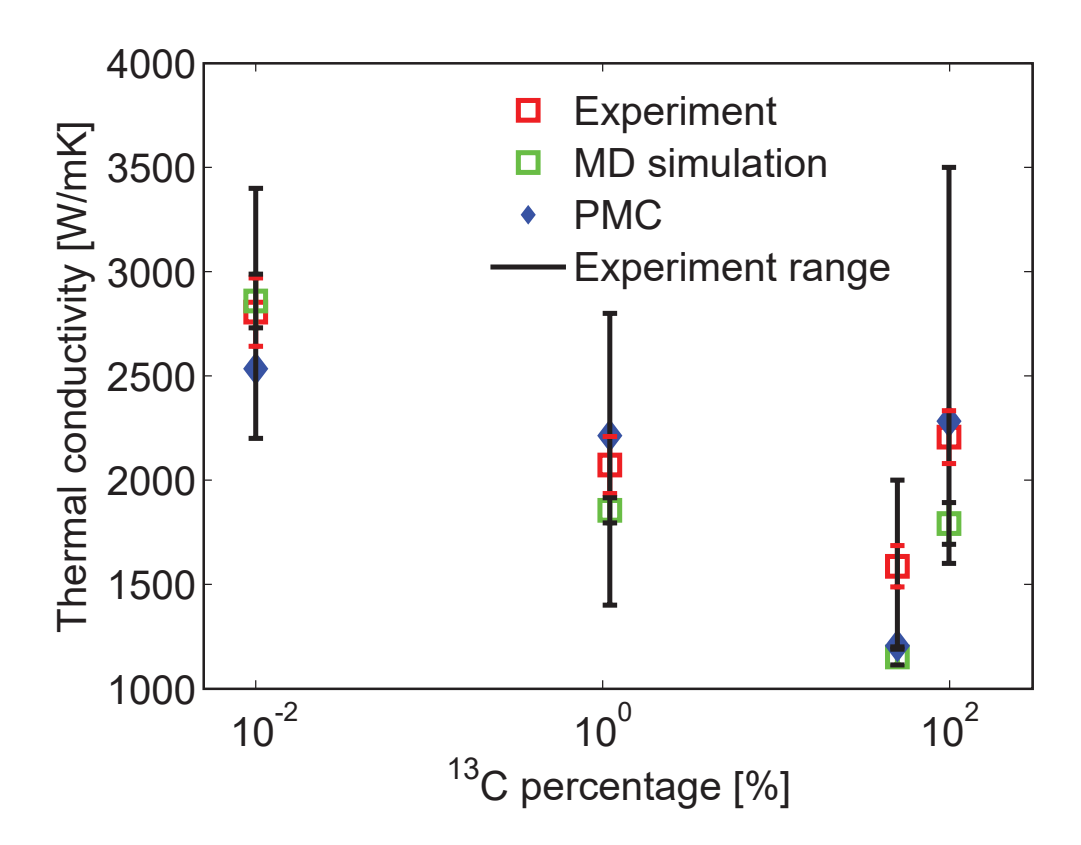


Figure 3.14: Thermal conductivity of graphene as a function of ¹³C abundance at 380 K. Red squares show the experimental data from Chen *et al.*[9], green squares are the MD simulation results from the same paper, and blue diamonds correspond to the PMC simulation.

Figure 3.13 shows the temperature dependence for four different compositions from experiment[9] compared with our PMC simulation results. We are able to capture the composition-dependence trend: thermal conductivity with 50%¹³C is the lowest because the two isotopes are equally mixed, giving rise to maximal isotope scattering. In general, our simulation data agrees well with experiment in a large temperature and ¹³C abundance range.

Figure 3.14 shows a direct comparison of thermal conductivity versus 13 C composition at a fixed temperature (T = 380 K). Our results are within the measured range and are even closer to the experimental data than the molecular dynamics simulation results reported by Chen *et al.* themselves.[9]

3.6.4 Width-dependent thermal conductivity

Perfectly periodic edge structures have been achieved in practice for both armchair [76, 77, 78, 79] and zigzag [76, 77, 79] orientations. Both theoretical [80] and experimental [81] work show the perfect armchair edge to be stable. The zigzag edge is relatively stable, though theory predicts that the zigzag edge can reconstruct to a pentagon-heptagon shape and become more stable. [80] Experiments showed that reconstructions in both direction (from all hexagon to pentagon-heptagon and from pentagon-heptagon to all hexagon) are spontaneous under the experimental environment conditions. [81] It was also shown that the bond length and angle between bonds at the edges may differ slightly from those inside the ribbon. [80, 81] We work with perfect edges because of they share the symmetry of graphene dispersion (Sec. 3.4.1) For simplicity, we use the equilibrium C-C bond length as the length of our edge segments and neglect the bond-angle changes.

In studying the width-dependence, we set the $L=10~\mu\mathrm{m}$ for all the GNRs. Figure 3.15 shows the width dependence of thermal conductivity for both AGNRs and ZGNRs at 300 K. We see that the thermal conductivity for both orientations varies greatly with width, approaching the smooth-edge value for the same length in the wide-GNR limit. The difference with respect to orientation is minute here at room temperature. The influence

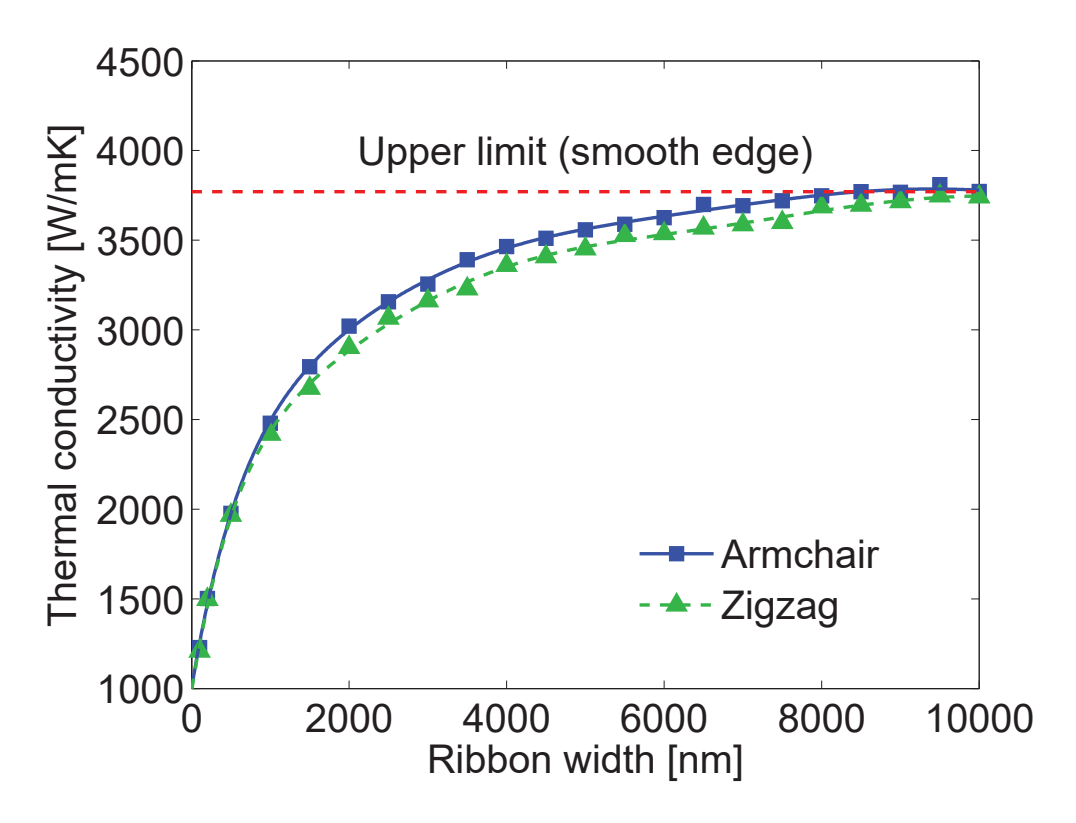


Figure 3.15: Thermal conductivity of $10 - \mu \text{m}$ -long AGNRs (blue squares) and ZGNRs (green triangles) at 300 K as a function of GNR width, obtained from the PMC simulation. The red dashed line is the upper limit of thermal conductivity for the same length, calculated with a flat-edge GNR.

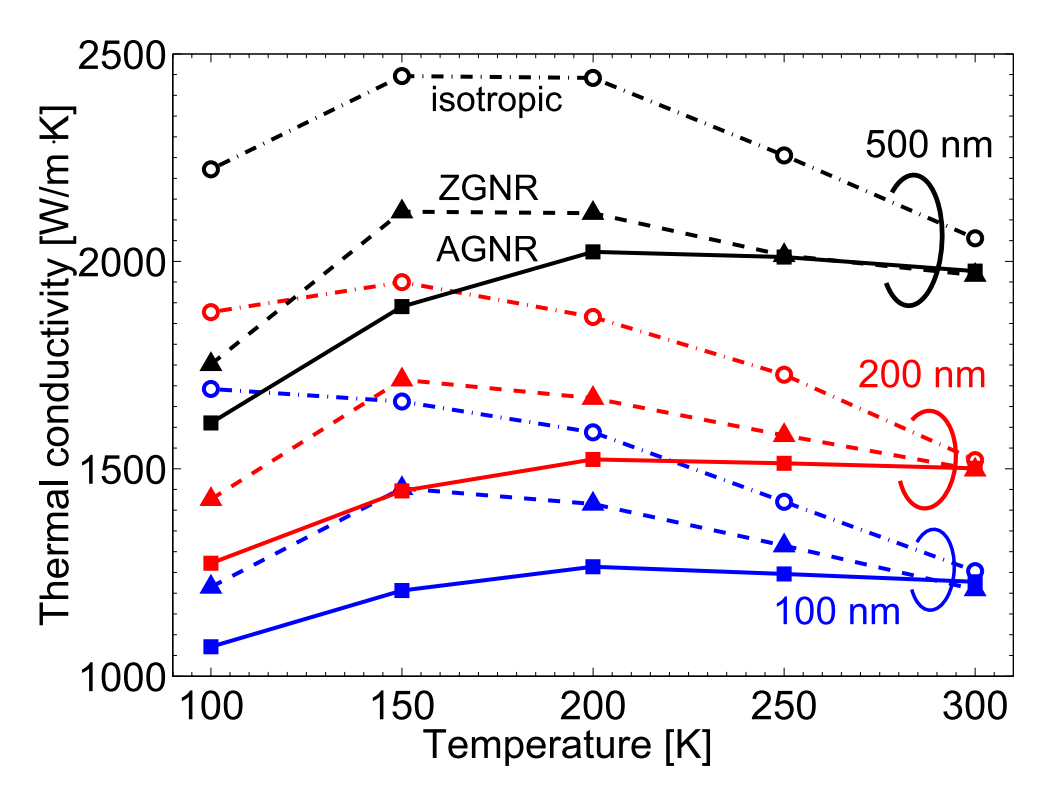


Figure 3.16: Thermal conductivity versus temperature for GNRs of width 500 nm (black), 200 nm (red), and 100 nm (blue) calculated based on PMC. For each width, we present data obtained with isotropic dispersion (open circles), as well as with full dispersion assuming the AGNR (solid squares) and ZGNR (solid triangles) ribbon orientation.

of orientation and full dispersion only becomes significant at lower temperatures. We include both full-dispersion AGNR and ZGNR as well as an isotropic dispersion approximation to demonstrate the point. For each acoustic branch, the isotropic dispersion approximation was obtained from a quadratic fit to the full dispersion, $\omega_{\rm b} = v_{\rm s,b}q + c_{\rm b}q^2$. Here, $c_{\rm TA} = -1.15 \times 10^{-7}$, $c_{\rm LA} = -3.95 \times 10^{-7}$, and $c_{\rm ZA} = 2.83 \times 10^{-7}$ (in m²/s), while $v_{\rm s,TA} = 1.17 \times 10^4$, $v_{\rm s,LA} = 2.19 \times 10^4$, and $v_{\rm s,ZA} = 2.28 \times 10^3$ (in m/s). All GNRs have the same length $L = 10~\mu{\rm m}$ and their widths take values of 500-nm, 200-nm, and 100-nm. Figure 3.16 shows the calculated thermal conductivity as a function of temperature for these GNRs.

Based on Fig. 3.16, we see that the isotropic dispersion approximation generally overestimates thermal conductivity, quite dramatically so at low temperatures. The relative error brought about by the use of isotropic approximation at low temperatures is quite high in narrow GNRs, where edge roughness dominates. The difference between full and isotropic dispersion decreases with increasing temperature. The trend is intuitively plausible, as orientation-dependent edge-roughness scattering dominates at low temperatures, while the momentum-randomizing three-phonon scattering take over as the temperature increases. We also note that the thermal conductivity of ZGNRs is higher than that of AGNRs, in agreement with the results of atomistic studies. [82, 83, 84, 85]

3.6.5 Bulk Limit

As we both L and W become large enough, thermal transport is at the diffusive-limit and the edge becomes irrelevant. The calculations from both edge structures converge to the smooth-edge limit and the resultant thermal conductivity κ_{diff} indicates the upper limit of that could obtained in graphene samples. As we have mentioned, almost all samples in experiments [66, 68, 67, 69, 7, 8] are still in the quasiballistic regime, so κ_{diff} is higher than all experimental data. In Fig.3.17 we show the comparison with predicted upper limit of thermal conductivity from Dorgan $et\ al.$ [10] We see that the difference reduces as the temperature increases, because the phonon MFP decreases as the temperature increases. As a result, for a

given sample length, transport moves from quasiballisic to diffusive at higher temperatures, therefore the measured values are closer to the calculated diffusive upper limit. Another insight we can take from Fig. 3.17 is that thermal transport is indeed isotropic for infinitely large graphene, which was predicted by first-principles calculations[86].

3.7 Conclusion to Chapter 3

We studied phonon transport in suspended single-layer graphene and micron-sized GNRs using the full-dispersion PMC technique. The calculated thermal conductivity is in good agreement with experimental measurements of Chen et al. [9, 7] and Xu et al. [8] We captured the ballistic-to-diffusive crossover in thermal conductivity and found that the diffusive limit at room temperature is not reached in most experiments, as lengths over 100 lm are needed. Consequently, the diffusive upper limit is likely higher than predicted, [10] and we calculate it for temperatures up to 600 K. We show that the GNR orientation matters for thermal transport, with ZGNRs having higher thermal conductivity than AGNRs in micron-sized systems, which is the same trend observed in atomistic calculations. The error made by employing the isotropic dispersion approximation for transport in GNRs is not large at room temperature, but the results with isotropic dispersions generally overestimate thermal conductivity and quite considerably so at low temperatures and in narrow GNRs. The fulldispersion PMC technique, presented here in detail, combines an efficient transport kernel (including inelastic and elastic scattering, as well as enabling the incorporation of real-space edge features) with an accurate account of phonon dispersions. This technique is a good choicein terms of accuracy, computational efficiency, and adaptability to different materials or geometries for analyzing systems with pronounced directional sensitivity (such as GNRs, or generally semiconductor membranes and nanowires), which have rough boundaries and are too large to address using atomistic techniques.

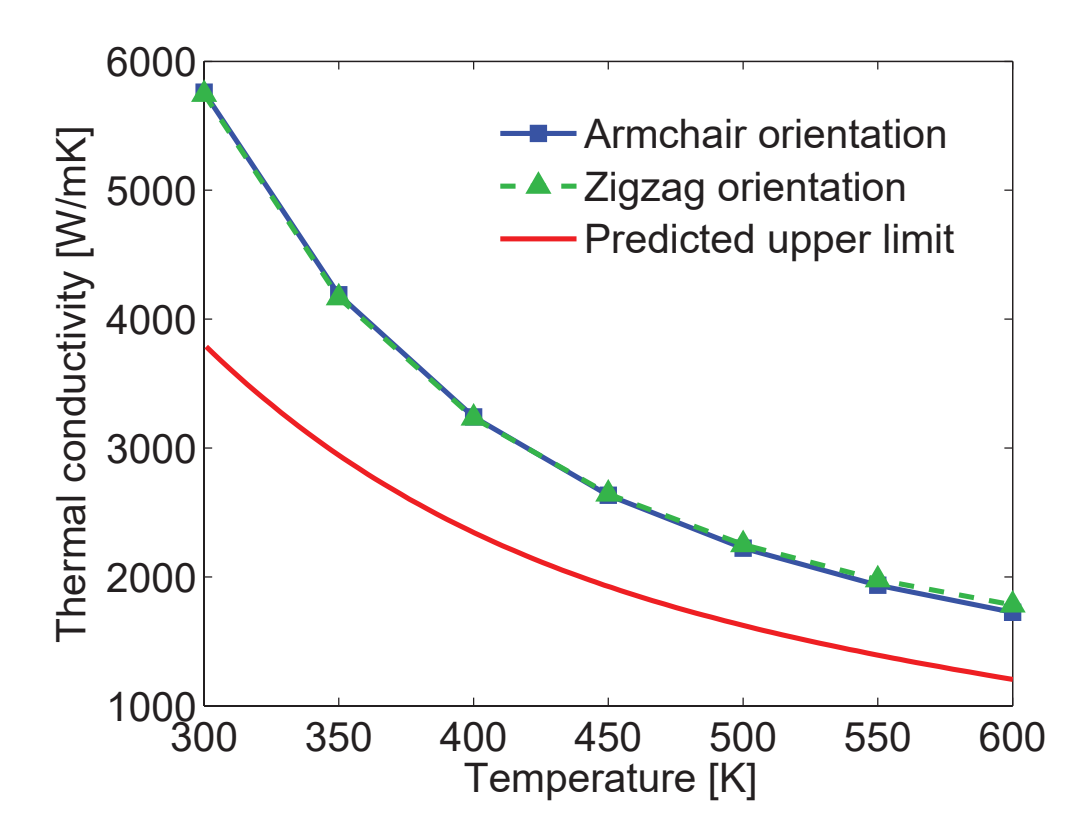


Figure 3.17: Thermal conductivity for suspended pristine bulk graphene from the PMC simulation (squares – armchair direction, triangles – zigzag direction) and the maximal thermal conductivity predicted by Dorgan *et al.*.[10]

Chapter 4

Thermal Conductivity of III-V Bulk Materials: 3D RTA with Full Dispersion

III-V arsenide (III-As) ternary alloys and their superlattices (SLs) are widely used in optoelectronic and thermoelectric devices.[87, 88] In particular, the use of these III-As alloys brings about great flexibility in designing the active region of quantum cascade lasers (QCLs).[89] In quantum cascade lasers (QCLs), self-heating is the main issue limiting the development of room-temperature (RT) continuous-wave (CW) lasing, which is exacerbated by the poor thermal conduction through the active core where hundreds of interfaces are present in a typical structure. [90, 12, 91] Despite the wide popularity, even the bulk thermal properties of these ternary alloys are poorly understood and characterized, leading to trouble analyzing the thermal performance of these devices.

In this chapter, we present a semiclassical model describing thermal conductivity of III-V compound semiconductors, and apply it to III-As systems. The PBTE is solved in the RTA; thermal conductivity of both binary and ternary III-As materials is well described with the model. This chapter lays the foundation of Chapter 5 where we investigate the crucial influence interfaces have on the thermal transport in III-As SLs.

4.1 Phonon Scattering Rate in III-V Materials

Same as in graphene, the total scattering rate for a given phonon equals the summation of the contribution from all scattering mechanisms (Eq. 3.6). Here we consider both U

and N three-phonon scattering processes, mass-difference scattering (from both isotopes and alloying), and scattering from charged carriers and ionized dopants. The following subsections provide the scattering rates and parameters we used for each mechanism. Note III-V materials are 3D materials, we consider 2 TA branches and 1 LA branch (see Sec. 1.1).

It should be noted that even though we consider only III-As materials (AlAs, GaAs, and InAs to be specific) in this work, the general methodology and scattering rates should be applicable to other III-V bulk materials or group-IV semiconductors (e.g. Si, Ge) and their alloys (e. g. Si_xGe_{1-x}) as well.

4.1.1 Phonon-Phonon Scattering

The scattering rate due to the U process is [92]

$$\tau_{\mathrm{b,U}}^{-1}(\mathbf{q},T) = \frac{\hbar \gamma_{\mathrm{b}}^2 \omega_{\mathrm{b}}^2(\mathbf{q})}{\overline{M}\Theta_{\mathrm{b,D}} v_{\mathrm{s,b}}^2} T e^{-\Theta_{\mathrm{b,D}}/3T},\tag{4.1}$$

the same as that in graphene (Eq. 3.7). The mode-dependent sound velocity $v_{s,b}$ and Debye temperature are both obtained from calculated dispersion.

The scattering rate due to the N process is [93, 94]

$$\tau_{\mathrm{b,N}}^{-1}(\mathbf{q}, \mathrm{T}) = \begin{cases} B_{\mathrm{N}}^{\mathrm{T}}\omega_{\mathrm{b}}(\mathbf{q})T^{4}, & \mathrm{b} = \mathrm{TA}, \\ B_{\mathrm{N}}^{\mathrm{L}}\omega_{\mathrm{b}}^{2}(\mathbf{q})T^{3}, & \mathrm{b} = \mathrm{LA}, \end{cases}$$
(4.2)

where

$$B_{\rm N}^{\rm T} \sim \frac{k_B^4 \gamma_{\rm T}^2 \Omega_0}{\bar{M} \hbar^3 v_{\rm T}^5(\mathbf{q})},$$
 (4.3a)

and

$$B_{\rm N}^{\rm L} \sim \frac{k_B^3 \gamma_{\rm T}^2 \Omega_0}{\bar{M} \hbar^2 v_{\rm I}^5(\mathbf{q})}.$$
 (4.3b)

Here, Ω_0 is the average volume occupied by an atom in the lattice. We assume the same Grüneissen parameter γ_b for both N and U processes in a given branch. However, in the case of III-V materials, the experimentally measured γ_b vary a lot.[95, 96, 97] In practice, we start with a reference value and slightly adjusted it to get the best fit to the experimentally obtained thermal conductivity (see Table 4.1). In our calculations, B_N^T is on the order of

 $10 \times -14 \text{ s}^{-1}\text{K}^{-3}$ and B_{N}^{L} is on the order of $10 \times -26 \text{ s}^{-1}\text{K}^{-5}$, varying slightly as the group velocity and mass difference changes for different materials (see Table 4.1).

4.1.2 Mass-Difference Scattering

There are two major sources of mass-difference scattering in compound semiconductors: the natural occurrence of isotopes and the fact that the compound is formed with different elements and they have different masses. The scattering rate of a phonon due to mass-difference is [98, 99]

$$\tau_{b,M}^{-1}(\mathbf{q}) = \frac{\pi}{6} \Omega_0 \Gamma_M \omega_b^2(\mathbf{q}) D_b(\omega_b(\mathbf{q})), \tag{4.4}$$

where $\Gamma_{\rm M}$ is the total mass parameter, obtained by summing over all mass parameters.

For a single element A with an average mass of $\bar{M}_A = \sum_i f_i M_{i,A}$, where f_i and $M_{i,A}$ are the abundance and the mass of the *i*th isotope of element A, the isotope mass parameter is

$$\Gamma_{\rm I}({\rm A}) = \sum_{i} f_{\rm i} (1 - M_{\rm i,A}/\bar{M}_{\rm A})^2.$$
 (4.5)

For a compound with the form of $A_xB_yC_z...$, the effective isotope mass parameter can be expressed as [100]

$$\Gamma_{\rm iso} = \frac{1}{x+y+z+\dots} \left[x \left(\frac{\bar{M}_{\rm A}}{\bar{M}} \right)^2 \Gamma_{\rm I}(A) + y \left(\frac{\bar{M}_{\rm B}}{\bar{M}} \right)^2 \Gamma_{\rm I}(B) + z \left(\frac{\bar{M}_{\rm C}}{\bar{M}} \right)^2 \Gamma_{\rm I}(C) + \dots \right], \tag{4.6}$$

where

$$\bar{M} = \frac{x\bar{M}_{A} + y\bar{M}_{B} + z\bar{M}_{C} + \dots}{x + y + z + \dots}$$
 (4.7)

is the average atom mass in the compound.

Here we are interested in both binary and ternary III-As compounds, so the general form of the compound becomes $A_xB_{1-x}As$, $(0 \le x \le 1)$. Since the element As has only one stable isotope ⁷⁵As[101], our total isotope mass parameter simplifies to

$$\Gamma_{\rm iso} = \frac{2}{\left[x\bar{M}_{\rm A} + (1-x)\bar{M}_{\rm B} + M_{\rm As}\right]^2} \left[x\bar{M}_{\rm A}^2\Gamma_{\rm I}(A) + (1-x)\bar{M}_{\rm B}^2\Gamma_{\rm I}(B)\right]. \tag{4.8}$$

In binary (x = 0 or x = 1) compounds, isotope scattering is dominant at low temperatures (< 150 K). In ternary (0 < x < 1) compounds, group III elements A and B forms a random alloy and introduces alloy mass scattering. The alloy mass-difference parameter is [21, 22]

$$\Gamma_{\text{alloy}} = x(1-x) \left[(\Delta M/\bar{M}_{\text{III}})^2 + \epsilon (\Delta a/\bar{a})^2 \right], \tag{4.9}$$

where

$$\Delta M = \bar{M}_{A} - \bar{M}_{B},$$

$$\bar{M}_{III} = x\bar{M}_{A} + (1-x)\bar{M}_{B},$$

$$\Delta a = a_{A} - a_{B},$$

$$\bar{a} = xa_{A} + (1-x)a_{B}.$$
(4.10)

Here $a_{\rm A}$ and $a_{\rm B}$ are the lattice constant of binary compounds AAs and BAs, respectively. ϵ is an empirically determined constant which captures the scattering caused by the mismatch of lattice constants. Here we take $\epsilon = 45$ for the III-V compounds following Abeles.[21] Relative abundance of isotopes is taken as: 26 Al: 0.001, 27 Al: 0.999; 71 Ga: 0.3989, 69 Ga: 0.6011; 113 In: 0.0429, 115 In: 0.9571.

4.1.3 Dopant and Electron Scattering

When the III-V compound semiconductors are doped (we consider n—type only for our applications of interest), group-III atoms may be randomly replaced by group-IV dopant, creating extra free electrons. Doping introduces two extra scattering mechanisms, phonon-electron interaction and impurity mass-difference scattering. At low doping levels, the relaxation time due to phonon-electron interaction can be expressed as [102]

$$\tau_{\rm b,ph-e}^{-1}(\mathbf{q}) = \frac{N_{\rm D}\xi_{\rm def}^2}{\rho v_{\rm b}^2(\mathbf{q})k_B T} \sqrt{\frac{\pi m^* v_{\rm b}^2(\mathbf{q})}{2k_B T}} \exp\left(-\frac{m^* v_{\rm b}^2(\mathbf{q})}{2k_B T}\right). \tag{4.11}$$

Here $N_{\rm D}$ represents the doping concentration, $\xi_{\rm def}$ is the deformation potential, ρ is the density of the crystal, and m^* is the electron effective mass in the crystal. For ternary materials, m^* is obtained from weighted average of those in the constituent binary materials.[103]

The impurity mass-difference scattering yields an additional contribution to the total mass parameter discussed in the previous section,[104]

$$\Gamma_{\rm imp} = \frac{N_{\rm D}}{N_0} \left(\frac{\delta M}{\bar{M}}\right)^2. \tag{4.12}$$

 $N_0 = 1/\Omega_0$ is the concentration of native atoms, and $\delta M = M_{\rm D} - \bar{M}_{\rm III}$ is the mass difference between the dopant and the average mass of group-III atoms being replaced. Our assumed n-type dopant is Si where $\bar{M}_{\rm Si} = 28.085$.

The effect of scattering introduced by doping is negligible when the impurity level is below 10^{17} , and still small compared to other scattering rates when then doping level exceeds 10^{18} , agree well with the result shown in experiment.[15]

4.2 Thermal Conductivity of Binary Compounds

In III-V semiconductor compounds, where acoustic phonons carry the vast majority of the heat. [93, 11] As derived previously in Sec. 2.1, the full thermal conductivity tensor of a crystalline semiconductor at temperature T can therefore be calculated as [105]

$$\kappa^{\alpha\beta}(T) = \sum_{\mathbf{b},\mathbf{q}} C_{\mathbf{b}}(\mathbf{q}, T) \tau_{\mathbf{b}}(\mathbf{q}, T) v_{\mathbf{b}}^{\alpha}(\mathbf{q}) v_{\mathbf{b}}^{\beta}(\mathbf{q}), \tag{4.13}$$

where $C_{\rm b}(\mathbf{q},T)$ is the phonon heat capacity for branch b given as

$$C_{\rm b}(\mathbf{q},T) = \frac{\partial \left[\frac{\hbar \omega_{\rm b}(\mathbf{q})}{e^{(\hbar \omega_{\rm b}(\mathbf{q})/k_B T)}} \right]}{\partial T} = \frac{\left[\hbar \omega_{\rm b}(\mathbf{q}) \right]^2}{k_B T^2} \frac{e^{\hbar \omega_{\rm b}(\mathbf{q})/k_B T}}{\left[e^{\hbar \omega_{\rm b}(\mathbf{q})/k_B T} - 1 \right]^2}.$$
 (4.14)

 $\tau_{\rm b}({\bf q},T)$ is the total phonon relaxation time and $v_{\rm b}^{\alpha}({\bf q})$ is the phonon group velocity along the α direction for given mode and wave vector. Both the heat capacity and the group velocity are calculated from the exact phonon dispersion relation using the adiabatic bond charge model (ABCM).[106, 107] We numerically evaluate Eq. (4.13) over the first Brillouin Zone (1BZ) to obtain one entry in the bulk thermal conductivity tensor. When dealing with ternary compounds ($A_xB_{1-x}C$), the parameters in ABCM are calculated in the virtual crystal approximation (VCA).[21]

Material	GaAs	InAs	AlAs
$\gamma_{\mathrm{TA1}} \; (\mathrm{exp.})$	0.57	0.58	0.46
$\gamma_{ m TA1} \; (ab \; initio)$	0.52	0.46	0.46
$\gamma_{\rm TA2}~({\rm exp.})$	0.57	0.58	0.46
$\gamma_{\mathrm{TA2}} \; (ab \; initio)$	0.52	0.46	0.46
$\gamma_{\rm LA}~({ m exp.})$	1.35	1.6	1.35
$\gamma_{ m LA}~(ab~initio)$	1.3	1.35	1.35
$\Theta_{\mathrm{TA1,D}}$ (K)	141.21	103.93	181.59
$\Theta_{TA2,D}$ (K)	167.76	124.64	215.21
$\Theta_{\mathrm{LA,D}}$ (K)	304.96	253.16	380.07
$B_{\rm N}^{\rm TA1} \ (10 \times -14 \ {\rm s}^{-1} {\rm K}^{-3})$	0.421	1.33	0.166
$B_{\rm N}^{\rm TA2}~(10\times-14~{\rm s}^{-1}{\rm K}^{-3})$	0.443	1.39	0.173
$B_{\rm N}^{\rm LA}~(10\times-26~{\rm s}^{-1}{\rm K}^{-5})$	1.27	2.85	7.04
$v_{\mathrm{TA1}}~(\mathrm{m/s})$	3397.3	2817.5	4318.2
$v_{ m TA2}~({ m m/s})$	3361.9	2793.0	4284.7
$v_{ m LA}~({ m m/s})$	5418.2	4708.7	6812.4
a_0 (Å)	5.6532	6.0583	5.6611
$\Omega_0 = a_0^3/4 \ (10 \times^{-29} \mathrm{m}^3)$	4.5168	5.5589	4.5357
$m^* (m_0 = 9.1 \times 10^{-31} \text{ kg})$	0.063	0.023	0.1
\bar{M} (a.u. = 1.66054×10^{-27} kg)	69.7978	144.9142	26.999
$\rho~(10^3~{\rm kg/m^3})$	5.3232	5.673	43.7342

Table 4.1: Material parameters used in the calculation.

We apply the scattering rates (Sec. 4.1) and the thermal conductivity model (Eq. 4.13) to three binary arsenide compounds—GaAs, AlAs, and InAs—whose thermal properties have been extensively studied both experimentally[15, 14, 13, 108, 12, 20, 18, 19, 17] and via ab inito calculations[11]. We find that thermal conductivity of bulk III-V binary materials is quite isotropic: diagonal terms in the thermal conductivity tensor are the same while off-diagonal terms are negligible. As a result, we report the thermal conductivity as a single number ($\kappa = \kappa^{xx} = \kappa^{yy} = \kappa^{zz}$).

4.2.1 Thermal Conductivity of GaAs

Figure 4.1 shows the thermal conductivity of GaAs obtained from our full dispersion calculations together with the experimental results from Amith *et al.*,[15] Carlson *et al.*,[14] Inyushkin *et al.*,[13] and the *ab inito* results of Lindsay *et al.*[11]. By slightly adjusting the Grüneissen parameter, we can get thermal conductivity that agrees very well with either experiment (green curve) or first-principles calculations (light-blue curve). Purple curve shows our calculation from an isotropic dispersion approximation (see Sec. B).

4.2.2 Thermal Conductivity of AlAs

Similarly, Fig. 4.2 compares the calculated thermal conductivity of AlAs (blue curve) with analytical fit from Evans *et al.* (orange curve),[12] experimental data from Afromowitz,[16] and *ab inito* calculations (green curve).[11] Purple curve is again showing the results from isotropic dispersion approximation (see Sec. B).

4.2.3 Thermal Conductivity of InAs

Figure 4.3 shows the thermal conductivity of InAs from our calculation ($\gamma_{TA} = 0.56$, $\gamma_{LA} = 1.60$ for blue curve and $\gamma_{TA} = 0.46$, $\gamma_{LA} = 1.35$ for red curve) compared with *ab initio* results from Lindsay *et al.* (green curve), [11] experimental data from Heckman *et al.* (yellow triangles), [17] Tamarin *et al.* (brown circles), [18] Guillou *et al.* (pink diamonds), [19] and

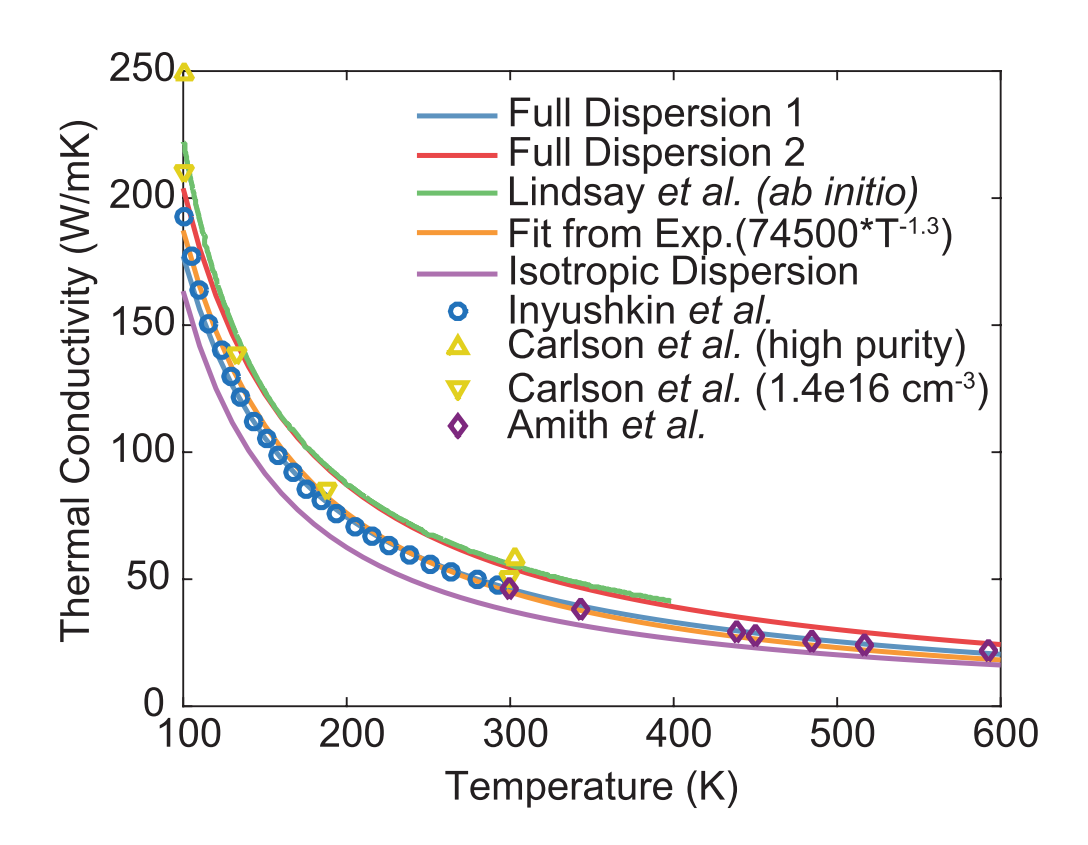


Figure 4.1: Thermal conductivity of bulk GaAs based on our calculation with full dispersion; $\gamma_{\text{TA}} = 0.57$, $\gamma_{\text{LA}} = 1.35$ (blue curve) and $\gamma_{\text{TA}} = 0.52$, $\gamma_{\text{LA}} = 1.30$ (red curve). The green curve shows the *ab initio* results from Lindsay *et al.*.[11] The orange curve is an analytic fit to the experimental data of Evans *et al.*[12] The purple curve is the calculated thermal conductivity based on our model and with the isotropic dispersion approximation (see Appendix B). Blue circles, yellow triangles, and blue diamonds correspond to the experimental data from Inyushkin *et al.*,[13] Carlson *et al.*,[14] and Amith *et al.*,[15] respectively.

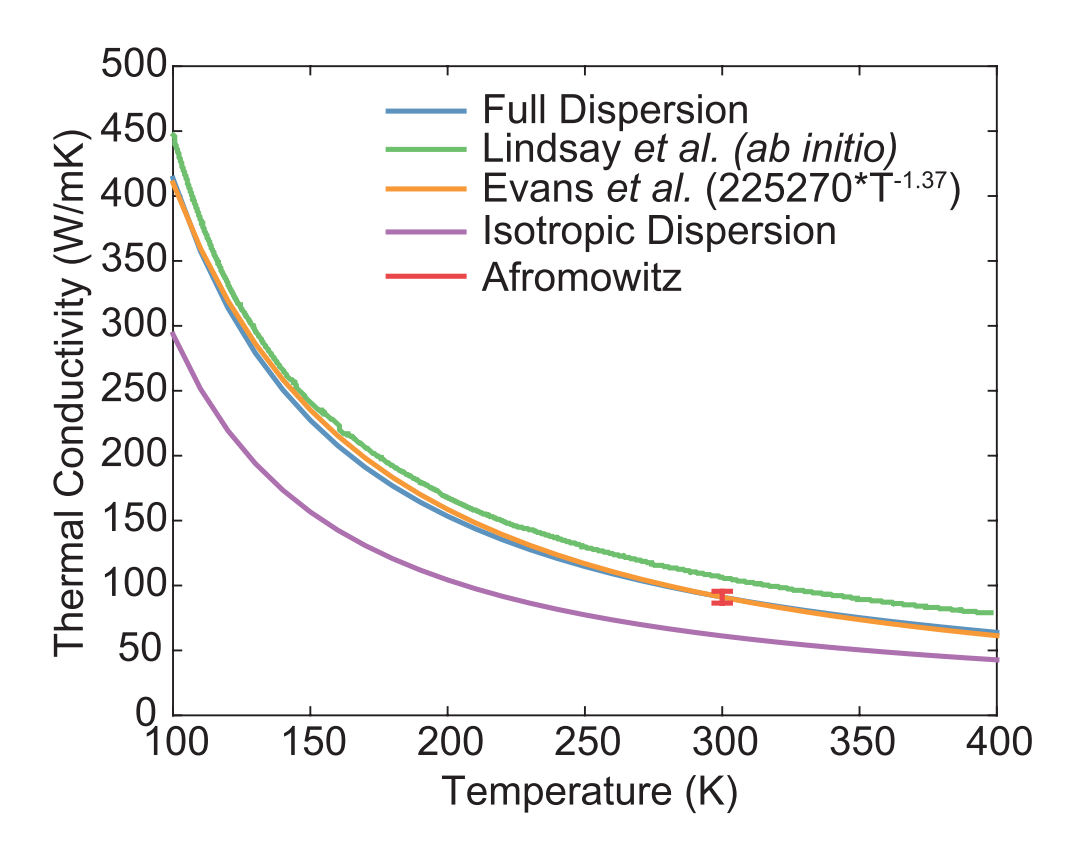


Figure 4.2: Thermal conductivity of bulk AlAs based on our calculation with full dispersion. $\gamma_{TA} = 0.46$ and $\gamma_{LA} = 1.35$ (blue curve). In green, orange, and purple we show the *ab initio* data from Lindsay *et al.*,[11] an analytic fit to the experimental data from Evans *et al.*,[12] and the calculation with isotropic dispersion approximation (see Appendix B), respectively. The red symbol shows experimental data from Afromowitz.[16]

Bowers *et al.* (orange squares),[20] respectively. Purple curve shows the isotropic dispersion approximation (see Sec. B).

4.3 Thermal Conductivity of Ternary Alloys

III-V ternary compounds are typically random alloys; in our case, we are interested in the alloy of two III-As binary compounds. In the lattice, the anion cites are always taken by an As atom while the cation cites can be randomly taken by either of the group-III atoms. As a result of the mass-difference between group-III atoms, alloy scattering is the dominant mechanism that influences the thermal conductivity of ternary arsenide compounds.

Unfortunately, very few experiments [4, 21, 16, 22] have been carried out on these materials and they were all performed at room temperature (RT). We calculate thermal conductivity of $In_xGa_{1-x}As$, $Al_xGa_{1-x}As$, and $In_xAl_{1-x}As$ at RT with various compositions and compare with experimental results. [4, 21, 16, 22]

4.3.1 Thermal Conductivity of InGaAs

Figure 4.4 shows our calculated thermal conductivity of bulk $In_xGa_{1-x}As$ with varying In compositions (purple diamonds) compared with the theoretical results from Abeles (blue curve) [21] and the experimental results from Adachi (red curve) [22] and Abrahams *et al.* (orange dots) [4]. Our calculations agree well with the available experimental data over a wide range of compositions.

4.3.2 Thermal Conductivity of AlGaAs

Figure 4.5 shows our calculated thermal conductivity of bulk $Al_xGa_{1-x}As$ with varying Al compositions (red diamonds) compared with the experimental results from Afromowitz et al.[16]. The agreement is good over the whole composition range as well.

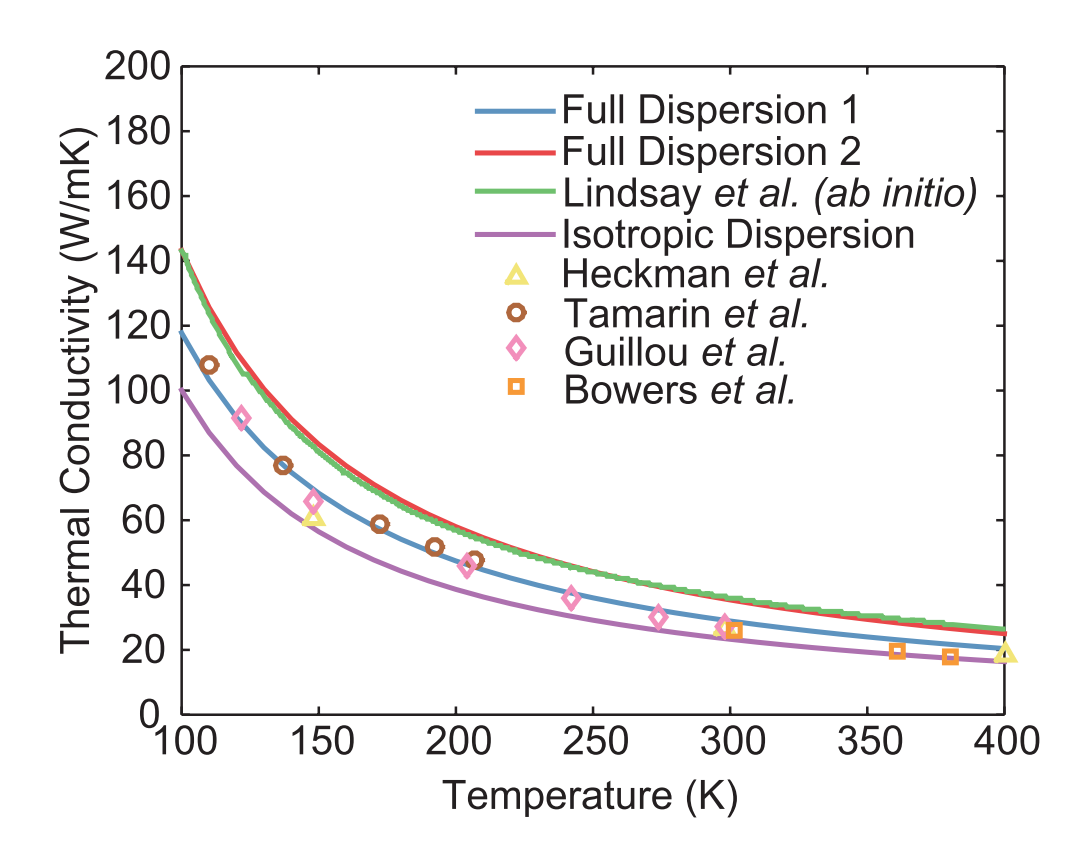


Figure 4.3: Thermal conductivity of bulk InAs based on our calculation with full dispersion; $\gamma_{TA} = 0.56$, $\gamma_{LA} = 1.60$ (blue curve) and $\gamma_{TA} = 0.46$, $\gamma_{LA} = 1.35$ (red curve). The green curve shows the *ab initio* results from Lindsay *et al.*.[11] The purple curve shows the calculated thermal conductivity with the isotropic dispersion approximation (see Appendix B). Yellow triangles, brown circles, pink diamonds, and orange squares correspond to the experimental data from Heckman *et al.*,[17] Tamarin *et al.*,[18] Guillou *et al.*,[19] and Bowers *et al.*,[20] respectively.

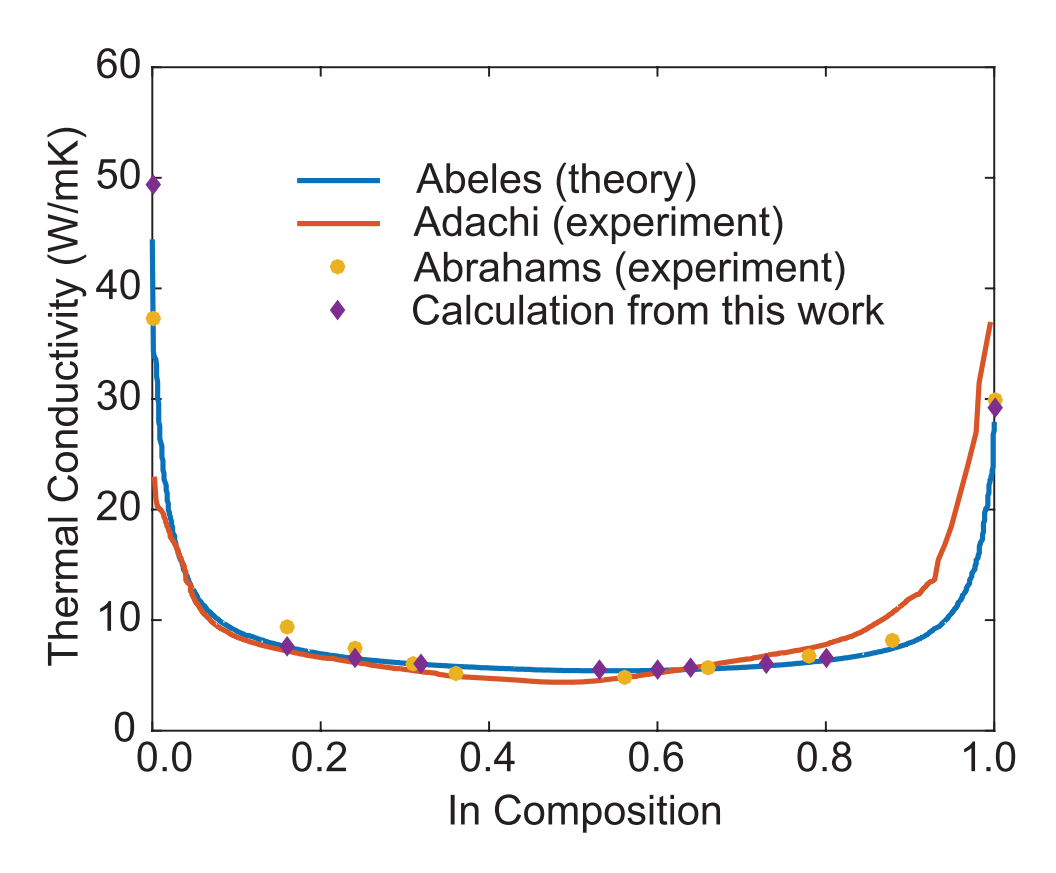


Figure 4.4: Thermal conductivity of bulk $In_xGa_{1-x}As$ with varying In composition. The blue curve shows the theoretical results from Abeles.[21] The red curve and orange dots present the experimental results from Adachi[22] and Abrahams *et al.*,[4] respectively. Purple diamonds represent the results of our calculation.

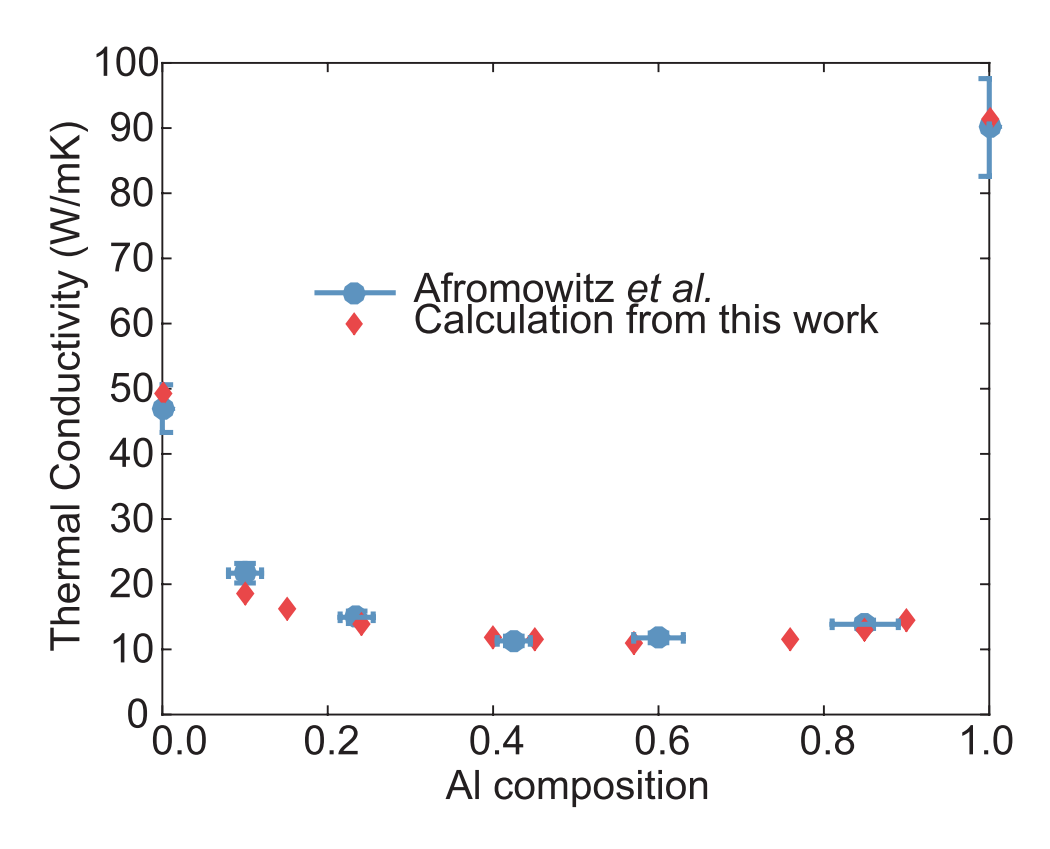


Figure 4.5: Thermal conductivity of bulk $Al_xGa_{1-x}As$ with varying Al composition. Blue dots and red diamonds show the experimental data of Afromowitz *et al.*[16] and the results of our calculation, respectively.

4.3.3 Thermal Conductivity of InAlAs

To our knowledge, no systematic measurements of the thermal conductivity of $In_xAl_{1-1}As$ have been carried out thus far. Figure 4.6 shows our calculated thermal conductivity of $In_xAl_{1-1}As$ with varying In composition. Note that upon further analysis, these results likely overestimate the thermal conductivity due to the VCA mass-difference scattering rate this model implements (see Sec. 4.1.2). More discussion on this can be found in Sec. 5.

4.4 Conclusion to Chapter 4

We solve the PBTE under the RTA to describe the thermal conductivity of III-As (AlAs, GaAs, and InAs) compound semiconductors. The obtained temperature-dependent thermal conductivity agree well with experimental measurements over the temperature range between 100 K and 400 K. We also calculate the thermal conductivity of III-As ternary alloys ($Al_xGa_{1-x}As$, $In_xGa_{1-x}As$, and $In_xAl_{1-x}As$) with different composition x under the VCA at room temperature. For $Al_xGa_{1-x}As$ and $In_xGa_{1-x}As$, the calculated results agree well with experimental data.[16, 4, 22] For $In_xAl_{1-x}As$, experimental results only exist for $In_{0.52}Al_{0.48}As$ (lattice-matched to InP) and do not agree with each other.[5, 27] We will revisit the results for $In_xAl_{1-x}As$ in the next two chapters.

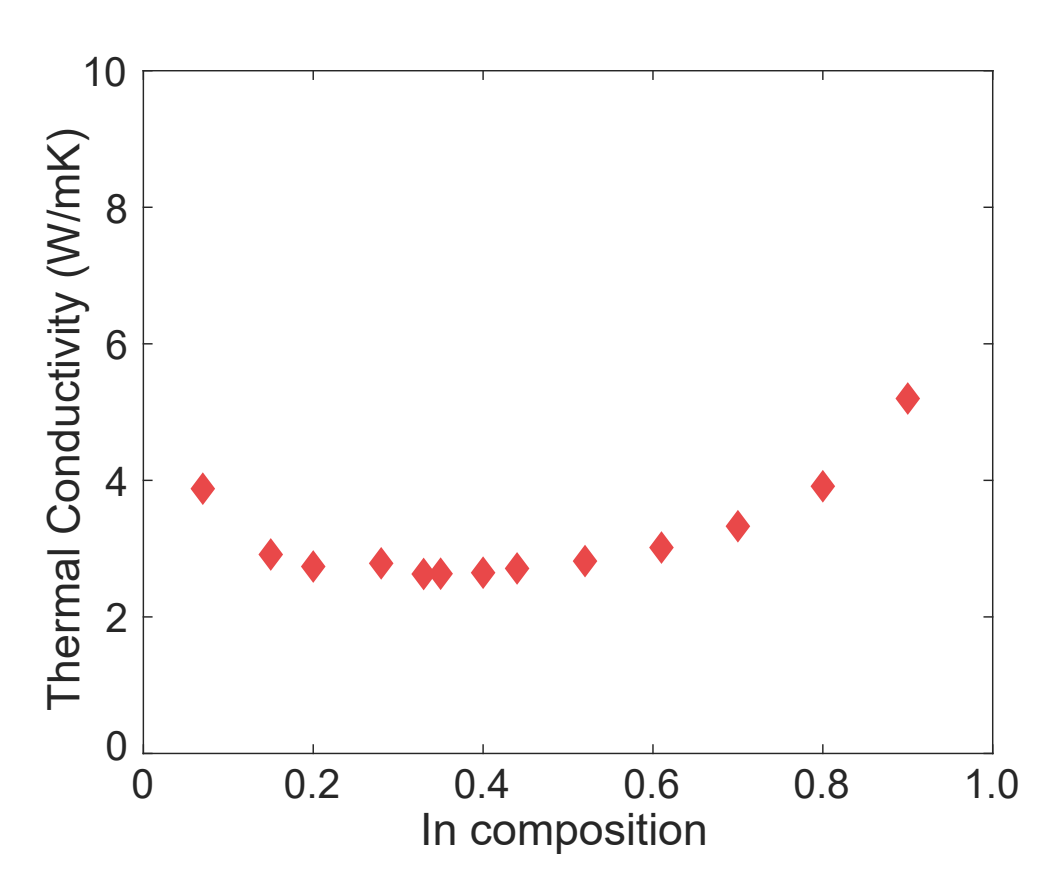


Figure 4.6: Thermal conductivity of bulk $In_xAl_{1-x}As$ with varying In composition from our calculation.

Chapter 5

Thermal Conductivity of III-V Superlattices (SLs): 3D RTA with Full Dispersion

A semiconductor superlattice (SL) is a periodic structure, with each period consisting of two or more thin layers of different materials. III-V semiconductor SLs have been widely used in electronic and photonic devices. [109, 87, 110, 88] Thermal transport in SLs exhibits pronounced anisotropy: the cross-plane thermal conductivity (the thermal conductivity in the SL growth direction, normal to each planar layer) is much lower than the in-plane thermal conductivity.[111] Advanced experimental techniques have enabled the measurements of the in-plane[112] and cross-plane[113, 114] thermal conductivity on several material systems. These results show that thermal conductivity of a SL is substantially lower than that of a weighted average of the constituent bulk materials. [23, 115, 24, 26, 116, 25, 117, 91, 1, 27] Theoretical studies show that the interfaces between adjacent layers are responsible for both the overall reduction and the anisotropy of thermal conductivity. [118, 33, 119] In this chapter, we offer a model that quantitatively captures both effects of the interfaces in III-V SLs. The bulk thermal conductivity of the III-V materials (both binary compounds and ternary alloys) making up the SLs are obtained through solving the PBTE in the RTA. The influence of interfaces is captured through a single free parameter—the effective rms roughness Δ of the interface.

5.1 Model Overview

We break down the thermal conductivity of SLs to two main parts, the layer thermal conductivity and the thermal boundary resistance (TBR). Layer thermal conductivity is reduced from the bulk value because of the (partially) diffuse interface scattering. The lowered layer thermal conductivity contributes to the lowering of thermal conductivity in both inplane and cross-plane direction. Additionally, TBR between adjacent layers is responsible for the pronounced cross-plane thermal-conductivity reduction. [118, 33, 120, 111]

The interfacial transport behavior in SLs is largely dependent on the material system and the interface quality.[111] The acoustic mismatch model (AMM) and the diffuse mismatch model (DMM) have been traditionally used to calculate the phonon transmission coefficient and the resulting TBR of an interface.[121, 122] These two models are believed to yield the lower and upper limits of the TBR, respectively, but do not satisfactorily explain realistic experimental results.[120] Molecular dynamics (MD) simulations[119, 123, 124, 125, 126, 127] have provided valuable insights into heat transport across a number of solid-solid interfaces. The non-equilibrium Green's function technique (NEGF) has also been applied to describe the phonon dynamics,[128, 129] generally without phonon-phonon scattering. In general, atomistic simulations are limited by computation burden, which makes it hard to study complicated SL structures, such as the active region of solid-state lasers.[87, 88]

We build our semiclassical model on top of the previous description of thermal conductivity in III-V bulk materials (see Sec. 4). The in-plane thermal conductivity is obtained from connecting the layers in parallel while the cross-plane conductivity is calculated from connecting the layers and the TBRs in series. The TBR of each interfaces is calculated by interpolating between the AMM and DMM transmission coefficients at the interface. Both the partially diffuse interface scattering and the AMM-DMM interpolation are described with the aid of the same momentum-dependent specularity parameter, wherein there is a single adjustable parameter – an effective interface rms roughness. The model can effectively

describe complicated systems with an arbitrary number of interfaces and random layer thicknesses. Despite the model simplicity, the calculation results agree well with experimental data from multiple studies by different groups. [23, 115, 24, 26, 25, 1, 27]

Even though a typical layer thickness in III-V SL structures is on the order of a few nanometers, we argue that coherent phonon transport can be neglected and that the semi-classical pBTE provides an appropriate framework for analyzing heat flow in these systems over a range of temperatures. The reasons for this assertion are the following:

- 1. We are interested in the thermal conductivity of SLs near room temperature, where the phonon-phonon interaction is strong and breaks the phonon wave coherence.[130] Experiments find that coherent transport is prominent in GaAs/AlAs SLs only when T<100 K.[34] Considering that ternary III-V compounds have a much higher scattering rate than binary compounds, coherent transport phenomena in them would only show at even lower temperatures.
- 2. Even in best-quality lattice-matched SLs, there exist three or more interfacial layers, which effectively introduces atomic scale roughness.[131, 132, 133, 134, 135, 34] Phonons may suffer from phase-breaking interface scattering when they hit the rough interface.[136]
- 3. The phonon coherence length has been estimated to be smaller than 2 nm for GaAs,[118, 33] and the number should be even lower for SLs formed by ternary compounds, especially when there is strain in the SL. The SL structures we use to validate our model[23, 115, 24, 26, 25, 1, 27] have layer thicknesses equivalent to or thicker than that. Other SL structures that we are interested in [12, 137] also have relatively thick layers or only one thin layer among tens of thick layers, making the coherent transport contribution negligible.
- 4. In QCLs, the SL is formed with multiple periods, often called stages, with many layers in each stage and the layer thickness in each stage being highly variable, depending

on the desired optoelectronic properties.[12, 137] Consequently, the QCL SL structure behaves as a nearly random multilayer system in which coherent phonon transport is further suppressed.[138]

As a result of all the reasoning above, we do not consider phonon coherent transport or phonon confinement to analyze thermal transport. We use bulk dispersions and the phonon Boltzmann transport equation in the SL thermal conductivity calculations.

5.2 The Twofold Influence of Effective Interface Roughness

As mentioned briefly above, there will inevitably exist a few transition layers between adjacent materials in a SL structure.[131, 132, 133, 134, 135, 34] Figure 5.1 shows a schematic of interfaces between lattice-matched crystalline layers in SLs. In the transition region, if we drew a line that separated the atoms of one crystal from those of the other, we would get a jagged boundary. Therefore, we model the interface with an effective interface rms roughness Δ , which captures the basic properties of interfacial mixing. The thicker the transition layer, the higher the Δ . Most III-V SLs are grown by molecular beam epitaxy (MBE)[35] or metal-organic chemical vapor deposition (MOCVD),[36] both being well-controlled growth environments. As a result, all the interfaces in the SL should be nearly identical. Therefore, we use a single roughness Δ to model all the interfaces.

The probability of a phonon reflecting specularly from a rough interface is represented by a wave-number-dependent specularity parameter [139]

$$p_{\text{spec}}(\mathbf{q}) = \exp(-4\Delta^2 |\mathbf{q}|^2 \cos^2 \theta), \tag{5.1}$$

where $|\mathbf{q}|$ is the magnitude of the wave vector, and θ represents the angle between \mathbf{q} and the normal direction to the interface. This expression is nominally derived in the limit of uncorrelated roughness;[140, 139] but considering that more correlated surfaces scatter phonons more specularly,[141] surface correlation can effectively be captured by using a lowered Δ .[142]

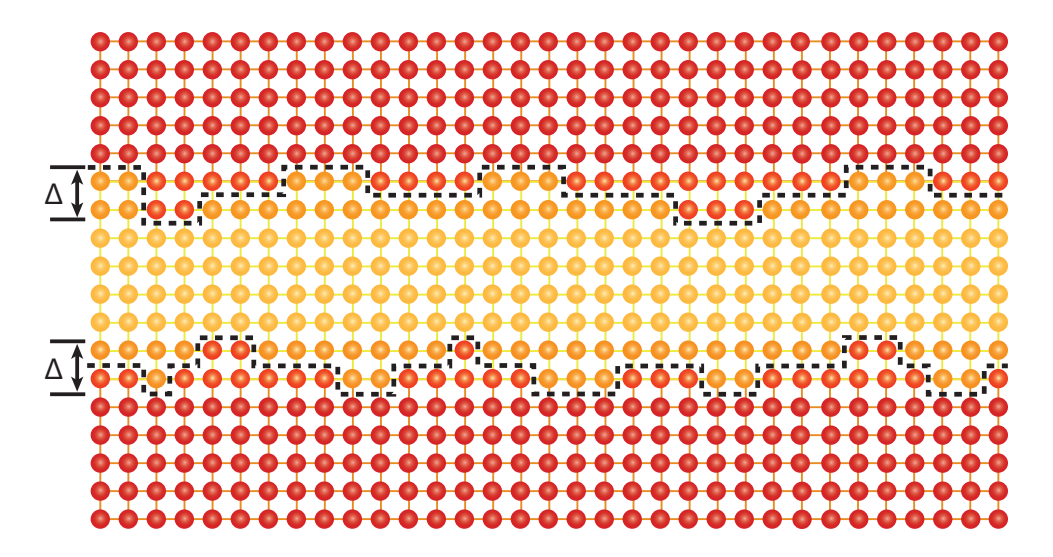


Figure 5.1: Even between lattice-matched crystalline materials, there exist nonuniform transition layers that behave as an effective atomic-scale interface roughness with some rms roughness Δ . This effective interface roughness lead to phonon momentum randomization and to interface resistance in cross-plane transport.

5.2.1 Layer Thermal Conductivity

Diffuse interface scattering affects all phonons in the SL and influences phonon mode occupation inside each layer. [143] The effect on interface roughness on mode population can be captured by solving the pBTE with appropriate boundary conditions. The result is an effective interface scattering rate [143] that captures the interplay between internal mechanisms described in Sec. 4.1 and interface roughness in a layer of thickness L:

$$\tau_{\text{interface}}^{-1}(\mathbf{q}) = \frac{v_{\text{b},\perp}(\mathbf{q})}{L} \frac{F_{\text{p}}(\mathbf{q}, L)}{1 - \frac{\tau_{\text{b,internal}}(\mathbf{q})v_{\text{b},\perp}(\mathbf{q})}{L} F_{\text{p}}(\mathbf{q}, L)},$$
(5.2a)

where

$$F_{p}(\mathbf{q}, L) = \frac{[1 - p_{spec}(\mathbf{q})]\{1 - \exp[-L/\tau_{b,internal}(\mathbf{q})v_{b,\perp}]\}}{1 - p_{spec}(\mathbf{q})\exp[-L/\tau_{b,internal}(\mathbf{q})v_{b,\perp}]}$$
(5.2b)

is a mode-dependent scaling factor. Here, b denotes the phonon branch and \mathbf{q} its wave vector, $v_{\mathrm{b},\perp}$ is the component of the phonon group velocity normal to the interface, and $\tau_{\mathrm{b,internal}}(\mathbf{q})$ is the total relaxation time due to internal scattering mechanisms in the layer (see Sec. 4.1). It is noteworthy that the effective rate of interface scattering (5.2a) depends on both roughness and the relative size of the layer thickness (L) to the mean free path for internal scattering $(\tau_{\mathrm{b,internal}}(\mathbf{q})v_{\mathrm{b},\perp})$: for very thin layers $(L/\tau_{\mathrm{b,internal}}(\mathbf{q})v_{\mathrm{b},\perp} << 1)$ the phonon "sees" both interfaces of a layer $(\tau_{\mathrm{interface}}^{-1}(\mathbf{q}) \to 2\frac{v_{\mathrm{b},\perp}(\mathbf{q})}{L}\frac{1-p_{\mathrm{spec}}(\mathbf{q})}{1+p_{\mathrm{spec}}(\mathbf{q})}$, a well-known expression derived by Ziman[140]), while for very thick layers $(L/\tau_{\mathrm{b,internal}}(\mathbf{q})v_{\mathrm{b},\perp} >> 1)$, the phonon will scatter many times due to internal mechanisms between successive interactions with interfaces, as if the interfaces were completely independent $(\tau_{\mathrm{interface}}^{-1}(\mathbf{q}) \to \frac{v_{\mathrm{b},\perp}(\mathbf{q})}{L}[1-p_{\mathrm{spec}}(\mathbf{q})])$. For details, see Ref. [143]. Through this additional effective scattering rate, rough interfaces that bound each layer affect phonon population and thus influence both in-plane and cross-plane thermal transport. [143] This is the first aspect of interfacial influence on thermal transport in SLs.

5.2.2 Thermal Boundary Resistance

The cross-plane thermal conductivity bears an additional influence of the interfaces.[122, 144] In order to carry heat along the cross-plane direction, phonons must cross interfaces. As there are two different materials on the two sides of the interface, the phonon transmission

probability through the interface is not unity, and a thermal boundary resistance emerges. There have been two widely accepted models – the AMM[121, 145] and the DMM – for the calculation of the phonon transmission coefficient and the TBR.[122]

From the AMM point of view, the interface is treated as a perfect plane and the phonons as plane waves. The transmission probability is determined from an analogue of Snell's law for electromagnetic waves. The AMM transmission probability for a phonon going from material 1 to material 2 can be expressed as:

$$t_{b,1\to 2}^{AMM}(\mathbf{q}) = \frac{4Z_{b,1}^{\perp}(\mathbf{q})Z_{b,2}^{\perp}(\mathbf{q})}{\left[Z_{b,1}^{\perp}(\mathbf{q}) + Z_{b,2}^{\perp}(\mathbf{q})\right]^{2}},$$
(5.3)

where $Z_{\mathrm{b},1/2}^{\perp} = \rho_{1/2} v_{\mathrm{b},1/2}^{\perp}(\mathbf{q})$ are the perpendicular acoustic impedances of sides 1 and 2. ρ is the mass density of a material.

On the other hand, in the DMM, the assumption is that the coherence at the interface is completely destroyed: a phonon loses all memory about its velocity and randomly scatters into another phonon with the same energy. The transmission coefficient can be derived from the principle of detailed balance as[146]

$$t_{1\to2}^{\text{DMM}}(\mathbf{q}) = \frac{v_{\text{b},2}(\mathbf{q})D_2(\omega_1(\mathbf{q}))}{v_{\text{b},2}(\mathbf{q})D_2(\omega_1(\mathbf{q})) + v_{\text{b},1}(\mathbf{q})D_1(\omega_1(\mathbf{q}))},$$
(5.4)

where $D_1(\omega)$ and $D_2(\omega)$ are the phonon densities of states in materials 1 and 2, respectively.

In reality, for a high-quality interface like that in a III-V SL structure, phonon interface scattering is neither purely specular nor completely diffuse; consequently, the AMM overestimates while the DMM underestimates the transmission coefficient. [147] In order to accurately model the TBR in a large temperature range and for various interfaces, we will interpolate between the two models for the transmission coefficient. [33, 148] We posit that the specularity parameter (5.1) can also be used to give weight to the probability of phonon transmission without momentum randomization, i.e., to the AMM transmission coefficient. In other words, we introduce an effective phonon transmission coefficient as

$$t_{\rm b}(\mathbf{q}) = p_{\rm spec}(\mathbf{q}) \cdot t_{\rm b}^{\rm AMM}(\mathbf{q}) + [1 - p_{\rm spec}(\mathbf{q})] \cdot t_{\rm b}^{\rm DMM}(\mathbf{q}). \tag{5.5}$$

This coefficient captures both the acoustic mismatch and the momentum randomization at a rough interface between two media. The rougher the interface, the lower the specularity parameter, and therefore the higher the TBR. The TBR will only be picked up by the phonons trying to cross an interface, thus having an influence on cross-plane transport only. This is the second effect the roughness has on the thermal transport.

5.3 Calculation of In-plane and Cross-plane Thermal Conductivities

In calculating SL thermal conductivity, we first calculate each layer's thermal conductivity in the same way as the bulk thermal conductivity of a material (Ch. 4), but with an additional scattering rate (5.2a) due to the presence of interfaces.[143] The layer thermal conductivity obtained this way will already be lower than the bulk thermal conductivity of the same material.

Second, the TBR is calculated using a transmission coefficient interpolated from the AMM and the DMM values. The TBR from material 1 to material 2, denoted $R_{1\to 2}$, is given by

$$R_{1\to 2}^{-1} = \frac{1}{2} \sum_{b,\mathbf{q}} \frac{v_{b,1,\perp}(\mathbf{q}) C_{b,T}(\mathbf{q}) t_{1\to 2}(\omega_1(\mathbf{q}))}{1 - \frac{1}{2} \langle t_{1\to 2}(\omega_1(\mathbf{q})) + t_{2\to 1}(\omega_1(\mathbf{q})) \rangle}.$$
 (5.6)

The denominator in the expression is a correction factor introduced following the modified definition of temperature of Simons[149] and Zeng and Chen,[150] as the phonon distribution at the interface is far from equilibrium. The correction ensures that the TBR vanishes at a fictitious interface inside a material. Here $\langle t_{1\to 2}(\omega_1(\mathbf{q})) + t_{2\to 1}(\omega_1(\mathbf{q})) \rangle$ represents the average value of transmission coefficients over the Brillouin zone.

With properly calculated layer thermal conductivity and the TBR, the in-plane and crossplane thermal conductivity of a SL with two layers per period can be written as [144, 143]

$$\kappa_{\text{in-plane}} = \frac{L_1 \kappa_1 + L_2 \kappa_2}{L_1 + L_2},\tag{5.7a}$$

$$\kappa_{\text{cross-plane}} = \frac{L_1 + L_2}{\frac{L_1 + L_2}{\kappa_{1+} + \frac{L_2}{\kappa_2} + (R_{1\to 2} + R_{2\to 1})}},$$
(5.7b)

where L_1 and L_2 are the layer thicknesses of materials 1 and 2, respectively, while κ_1 and κ_2 are the corresponding layer thermal conductivities. $R_{1\to 2}$ and $R_{1\to 1}$ represent the TBRs from layer 1 to layer 2 and from layer 2 to layer 1. The expressions can be extended to the situation of a SL with n layers of thicknesses L_i (i = 1, ..., n):

$$\kappa_{\text{in-plane}} = \frac{\sum_{i=1}^{n} L_i \kappa_i}{\sum_{i=1}^{n} L_i},\tag{5.7c}$$

$$\kappa_{\text{in-plane}} = \frac{\sum_{i=1}^{n} L_i \kappa_i}{\sum_{i=1}^{n} L_i},$$

$$\kappa_{\text{cross-plane}} = \frac{\sum_{i=1}^{n} L_i}{\sum_{i=1}^{n} L_i / \kappa_i + R_{i \to i+1}},$$
(5.7c)

with the understanding that $R_{n\to n+1} \equiv R_{n\to 1}$, owing to periodicity. It is also clear why SLs can act as thermal rectifiers: the layer sequence is important in Eq. (5.7d), as the cross-plane thermal conductivity is not the same in both directions, because the TBRs are generally not symmetric $(R_{i\to j} \neq R_{j\to i})$.

Results and Comparison with Experiments 5.4

We have compared the results from our simple model with several experimental results by different groups on both in-plane [23, 24, 1] and cross-plane [115, 26, 25, 1, 27] thermal conductivity of III-arsenide SLs and obtained good agreement.

5.4.1GaAs/AlAs Superlattices

Figure 5.2 shows the RT in-plane thermal conductivity of GaAs/AlAs SLs with various layer thicknesses. To compare with Yao's data, [23] we set the effective interface roughness to 6 A. The calculated data agrees well with experiment, except for the layer thickness of 20 nm. However, we argue that the in-plane thermal conductivity should first increase monotonically with increasing layer thickness, then saturate at the bulk value; yet, the

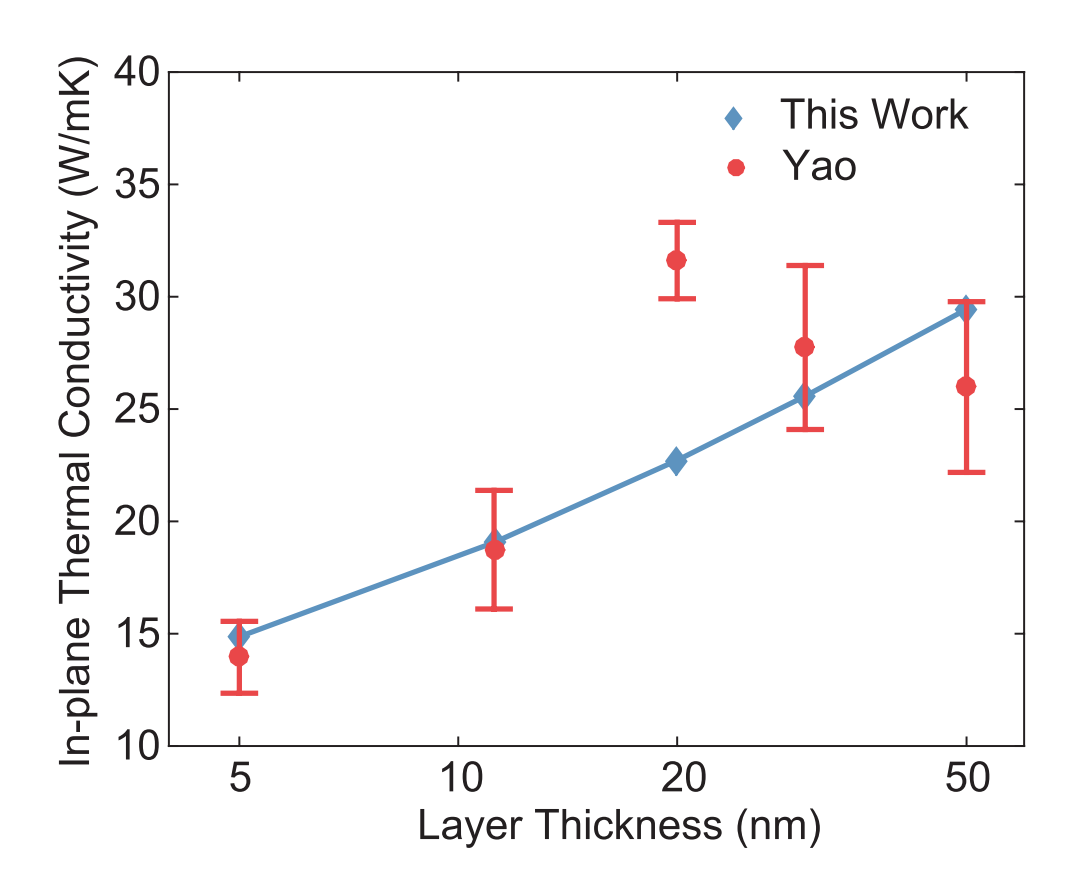


Figure 5.2: In-plane thermal conductivity of GaAs/AlAs superlattices as a function of layer thickness. Red dots are the experimental data from Yao [23] and blue diamonds are our calculated data with $\Delta=6\,\text{Å}$.

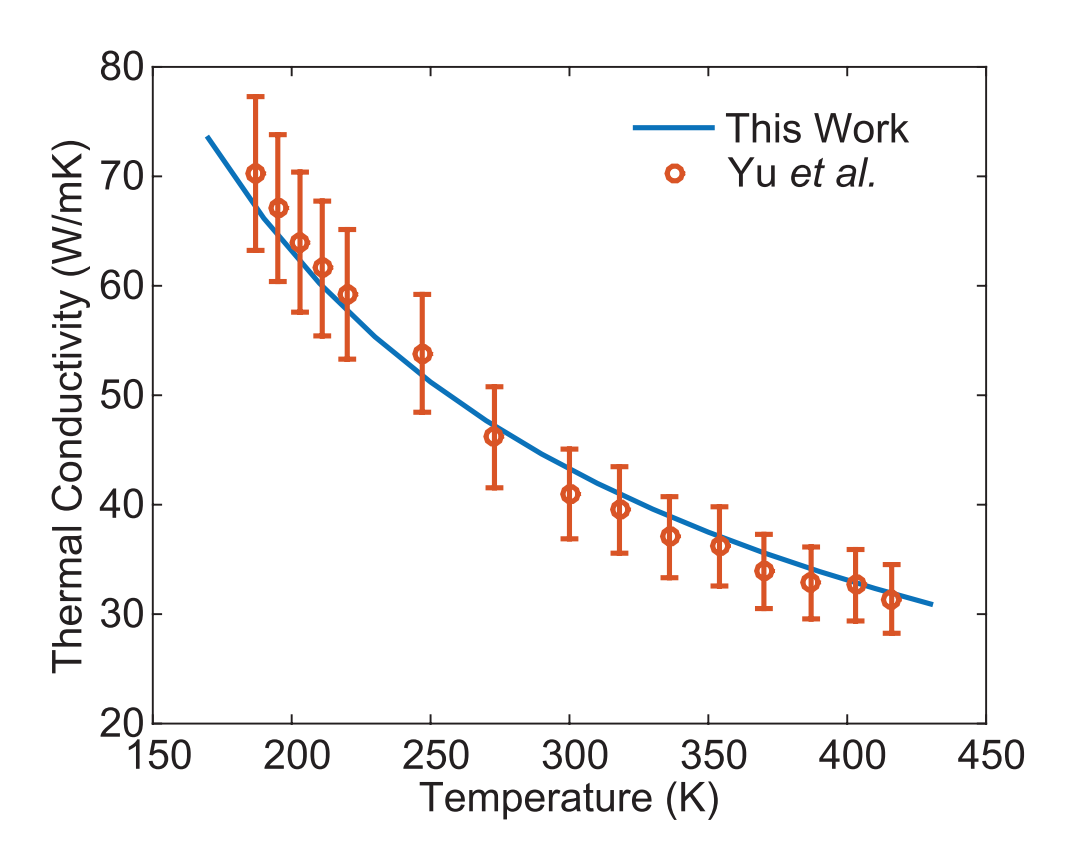


Figure 5.3: In-plane thermal conductivity of a GaAs/AlAs superlattice (layer thickness 70 nm) as a function of temperature. Red symbols show the experimental results of Yu et al.[24] and the blue curve shows the calculations from our model with $\Delta = 3.7$ Å.

experimental data is not monotonic, which indicates that issues with the measurement might explain the discrepancy between our theory and experiment.

Figure 5.3 shows the in-plane thermal conductivity of a GaAs/AlAs SL with a layer thickness of 70 nm at various temperatures. The symbols are the experimental results reported by Yu *et al.*[24] and the line is our calculation with $\Delta = 3.7$ Å. The calculation agrees well with experiment over a wide temperature range.

Figure 5.4 shows the cross-plane thermal conductivity of GaAs/AlAs SLs with various layer thicknesses and from 100 K to 400 K. Symbols show the experimental results reported by Capinski and Maris[26] and Capinski et al.[25] The corresponding curves are obtained from our model. We first set the layer thicknesses to those reported in experiments and then slightly adjust the effective roughness to get the best fit. The roughness chosen for the 40×40 , 25×25 , 10×10 , and 12×14 SLs [× is the notation in these two experimental papers] are 1.75 Å, 1.65 Å, 1.3 Å, and 1.8 Å, respectively. The thermal conductivity varies very little as the temperature changes, and the value is much smaller than that of the in-plane thermal conductivity, both indicating that the TBR indeed dominates thermal transport across the plane.

Luckyanova et al.[1] recently measured both the in-plane and the cross-plane thermal conductivity of a GaAs/AlAs SL. Our calculation for the same structure and the experimental results are shown in Table 5.1. All the calculation results used an effective interface rms roughness of 1.1 Å for the 2-nm system and 1.9 Å for the 8-nm one, which results in good agreement for the cross-plane conductivity; however, the measured in-plane thermal conductivity is considerably lower than the calculation. In fact, the experimental data from Luckyanova et al.[1] shows a great discrepancy with all the previous experiments on similar systems.[23, 24, 26, 25] For example, the in-plane thermal conductivity of their 8-nm SL is considerably smaller than that of the 5-nm SL in Yao's paper,[23] which is counterintuitive and does not agree with well-established trends of increasing thermal conductivity with increasing layer thickness. Furthermore, the cross-plane thermal conductivity (8.7 \pm 0.4 W/mK) is considerably smaller than that of Capinski et al. (10.52 W/mK) with similar

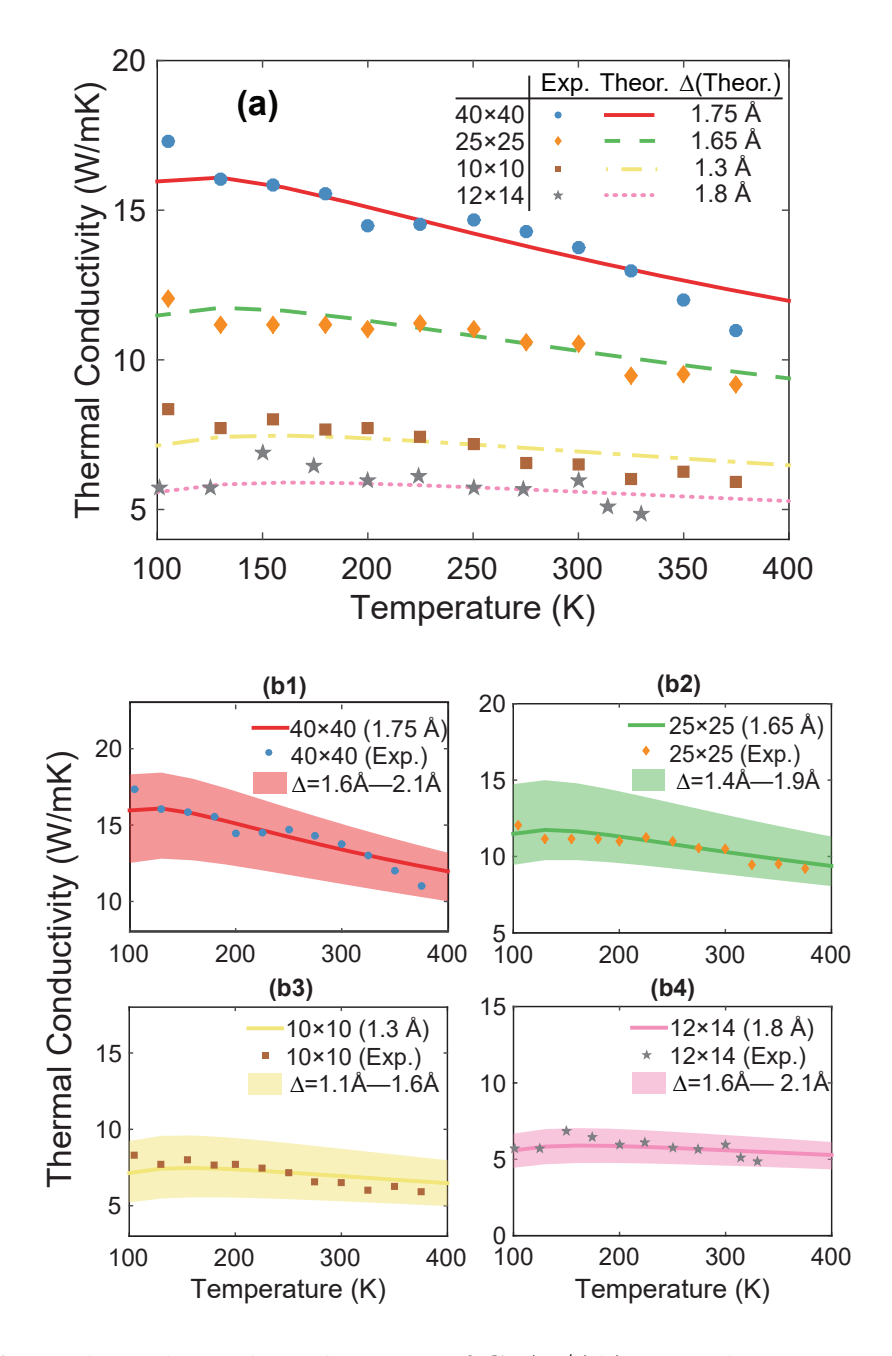


Figure 5.4: Cross-plane thermal conductivity of GaAs/AlAs superlattices as a function of temperature. Blue circles, orange diamonds, and brown squares show the measured cross-plane thermal conductivity data for 40×40 , 25×25 , and 10×10 SLs from Capinski *et al.*[25] Grey stars are the cross-plane thermal conductivity data for for a 12×14 SL from Capinski and Maris.[26] The corresponding curves are calculated based on our model, with the effective rms roughness Δ denoted in the legend.

layer thickness	2 nm		8 nm	
	exp	cal	exp	cal
$\kappa_{ m in-plane}$	8.05 ± 0.48	25.03	11.4 ± 0.46	22.78
$\kappa_{ m cross-plane}$	6.5 ± 0.5	6.38	8.7 ± 0.4	8.59

Table 5.1: Comparison of experimental results from Luckyanova *et al.*[1] and our calculated data for GaAs/AlAs SLs with layer thickness of 2 nm and 8 nm. In the calculation, we assume an interface rms roughness of 1.1 Å for the 2-nm system and 1.9 Å for the 8-nm one.

layer thickness. The earlier experiments [23, 25] should have worse or at best equivalent interface quality to the samples in the most recent work, [1] owing to the development in growth techniques that happened over the past few decades; yet, older samples show higher conductivities. Luckyanova *et al.*[1] also performed density functional perturbation theory (DFPT) simulation, the results of which are about twice what they measured.

5.4.2 InGaAs/InAlAs Superlattices

Sood et al.[27] studied the RT cross-plane thermal conductivity of lattice-matched In-GaAs/InAlAs SLs (In_{0.53}Ga_{0.47}As/In_{0.52}Al_{0.48}As) with varying layer thicknesses. They used the notation AmGn to represent a SL structure with the InAlAs and InGaAs layer thicknesses of n and m nanometers, respectively. Six different SL structures (A2G2, A2G4, A2G6, A4G2, A4G4, A6G2) were measured and these experimental results are reproduced as blue diamonds in Figure 5.5.

We show our calculation results in Figure 5.5. The green circles are the results from our bulk rates as described in Sec. 4.3.3. The calculation assumes very small roughness $\Delta = 0.5$ Å, in keeping with the X-ray diffraction measurements that show nearly perfect interface quality. We note that the green data points are higher than the measurement, but that the trend with the period length is the same as in experiment. Indeed, increasing the interface roughness would significantly and adversely affect the slope of the thermal

conductivity with increasing period length. Therefore, we believe that the reason for the discrepancy is the incomplete knowledge of internal (bulk) scattering in InAlAs, exacerbated by the lack of direct experimental measurements.

Namely, from their data, Sood et al. [27] extract the bulk thermal conductivities of InGaAs and InAlAs to be 5 W/mK and 1 W/mK, respectively. While our calculated bulk thermal conductivity of InGaAs matches experiment, we calculate the bulk conductivity of InAlAs to be of 3.1 W/mK, considerably higher than what Sood et al. reported. Unfortunately, there is no direct experimental data on the thermal conductivity of InAlAs, making it hard to tell what could be the reason of the difference between our calculation and their extracted result.

In red squares, we artificially increase the internal scattering rate of InAlAs so that its bulk thermal conductivity is around 1 W/mK, in keeping with Sood et~al.[27], and we keep the interface scattering rate as before, corresponding to very small $\Delta=0.5$ Å for good-quality interfaces. We see that the red squares agree very well with experimental data, both quantitatively and in the trend with with increasing period length. Considering that the normally calculated thermal conductivity for InAs and AlAs agree with experiment, we believe there is likely some nontrivial aspect of alloy scattering in InAlAs that the model in Ch. 4 does not fully capture and that leads to apparently much lower bulk alloy conductivity of InAlAs than anticipated. Experimental measurement on InAlAs with different In compositions and at differnt temperatures would help shed light on the issue.

5.5 Conclusion to Chapter 5

Based upon the bulk thermal conductivity model presented in Chapter 4, we analyzed thermal transport in III-As SL structures. The calculation of the thermal conductivity tensor in superlattices involves each layers conductivity, itself affected by the impact of diffuse interface scattering on phonon populations, as well as explicit thermal boundary resistance that only affects the cross-plane thermal transport. We calculate the TBR between interfaces based on interpolating the transmission coefficient between the AMM and the

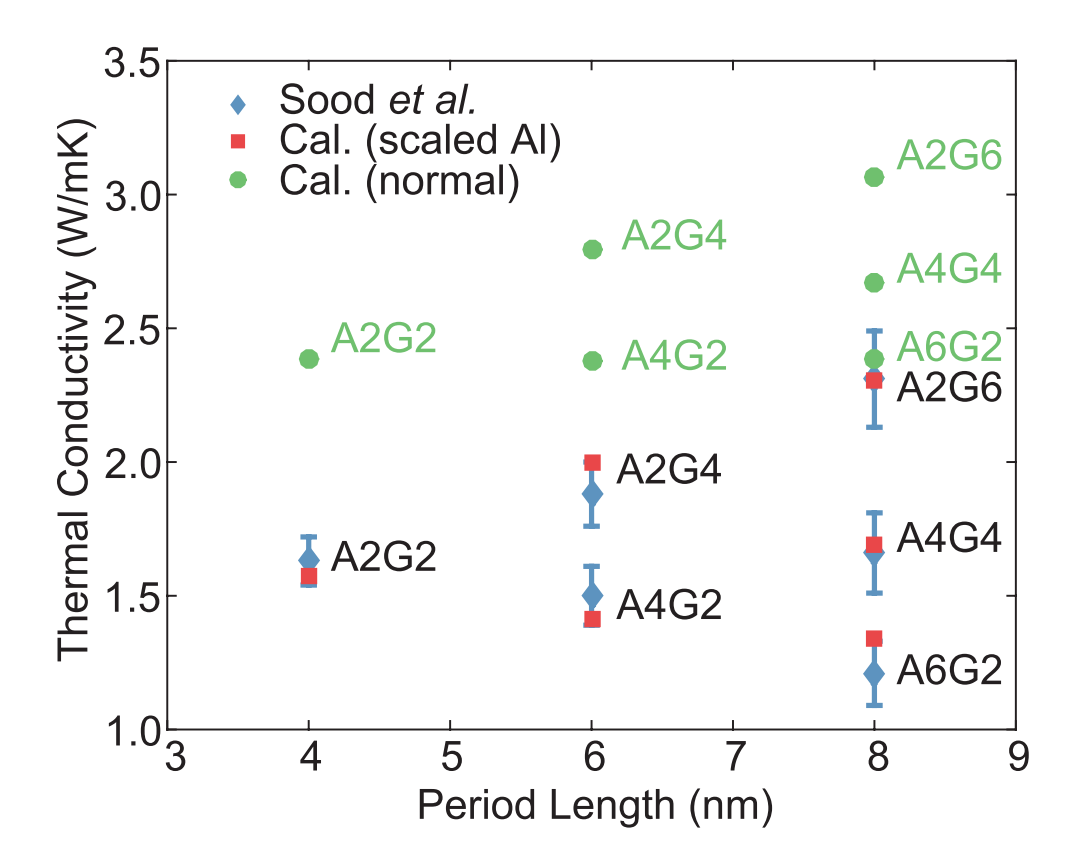


Figure 5.5: Cross-plane thermal conductivity of $In_{0.53}Ga_{0.47}As/In_{0.52}Al_{0.48}As$ SLs as a function of the period length. The notation AmGn represents a SL structure with the InAlAs and InGaAs layer thicknesses of m and n nanometers, respectively. Blue diamonds show the experimental data from Sood *et al.*[27], green dots show our calculation with regular scattering rates, and red squares show the calculation results with artificially increased bulk rates for InAlAs. In both calculations, Δ is chosen to be 0.5 Å, in keeping with the perfect interface quality revealed in X-ray diffraction experiments.

DMM, where the specularity parameter (traditionally used to describe diffuse scattering) is also used as the AMM weight in the interpolation. Therefore, with a single free parameter—the effective interface rms roughness Δ (often ranging from 0.5 Åto 6 Åfor high-quality III-As interfaces)—we captured the transport properties of multiple GaAs/AlAs and InGaAs/InAlAs SL structures over a wide temperature range (70 K to 400 K). The observed discrepancy between the calculated and experimentally extracted layer thermal conductivity of InAlAs indicates that the VCA being questionable for this material. This topic is further explored in Chapter 6.

The presented model is fairly simple yet quite accurate, especially when used with full phonon dispersions. It can be very useful for thermal modeling complicated QCL structures, with many interfaces. The model is also applicable to other material systems where SLs have good-quality interfaces and phonon transport can be considered incoherent.

Chapter 6

Thermal Conductivity of III-V Bulk Materials: EMD

As discussed in chapter. 4 and 5, adopting the virtual crystal approximation [21] (VCA) to compute the thermal conductivity (TC) of ternary III-As alloys works well for $Al_xGa_{1-x}As$ and $In_xGa_{1-x}As$ with various x compositions. [4, 22, 16] For $In_xAl_{1-x}As$, however, experimental TC value is only available for $In_{0.52}Al_{0.48}As$ and don't agree with each other. [5, 27] Our calculated TC is 2.82 W/m·K, which is close to the Koh $et\ al$. [5] result but very far from the Sood $et\ al$. [27] value. Since we have benchmarked the technique for binaries, we speculate it is the VCA that is not entirely suitable for characterizing the TC of ternary III-As alloys.

Within the VCA, there are two major assumptions whose validity needs to be questioned when it comes to the calculation of TC in ternary alloys $A_xB_{1-x}C$. (1) All cations can effectively be replaced with an effective averaged cation, whose mass is calculated as the weighted average of cation masses, i.e., $(m_{III} = xm_A + (1-x)m_B)$. (2) The alloy is random, i.e., cation sites are randomly taken by atom A or atom B, with the frequency proportional to cation abundance (x and (1-x), respectively). Although an effective mass-difference scattering rate is added to compensate for the fact that assumption (1) eliminates scattering caused by cation mass-difference,[21] this approach is inherently perturbative and assumes that the cation mass difference is small with respect to the average cation mass. Therefore, the validity of this perturbative mass-difference-scattering approach becomes suspect when the cation masses are different. In our case, $m_{Al} = 26.98$ au, $m_{Ga} = 69.72$ au, and $m_{In} = 114.82$, so it makes sense that the model works better for $In_xGa_{1-x}As$ and $Al_xGa_{1-x}As$ than it does

for $In_xAl_{1-x}As$, since the mass difference between Al atoms and In atoms is significant. The second assumption is directly contradicted by a number of X-ray and transmission electron microscopy (TEM) experiments conducted on ternary III-V alloys grown epitaxially on GaAs or InP substrate.[151, 152, 153, 154, 155, 156, 157, 158, 159, 160, 161, 162] These experiments show that group III atoms in ternary III-As epi-layers are arranged with certain order rather than completely randomly. This ordered structure is also backed up by observable change in the width of electronic bandgap of these materials. The most observed types of ordering for $In_{0.53}Ga_{0.47}As$ and $In_{0.52}Al_{0.48}As$ are the CuPt-B order[151, 152, 153, 155] and the triple-period-A (TPA) order.[154, 156, 157, 158, 159, 160] The CuAu-I order is more common in $Al_{0.5}Ga_{0.5}As[161, 162]$ but could also be observed in $In_{0.53}Ga_{0.47}As$ or $In_{0.52}Al_{0.48}As$ under appropriate growth conditions.[157, 162]

To directly address these two questionable assumptions, we use molecular dynamics (MD) to study the thermal transport inside ternary III-As alloys. In a MD simulation, the mass and location of each atom are tracked in real space; therefore it is straightforward to include individual mass and the exact alloy structure explicitly in the simulation. We adopt the Tersoff[163, 164] empirical interatomic potentials (EIPs) to describe the interaction between atoms. The parameters we used in the EIPs had been obtained by an optimization technique, starting from the existing ones,[2, 165, 3] with the goal to better capture the phonon properties of binary III-As semiconductors.[166] We then used the optimized EIPs to study the influence of mass difference and ordering on the TC of ternary III-As alloys.

6.1 Thermal Conductivity from Equilibrium Molecular Dynamics

All the MD simulations in this work are carried out in the LAMMPS[167] package. We use equilibrium molecular dynamics (EMD) together with the Green-Kubo (GK) formula (discussed in chapter. 2) to compute the TC of the compound semiconductors.

For cubic bulk semiconductors, the TC is expected to be isotropic. As a result, we used cubic simulation cells with periodic boundary conditions applied in all directions. In a

typical simulation, the system was first initialized at the desired temperature T by assigning each atom a random velocity that follows the thermal distribution at T. Then the system was equilibrated as an NPT ensemble (constant number of atoms, constant pressure as 1 atm, and constant temperature T, as specified) using the Nosé-Hoover barostats and thermostats [168, 169] for 100 ps. After that, the system was further equilibrated as an NVE ensemble (constant number of atoms, constant volume, and constant system energy) for another 100 ps before the heat flux is collected. The instantaneous heat flux is then calculated and output into a file at every time step, for 5 million steps. A script was written to post-process the output file to obtain the heat current autocorrelation function and its running integral. We made sure the integral saturated and extracted the bulk TC according to Eq. (2.8). The time step was chosen to be small enough so the system stays stable throughout the simulation-here, the time step was 1 fs for binary materials and 0.1 fs for ternary alloys. For each simulation (given material and temperature), several random starting velocity distributions were used and the final result was averaged among the different runs. We tested the simulation domain sizes to make sure there is no size effect. The final results for binary III-As were obtained with a simulation cell $10a_0 \times 10a_0 \times 10a_0$ in size, where a_0 is the lattice constant for the material. For ternary alloys, $8a_0 \times 8a_0 \times 8a_0$ was enough for the TC to converge. We used $9a_0 \times 9a_0 \times 9a_0$ cells for alloys with TPA ordering as the algorithm for generating cells requires the system size to be multiples of 3 (more details in Sec. 6.4).

6.1.1 Quantum-Correction of Temperature

In MD simulations, system temperatures are calculated following the rules of classical statistical mechanics. [170] We adopt a simple quantum-correction procedure for the temperatures by mapping the kinetic energy of an MD system at temperature $T_{\rm MD}$ onto that of a quantum system with temperature $T_{\rm Q}$ [170, 171]

$$\frac{3}{2}Nk_{\rm B}T_{\rm MD} = \sum_{\rm b} \sum_{\mathbf{k}} \hbar\omega(\mathbf{k}, \mathbf{b}) \left\{ \frac{1}{2} + \frac{1}{\exp\left[\frac{\hbar\omega(\mathbf{k}, \mathbf{b})}{k_{\rm B}T_{\rm Q}}\right] + 1} \right\}.$$
 (6.1)

In the left-hand side, N is the number of atoms in the system and $k_{\rm B}$ is the Boltzmann constant. In the right-hand side, the summation is over all the phonon branches b and wave vectors \mathbf{k} . $\hbar\omega(\mathbf{k},\mathbf{b})$ is the corresponding phonon energy. The additional $\frac{1}{2}$ in the curly bracket accounts for the non-zero ground energy in a quantum system. For the right-hand side, we used an approximate isotropic phonon dispersion fitted from the full phonon dispersion, based on our previous work.[38] Figure 6.1 shows the mapping between the quantum-corrected temperature and the MD temperature for GaAs (the curve is similar for AlAs and InAs) between 0 K and 500 K. We see that $T_{\rm MD}$ and $T_{\rm Q}$ coincide at higher temperatures but differ a great deal at lower temperatures. At room temperature, there is typically a 4%-8% difference between $T_{\rm MD}$ and $T_{\rm Q}$ for III-As. Henceforth, all the temperatures listed in this work are the quantum-corrected temperatures $T_{\rm Q}$.

6.2 Optimizing the Tersoff Potentials

6.2.1 Tersoff Potentials

The Tersoff EIP was proposed in by Tersoff in 1988 for silicon, [163] extended to SiC in 1989, [164] and later successfully parameterized for most III-V binary compounds. [2, 172, 165, 3] Tersoff potentials have a cutoff distance that limits the atom interactions to only between the nearest neighbors, which is an advantage in our case: the nearest-neighbor interaction makes it easy to apply the potentials for binary III-As to ternary III-As alloys.

In the LAMMPS package, the Tersoff potential is described using 14 parameters in the following form. The total energy of the system is the summation of energy between each pair:

$$E = \frac{1}{2} \sum_{i} \sum_{j \neq i} V_{ij}. \tag{6.2}$$

The pair interaction potential V_{ij} between atom i and atom j is described by the competition between a repulsive term f_R and an attractive term f_A , and is modulated by a cutoff term f_C so that only nearest-neighbor interactions are included:

$$V_{ij} = f_C(r_{ij}) \left[f_R(r_{ij}) + b_{ij} f_A(r_{ij}) \right]. \tag{6.3a}$$

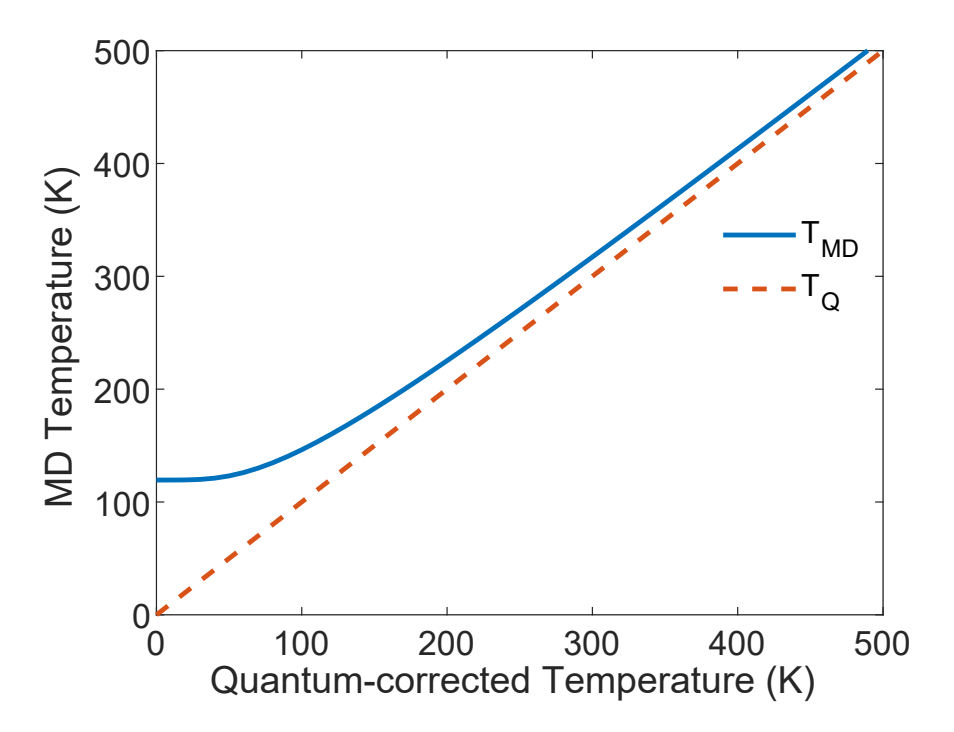


Figure 6.1: A typical mapping between the MD calculated temperature $T_{\rm MD}$ and the quantum-corrected temperature $T_{\rm Q}$ (figure showing the case of GaAs). The two values converge at high temperatures and differ a great deal at low temperatures.

The cutoff function writes as

$$f_C(r) = \begin{cases} 1 & : r < R - D, \\ \frac{1}{2} - \frac{1}{2}\sin\left(\frac{\pi}{2}\frac{r - R}{D}\right) & : R - D < r < R + D, \\ 0 & : r > R + D, \end{cases}$$
(6.3b)

where r is the variable. From Eq. (6.3b), the cutoff length is R + D and there is a transition window with width 2D. Both R and D are parameters of the Tersoff potential. Both the repulsive and the attractive terms have an exponential form with A, B, λ_1 and λ_2 being potential parameters:

$$f_R(r) = A \exp(-\lambda_1 r), \tag{6.3c}$$

$$f_A(r) = -B \exp(-\lambda_2 r). \tag{6.3d}$$

To include the influence of the bond angle and length, the attraction term f_A is further modified by the bond angle term b_{ij} where

$$b_{ij} = (1 + \gamma^n \xi_{ij}^n)^{-\frac{1}{2n}}, \tag{6.3e}$$

and

$$\xi_{ij} = \sum_{k \neq i,j} f_C(r_{ik}) g(\theta_{ijk}) \exp\left[\lambda_3^m (r_{ij} - r_{ik})^m\right],$$
 (6.3f)

$$g(\theta) = \delta_{ijk} \left(1 + \frac{c^2}{d^2} - \frac{c^2}{d^2 + (\cos \theta - \cos \theta_0)^2} \right).$$
 (6.3g)

The summation in ξ_{ij} goes over all the central atom i's neighbors within the cutoff except for the neighbor j whose interaction with i we are considering. The bond angle θ_{ijk} can be calculated with the three atoms' coordinates and δ_{ijk} is a scaling parameter that is unity in most cases. γ , n, λ_3 , and m are potential parameters. In particular, m can only take the value of 1 or 3. c, d, and $\cos \theta_0$ are bond-angle-related potential parameters. Note that $\cos \theta_0$ is often denoted as h; the form of a cosine simply reminds us this parameter can only take values between -1 and 1.

A variation of the original Tersoff potential is the Albe-Tersoff potential where the strength and the decaying speed in Eq. (6.3c) and (6.3d) are expressed with parameters

 D_e , S, β , and r_e in place of A, B, λ_1 , and λ_2 .[173] The relationship between the two sets of parameters can be derived as

$$A = \frac{D_e}{S - 1} \exp(\beta \sqrt{2Sr_e}), \tag{6.4a}$$

$$B = \frac{SD_e}{S - 1} \exp(\beta \sqrt{2S/r_e}), \tag{6.4b}$$

$$\lambda_1 = \beta \sqrt{2Sr_e},\tag{6.4c}$$

$$\lambda_2 = \beta \sqrt{2S/r_e},\tag{6.4d}$$

In the case of Albe-Tersoff potential, we work with the parameters D_e , S, β , and r_e and then use a script to convert them to A, B, λ_1 , and λ_2 for the input potential file of LAMMPS.

6.2.2 Phonon Dispersion from EIP

With a given EIP, the phonon frequencies $\hbar(\mathbf{k}, \mathbf{b})$ for wave vector \mathbf{k} and branch \mathbf{b} can be obtained by diagonalizing the dynamical matrix[174]

$$\mathcal{D}_{\alpha\beta}(ij|\mathbf{k}) = \frac{1}{\sqrt{m_i m_j}} \sum_{l'} \phi_{\alpha\beta}(0i; l'j) e^{i\mathbf{k}\mathbf{x}(l')}, \tag{6.5}$$

where l'j represents atom j in the l'th unit cell and the summation is over all the relevant neighbors of the central atom i. $\mathbf{x}(l')$ is the relative location of unit cell l' with respect to the unit cell i is in. The interatomic force constants (IFCs) between atom i and j ($\phi_{\alpha\beta}(0i; l'j)$) are calculated using the central finite difference method:

$$\phi_{\alpha\beta}^{ij} = \frac{\partial V_{ij}^2}{\partial \alpha \partial \beta} = \frac{V(\mathbf{r}_{ij} + d_{\alpha} + d_{\beta}) - V(\mathbf{r}_{ij} - d_{\alpha} + d_{\beta}) - V(\mathbf{r}_{ij} + d_{\alpha} - d_{\beta}) + V(\mathbf{r}_{ij} - d_{\alpha} - d_{\beta})}{4d_{\alpha}d_{\beta}}.$$
(6.6)

Phonon dispersion curves are obtained by computing the phonon frequencies for multiple \mathbf{k} s along a certain direction in the first Brillouin zone (1BZ). The sound velocities are obtained from the acoustic branches near the zone center (Γ point) as

$$|\mathbf{v}_{s,b}| = |\nabla_{\mathbf{k}}\omega(\mathbf{k},b)|,$$
 (6.7)

where the subscript b is the branch index. Since the phonon dispersion is isotropic near the Γ point, we use the dispersion curves along the [100] ($\Gamma - X$) direction to calculate the sound velocities. The two transverse acoustic (TA) branches are degenerate along the $\Gamma - X$ direction and we only need one scaler velocity for the TA branches $(v_{s,TA})$ and one for the longitudinal acoustic (LA) branch $(v_{s,LA})$.

6.2.3 Parameter Optimization

Most Tersoff potentials are parameterized so as to accurately capture the mechanical properties of the materials.[163, 164, 2, 172, 165, 3] However, for the EIPs to be good at describing thermal transport, they must also produce good phonon properties. Lindsay and Broido[166] optimized the Tersoff potential of carbon (C) for thermal transport. They use a χ^2 minimization procedure

$$\chi^2 = \sum_{i} \frac{(\eta_i - \eta_{\exp,i})^2}{\eta_{\exp,i}^2} \zeta_i, \tag{6.8}$$

where i runs over all the physical properties they optimize for. η_i and $\eta_{\exp,i}$ are, respectively, the calculated and experimental values for physical property i. ζ_i is the weighting factor determining the relative importance of each physical property in the optimization process. They assigned the most weight to the phonon frequencies and zone-center acoustic velocities (also known as the sound velocities), because of their crucial rule in thermal transport.[166]

Here we follow a similar minimization approach to improve the EIPs' performances for describing the thermal transport. The physical properties we optimized for are the lattice constant a_0 , the cohesive energy $E_{\rm coh}$, and the sound velocities $v_{s,\rm TA}$ and $v_{s,\rm LA}$. Note that the agreement of the phonon dispersion only guarantees the accuracy of the second derivatives of the EIPs (or the IFCs) (Sec. 6.2.2) while the finite TC of crystals originates from the phonon-phonon scattering, related to the third and higher derivatives of the EIPs. Since the strength of these higher-order interactions are not easily accessible through experiments, we used the temperature-dependent TC measured in experiments as an additional gauge, because the temperature variation of TC is dictated by phonon-phonon interactions. First, we optimize the EIPs to match the phonon dispersion following Lindsay and Broido.[166] Then we used the optimized potential to calculate the temperature-dependent TC following the procedure described in Sec. 2.3. We were most interested in the temperature range between 100 K and

500 K because most devices operate in this range. A comparison between the calculated and measured TC instructed us to further adjust the weights in the optimization process. This process was repeated until we obtained a satisfactory temperature-dependent TC from the potentials.

For simplicity, we use existing parameterizations as starting points. To choose the best starting point, we calculate the temperature-dependent TC with existing potentials. For the three binary III-As materials—AlAs, GaAs, and InAs—we are most interested in, the potentials that yield temperature-dependent TC closest to experimental values are from Sayed et~al.[2], Powell et~al.[165], and Hammerschmidt et~al.[3], respectively. Incidentally, all these three are parameterized in the Albe-Tersoff form. Like Lindsay and Broido,[166] we try to adjust only a few parameters among all. R and D are always left untouched because they dictate the cutoff of the EIPs. m also stays constant per LAMMPS's requirement. In the remaining parameters, we find that D_e , β , c, d, and h are very effective in adjusting the four physical properties we want to optimize. Therefore, during the χ^2 minimization, we only vary these five parameters.

6.2.4 Optimized Potentials

In the optimization, we found that the parameters for GaAs from Powell et al.[165] yielded very good sound velocities as well as temperature-dependent TC from 100 K to 500 K. Therefore we adopted this set of parameters as it was. However, the parameters for AlAs[2] and InAs[3] both had to be optimized. Table 6.1 shows the optimized parameters for AlAs and InAs. As mentioned in Sec. 6.2.3, the parameters other than the five listed were kept the same as in the original sets.

The three panels in Fig. 6.2 are show the calculated temperature-dependent TC (dark green dots with error bars) in comparison with experimental data[13, 15, 12, 18, 19, 20] (light green solid lines) for AlAs, GaAs, and InAs, respectively. The insets show the calculated phonon dispersion along the Γ – X direction (dashed lines) in comparison with measured values[11, 28, 29, 30] (dots).

AlAs	InAs
$D_e = 2.6372$	$D_e = 1.9949$
$\beta = 1.6948$	$\beta = 1.7660$
c = 1.4145	c = 4.0249
d = 0.9116	d = 1.0157
h = -0.6172	h = -0.6096

Table 6.1: Optimized parameters for the Albe-Tersoff potentials for AlAs and InAs. Parameters not listed are the same as in the original sets.[2, 3]

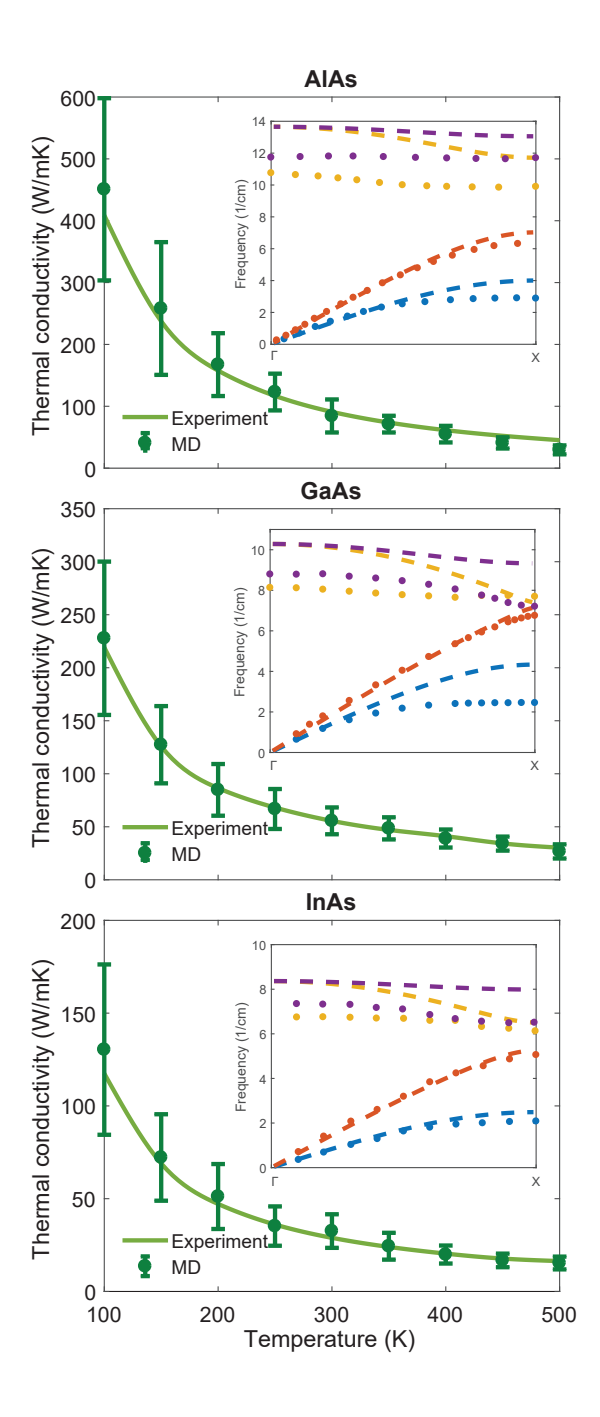


Figure 6.2: Temperature-dependent thermal conductivity, as calculated in this work with optimized potentials (dark green dots with error bars) and from experiments (light green solid lines) for AlAs,[12] GaAs,[13, 15] and InAs.[18, 19, 20] The insets show the calculated phonon dispersions (dashed lines) along the Γ – X direction along with experimental values (dots).[11, 28, 29, 30]

6.3 Thermal Conductivity of Ternary Alloy: The Role of Cation Mass Difference

After obtaining the optimized EIPs for binary compounds, we applied these potentials to ternary alloys. We investigated the validity of the first assumption in the VCA (all cation atom are assigned the same, weighted average mass) in predicting the TC. For this part, we kept the second assumption that all ternary alloys were random alloys. We considered $In_xGa_{1-x}As$ and $In_xAl_{1-x}As$ alloys with x varying from 0.1 to 0.9. For each x, we generated 10 different random simulation cells with the corresponding composition. For each random configuration, we conducted 20 simulations with different starting velocity distributions. Each of the final TC value was averaged over the 200 runs.

In order to isolate the effect of the mass difference, we carry out two sets of simulations (at RT). In the first set, all the cation atoms kept their own masses ($m_{Al} = 26.98$ au, $m_{Ga} = 69.72$ au, and $m_{In} = 114.82$ au). In the second set, the cations were all assigned the same weighted-average mass [$m_{avg} = x m_{In} + (1 - x) m_{Ga/Al}$]. Other than this difference, the two sets used the same EIPs and random (not ordered) configurations in the simulation. Figure 6.3 shows the TC data for both $In_xGa_{1-x}As$ and $In_xAl_{1-x}As$. The results from the explicit-mass (EM) case and the averaged-mass (VCA) case are shown in blue diamonds and red dots, respectively. Existing experimental data is shown in stars, for comparison.[4, 5, 27]

From Fig. 6.3, the EM TC is consistently lower than the VCA TC across the In% for both $In_xGa_{1-x}As$ and $In_xAl_{1-x}As$. Moreover, the difference between the EM and VCA is much more pronounced in $In_xAl_{1-x}As$ (where the mass difference is larger) than in $In_xGa_{1-x}As$ (where the mass difference is smaller). Therefore, it is evident that mass-difference scattering is critical in III-V ternary random alloys. Using an averaged VCA mass for cations will underestimate the mass-difference scattering; the larger the mass difference, the greater the underestimate. Additionally, in the case of $In_xGa_{1-x}As$, both the EM TC and the VCA TC are significantly smaller than the experimental value; in the case of $In_xAl_{1-x}As$, the two

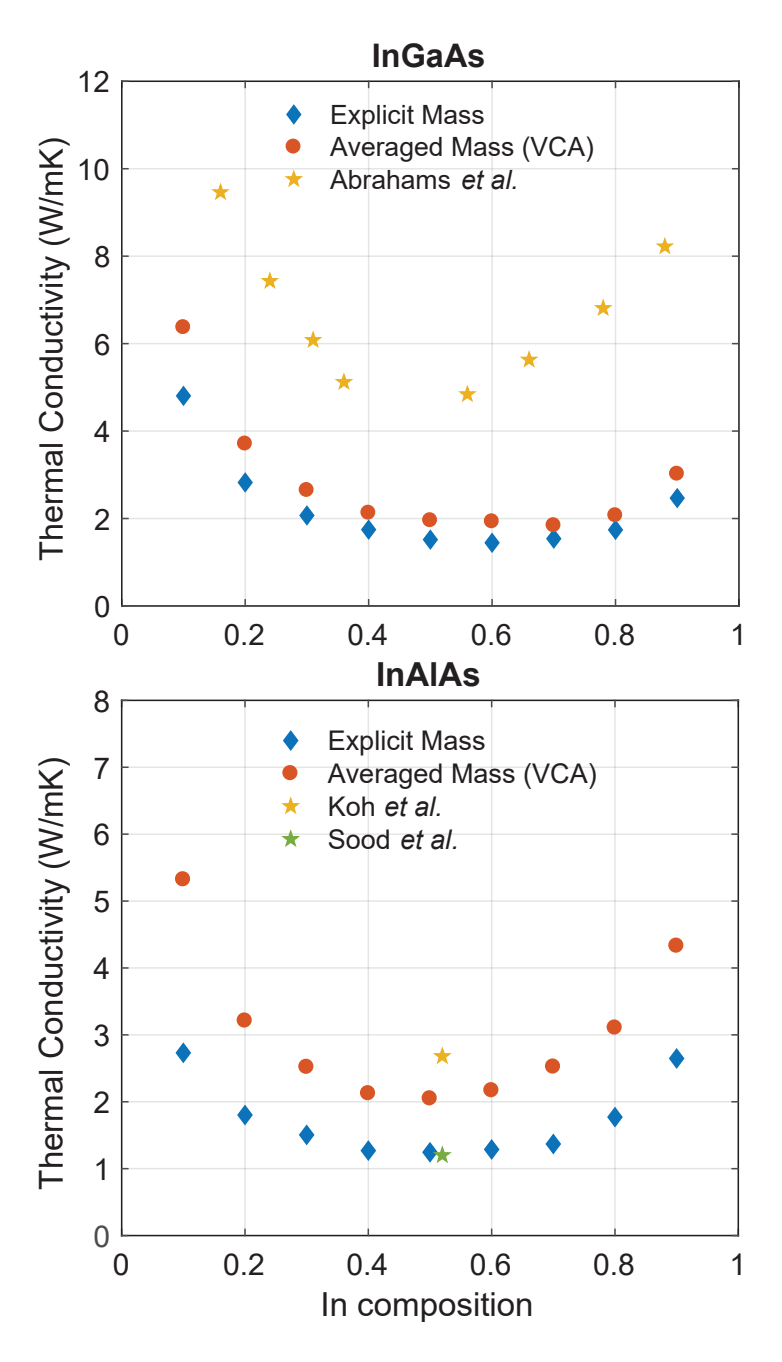


Figure 6.3: Thermal conductivity as a function of In composition in $In_xGa_{1-x}As$ and $In_xAl_{1-x}As$ random alloys at room temperature. In blue diamonds we show the calculated TC for the case where each atom's mass is included explicitly. Results from the case where all cations take the averaged-VCA mass are shown in red dots. Stars are showing experimental measurements.[4, 5, 27]

experimental results are so far apart that the EM TC and VCA TC fall in between the two measurements. As a result, we can conclude that there must be another mechanism that competes with the mass-difference scattering to influence the TC of ternary alloys.

6.4 Thermal Conductivity of Ternary Alloy: The Role of Order

6.4.1 Thermal Conductivity of Alloys Near $A_{0.5}B_{0.5}C$ Composition with CuPt-B and CuAu-I order

Experimentalists who grow and characterize III-V epitaxy layers have long discovered that both long-range and short-range order exists in ternary III-V alloys.[151, 153, 154, 155, 156, 157, 158, 175, 159, 160, 161, 162] Order leads to changes in bond length and electronic band gaps. Since phonons are quanta of lattice vibrations,[140] it is intuitive that thermal transport behavior will also change in the presence of ordering. Duda et al.[176, 177] studied one particular type of order in Si_{0.5}Ge_{0.5} using the non-equilibrium molecular dynamics (NEMD) method and the simple Lennard-Jones potential. Baker and Norris[178] studied both long-range and short-range order in Si_{0.5}Ge_{0.5} with the Stillinger-Weber potential. We were interested in III-V ternary alloys with compositions away from the 50%-50% case. We also want to use EIPs that would give us quantitatively accurate results for TC. It is noteworthy that order in III-V ternary alloy samples is often localized, i.e., it is common to have "poly-ordering" where the sample has one type of order in one region and a different type of order in another.[155, 175, 152]

For the sake of simplicity, in this work we only simulate samples with a single type of order that extends to infinity and we applied periodic boundary conditions. Moreover, we focused on three different types of order that are most commonly observed in III-V ternary alloys: the CuPt-B type, the CuAu-I type, and the triple-period-A (TPA) type.[157] Both CuPt-B and CuAu-I ordering yield alloys with the composition A_{0.5}B_{0.5}C within the Zinc-Blende lattice. Figure 6.4 shows the crystal structure of both the CuPt-B and CuAu-I ordering. In CuPt-B ordering, A atoms and B atoms take alternate cation planes along the [-111]

Material	CuPt-B	CuAu-I	Rand. Alloy	Expt.
$\mathrm{In}_{0.5}\mathrm{Ga}_{0.5}\mathrm{As}$	12.71	14.39	1.52	$4.84 (\mathrm{In}_{0.53} \mathrm{Ga}_{0.47} \mathrm{As})$
$\overline{In_{0.5}Al_{0.5}As}$	6.488	6.472	1.25	$2.68 (\mathrm{In}_{0.52} \mathrm{Al}_{0.48} \mathrm{As})$

Table 6.2: Comparison of calculated RT TC for $In_{0.5}Ga_{0.5}As$ and $In_{0.5}Al_{0.5}As$ with perfectly ordered CuPt-B and CuAu-I structure as well as the random alloy structure and the experimentally measured TC for $In_{0.53}Ga_{0.47}As[4]$ and $In_{0.52}Al_{0.48}As[5]$.

direction. In CuAu-I ordering, A atoms and B atoms take alternate cation planes along the [100] direction. Note that perfectly ordered alloys do not exist in experiments, so the alternating planes are actually A-rich and B-rich planes. TPA ordering in its ideal form refers to the case where the cation planes along [111] direction has a repeated pattern involving 3 planes. Therefore, ternary alloy $A_xB_{1-x}C$ with any composition x can be represented in some TPA ordering where each period has the arrangement of $A_uB_{1-u}/A_vB_{1-v}/A_wB_{1-w}$ and (u+v+w)/3=x (note the three planes in a period cannot be all equal or the triple-period collapses). Figure 6.5 depicts a typical crystal structure of ternary alloy $A_{0.5}B_{0.5}C$ where $u=1,\ v=0,$ and w=0.5.

We calculated the RT TC of perfectly ordered In_{0.5}Ga_{0.5}As and In_{0.5}Al_{0.5}As with both CuPt-B and CuAu-I types of order and show the results in Table 6.2. The calculated TC for In_{0.5}Ga_{0.5}As and In_{0.5}Al_{0.5}As with random alloy structures (with explicit mass) are also shown for comparison. Since there are no experiments on In_{0.5}Ga_{0.5}As and In_{0.5}Al_{0.5}As, we compared the results with experiments on In_{0.53}Ga_{0.47}As[4] and In_{0.52}Al_{0.48}As[5]. From Table 6.2, we conclude that order of either type significantly increases the TC of both In_{0.5}Ga_{0.5}As and In_{0.5}Al_{0.5}As alloys compared to the random alloy case. The CuAu-I type ordering leads to slightly higher TC than the CuPt-B type order in both alloys. All the simulated TC values from the perfectly ordered structures were higher than the experimental measurement, which is intuitive because In_{0.53}Ga_{0.47}As and In_{0.52}Al_{0.48}As in experiments are 1) not perfectly ordered and 2) have In compositions away from 0.5.

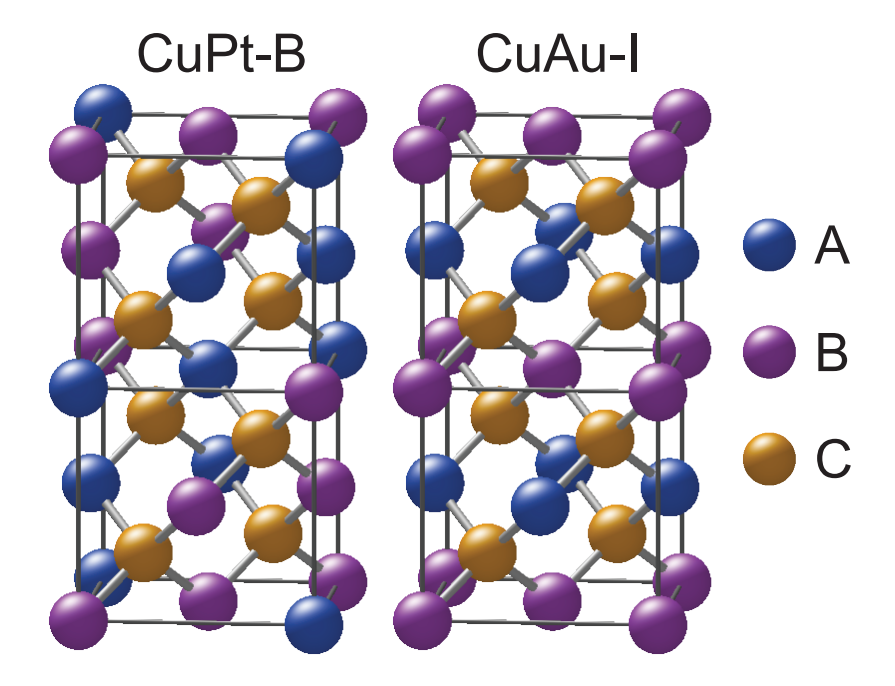


Figure 6.4: The crystal structure of ordered ternary alloy $A_{0.5}B_{0.5}C$ with CuPt-B and CuAu-I ordering.

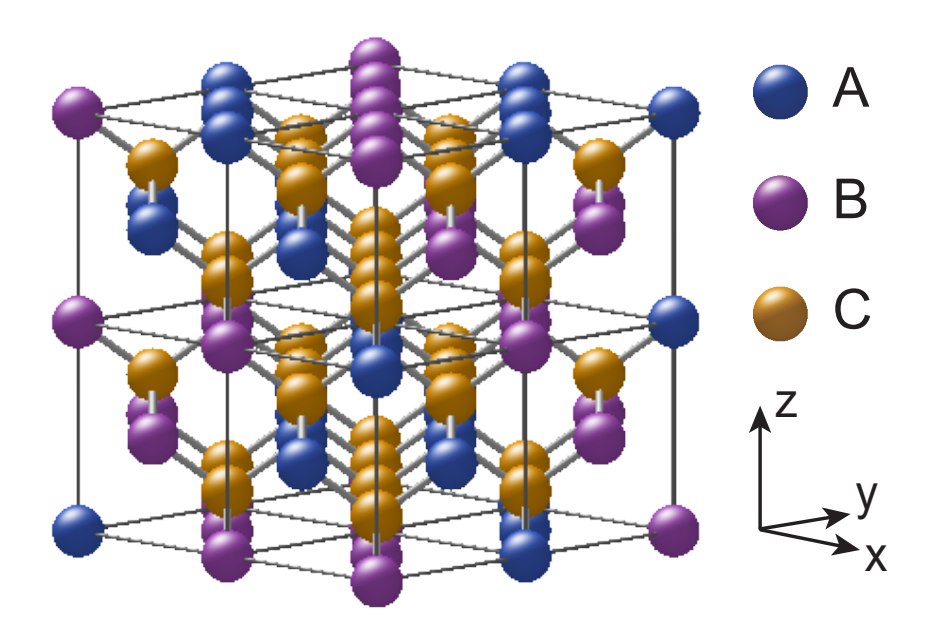


Figure 6.5: A sample crystal structure of ordered ternary alloy $A_{0.5}B_{0.5}C$ with TPA ordering. The 3 planes in a period $(A_uB_{1-u}/A_vB_{1-v}/A_wB_{1-w})$ has configurations of $u=1,\ v=0,$ and w=0.5.

	CuPt-B		CuAu-I				
Material	LM	LM+4%	LM+8%	LM	LM+4%	LM+8%	Expt.
$In_{0.53}Ga_{0.47}As$	5.022	3.165	2.585	5.728	3.567	2.845	4.84
$\overline{\text{In}_{0.52}\text{Al}_{0.48}\text{As}}$	3.965	3.216	2.654	4.426	3.248	2.805	2.68

Table 6.3: Calculated RT TC for lattice-matched (LM) $In_{0.53}Ga_{0.47}As$ and $In_{0.52}Al_{0.48}As$ with various percentage of additional random disorder. Experimentally measured TC are also listed for comparison.[4, 5]

To directly compare the simulated TC with the experimentally measured TC for $In_{0.53}Ga_{0.47}As$ and In_{0.52}Al_{0.48}As lattice matched to InP, we randomly replace 3% (2%) of Ga (Al) atoms in the perfectly ordered structure with In atoms to obtain lattice-matched simulation cells. Table 6.3 shows the TC of lattice-matched In_{0.53}Ga_{0.47}As and In_{0.52}Al_{0.48}As from both our simulations and the experiments. We see that TC obtained directly from the lattice-matched simulation cells are still quite large compared to the experiments, which could be attributed to the existence of additional disorder that is inevitable in real experimental samples. Here we investigate one type of disorder: randomness. We take the lattice-matched simulation cells and randomly swap an In atom with a Ga (Al) atom to create disorder. The amount of disorder is categorized by the percentage of swapped In atoms in the cell. In Table 6.3, the cells with the simulation results are labeled with LM+d%, where LM stands for lattice matched and d% is the level of disorder. Consistent with the findings in Sec. 6.3, even little disorder (< 10%) severely reduces the alloy TC. Comparing the calculation with experiments, the level of disorder in $In_{0.53}Ga_{0.47}As$ is around 2% while in $In_{0.52}Al_{0.48}As$ it is approximately 8%. Also, as expected, the calculated lattice-matched TC for InGaAs and InAlAs is lower than the corresponding TC calculated from the perfectly ordered structures.

6.4.2 Thermal Conductivity of Alloys with Dierent Compositions and TPA Order

To study the TC of ordered $In_xGa_{1-x}As$ and $In_xAl_{1-x}As$ with various x (away from 0.5), we needed to implement TPA order. While it was impossible to consider every feasible arrangement of the TPA order, we simulated the two extreme cases that would likely yield the upper and lower limits of the TC with TPA order for each x. The idea is that with more symmetry comes less phonon scattering, and the resulting TC should be higher. Note here we only focus on the perfectly ordered structures, therefore x values were limited to multiples of $\frac{1}{12}$. For each x, we generate two TPA cells: most symmetric (MS) and least symmetric (LS). Figure 6.6 shows the TC calculated from the MS cells (red squres), LS cells (yellow dots), and measured in experiments [4, 5] (blue diamonds), respectively. The results are consistent with our expectations. The MS TC is higher than the LS TC while both are higher than the experimental data (simulated structures are perfectly ordered, while experimental samples contain disorder). TC values of MS and LS fall on top of each other when $x = \frac{1}{12}$ and $x = \frac{11}{12}$ because the MS and LS structures are equivalent in these cases. Calculated TC follows the general U-shape (TC is lowest when x is close to 0.5 and increases as x approaches 0 and 1), except for a sudden TC jump at certain x values $(x = \frac{n}{12}, n = 2, 4, 6, 8, \text{ and } 10)$. The jumps exist because these fractions $\frac{n}{12}$ are reducible, which leads to additional symmetry in the system.

6.5 Conclusion to Chapter 6

In this chapter, we studied the thermal conductivity of III-V ternary alloys, $In_xGa_{1-x}As$ and $In_xAl_{1-x}As$ in particular. We investigated how the mass difference between cation atoms and the arrangement of cation atoms affect thermal transport. The MD technique is chosen for its advantage in addressing individual atom mass and ordering in the alloy. Optimized Able-Tersoff EIPs were used to describe the ternary alloys owing to their demonstrated success in

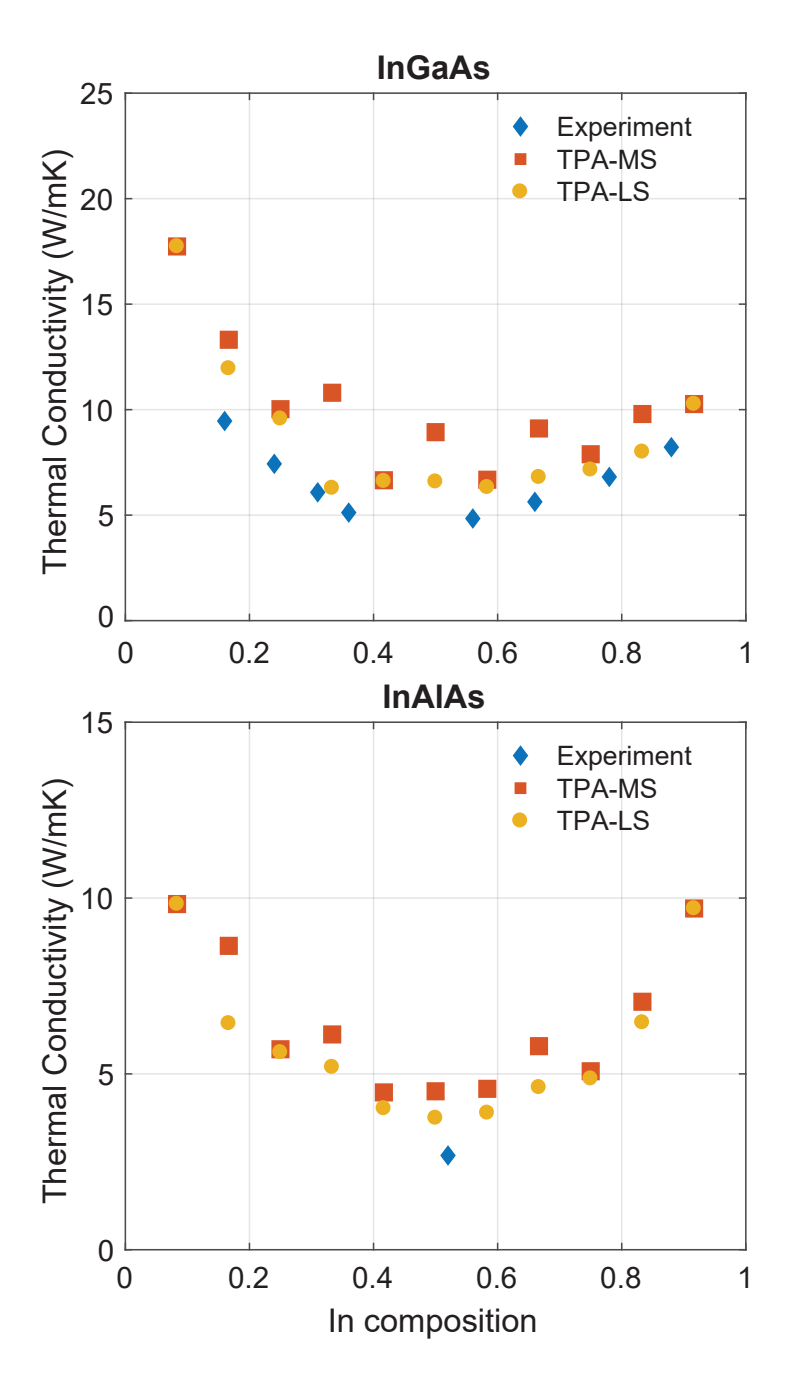


Figure 6.6: Calculated RT TC of InGaAs and InAlAs with perfect TPA ordering and various In compositions. Red squares and yellow dots show the results from the most-symmetric (MS) and least-symmetric (LS) structures. Experimental measurements[4, 5] are shown in blue diamonds.

describing III-V binary materials and their nearest-neighbor cutoffs that lend themselves to application in alloys.

We first optimized the Able-Tersoff potentials by matching the calculated phonon dispersion to experiments. We also matched the calculated temperature-dependent TC to experiment so the EIPs would capture higher orders in phonon-phonon interaction that are key in thermal transport. The quantum correction to the temperature was also accounted for in the simulations.

The optimized potentials were used to describe ternary alloys with both random and ordered structures. For random alloys, we compared the cases where atom masses were explicitly considered versus where they were all replaced with the averaged VCA mass, as is commonly done within the Boltzmann transport framework. The results showed that explicit atomic mass drastically reduces the TC of ternary alloys. The larger the mass difference between the cations in the alloy, the larger the discrepancy between explicit-mass and averaged-mass (VCA) TC results. We conclude that, when cation masses differ a lot (as is the case of $In_xAl_{1-x}As$), it is essential to include atom masses explicitly and any calculation that relies on VCA is likely inaccurate.

Moreover, measured thermal conductivities of ternary alloys are higher than calculations with either explicit or VCA mass and random positioning of cations, which led us to look at longer-range order in alloys. We considered perfectly ordered In_{0.5}Ga_{0.5}As and In_{0.5}Al_{0.5}As with both CuPt-B and CuAu-I types order and the corresponding lattice-matched alloys In_{0.53}Ga_{0.47}As and In_{0.52}Al_{0.48}As. Order in ternary alloys considerably raises TC. By adding random disorder to the lattice-matched alloys In_{0.53}Ga_{0.47}As and In_{0.52}Al_{0.48}As, we found that experimental results could be reproduced with levels of disorder close to 2% in In_{0.53}Ga_{0.47}As and 8% in In_{0.52}Al_{0.48}As.

We also studied perfectly ordered TPA alloys $In_xGa_{1-x}As$ and $In_xAl_{1-x}As$ with various compositions x. We found that more symmetry in the alloy led to higher TC, while the alloys with the least symmetry still yielded higher TC than experiments, indicating the existence of disorder in experiment.

In conclusion, in modeling thermal transport in III-V ternary alloys, it is crucial to include both the explicit masses of atoms and the effects of long-range order. The measured TC for III-V ternary alloys is likely a result of the competition between the two: reduction in TC stemming from mass-difference scattering associated with random disorder and an increase in TC associated with order in the alloy structure. These notions should be incorporated into other techniques for calculating thermal transport in alloys, and highlight the importance of critically evaluating the range of validity of even very common approximations, such as the VCA.

Appendix A: Algorithm for Choosing Wave Vector

A.1 Probability Distribution in Polar Coordinates

The starting point of choosing a wave vector is a fixed isoenergy curve from the already chosen ω and b for the given phonon. Figure A.1 shows a set of isoenergy curves (separated by 2×10^{13} rad/s) for the TA mode (the other two modes have similar curves). As we can see, the curves have near-radial symmetry, thus we use polar coordinates for convenience. Further, the 1BZ has 12-fold symmetry following the graphene lattice, so we would only need to consider the irreducible wedge (shaded area in Fig. A.1), and map it onto anyone of its counterparts with equal probability. Since we know the phonon energy and branch, only a polar angle θ is needed to uniquely find a wave vector \mathbf{q} . Here we choose the rejection technique to find the appropriate angle and then calculate the wave vector \mathbf{q} .

Evaluating the probability of a phonon having angle θ on a particular isoenergy curve ω is similar to a discretized version of phonon DOS calculation detailed in Sec. 3.1.2. The probability is represented by

$$p(\omega, \theta) \propto D_{\rm b}(\omega, \theta) \propto \frac{arc(\theta - \delta\theta, \theta + \delta\theta)}{|\mathbf{v}_g(\omega, \theta)|}.$$
 (A.1)

where $arc(\theta - \delta\theta, \theta + \delta\theta)$ is the arc length on the isoenergy curve between $(\theta - \delta\theta, \theta + \delta\theta)$ and $|\mathbf{v}_g(\omega, \theta)|$ is the magnitude of group velocity (we assume the group velocity is constant along the small arc). To make a rejection table, we need to discretize both the angular frequency and the angle in irreducible wedge. For the frequency, we still use the same discretization as in Sec. 3.2.1. For the angle, we divide the central angle of the irreducible wedge $(\theta_{\text{max}} = \frac{\pi}{6})$ into N_a equal intervals with $\Delta\theta = \frac{\theta_{\text{max}}}{N_a}$. The central frequency in the *i*th interval is $\theta_{c,i} = (2i-1)\frac{\Delta\theta}{2}$. We evaluate (A.1) only at discrete points $(\omega_{c,i}, \theta_{c,j})$ and get a $N_{\text{int}} \times N_a$ interpolation table. For any $0 < \omega < \omega_{\text{max}}$ and $0 < \theta < \theta_{\text{max}}$ we can get the probability of having a phonon from linear interpolation. We find that $N_a = 100$ serves the purpose of accurate interpolation.

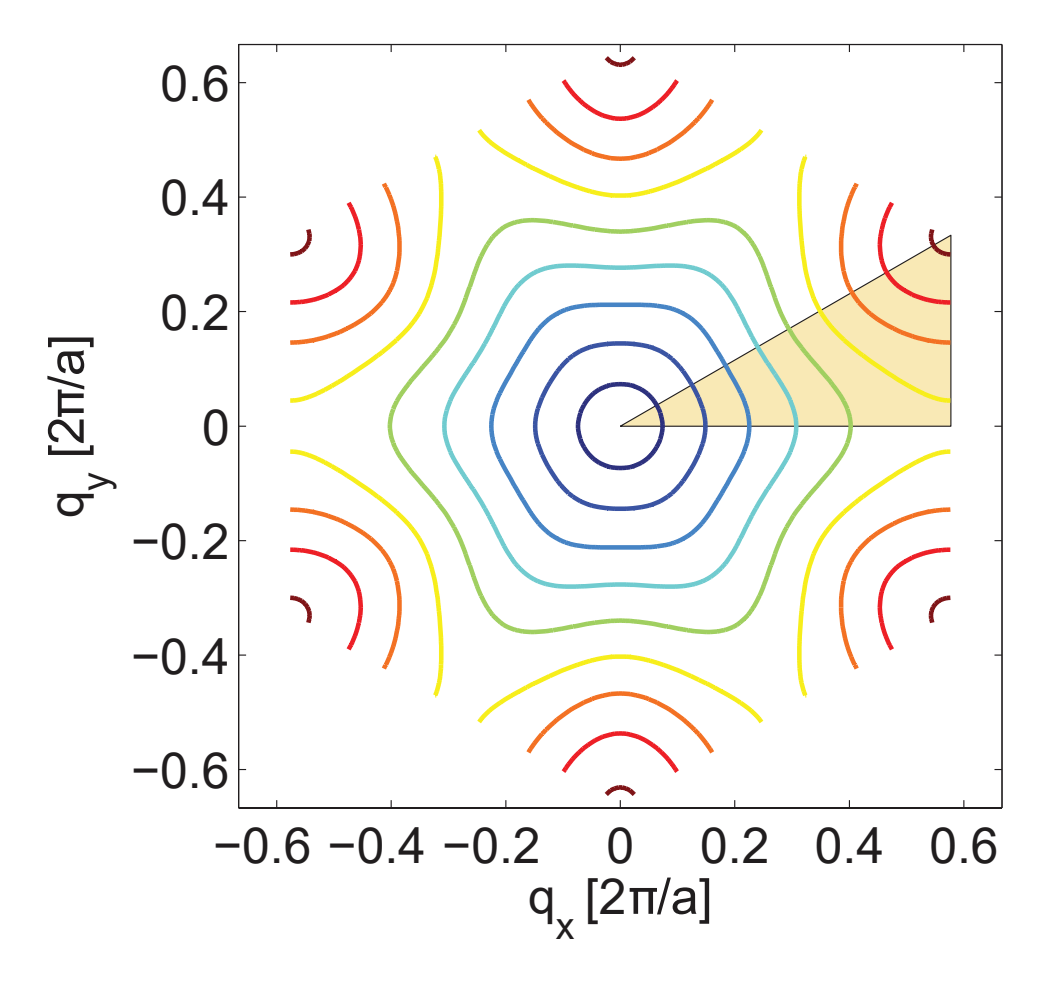


Figure A.1: Isoenergy curves in the 1BZ for TA-branch phonons. The neighboring curves are separated by 2×10^{13} rad/s and the shaded region in the black triangle is the irreducible wedge in the 1BZ.

Another effect caused by the full dispersion is that the group velocity at which phonons travel is no longer parallel to their wave vectors. So an extra step is needed to find the group velocity $\mathbf{v}_g(\omega, \theta)$ associated with the chosen \mathbf{q} . For each of the $N_{\text{int}} \times N_{\text{a}}$ discrete points $(\omega_{\text{c},i}, \theta_{\text{c},j})$ where we evaluated the probability, we also evaluate the group velocity $\mathbf{v}_g(\omega_{\text{c},i}, \theta_{\text{c},j})$ using finite difference method. Since the group velocity is a vector, we store each direction in a separate table, $v_{\text{x}}(\omega_{\text{c},i}, \theta_{\text{c},j})$ and $v_{\text{y}}(\omega_{\text{c},i}, \theta_{\text{c},j})$. Figure A.2 shows a point and its associated \mathbf{q} and \mathbf{v}_g . The shaded area shows the irreducible wedge.

A.2 Lookup Tables and Rejection Technique

We now have all the tables we need for phonon generation: the probability table $p(\omega_{c,i}, \theta_{c,j})$ and the two components of group velocity table $v_x(\omega_{c,i}, \theta_{c,j})$ and $v_y(\omega_{c,i}, \theta_{c,j})$. We need a set of these tables for each branch, and that makes $3 \times 3 = 9$ tables in total. All the tables are $N_{\text{int}} \times N_{\text{a}}$ (in our case 2500×100) in size and are pre-calculated and recorded before the actual simulation.

The first thing in actually choosing the phonon wave vector is to interpolate in each of the three 2D tables for our chosen branch b and get three 1D tables associated with our specified frequency level ω . The interpolation process for the three tables is the same and we would just show the probability table $p(\omega_{c,i}, \theta_{c,j})$ as an example. Again using the bisection algorithm, we can find the index m satisfying $\omega_{c,m} < \omega < \omega_{c,m+1}$. Then the probability of finding a phonon with angle $\theta_{c,j}$ at level ω is obtained from the weighted average of $p(\omega_{c,m}, \theta_{c,j})$ and $p(\omega_{c,m+1}, \theta_{c,j})$.

$$p(\theta_{c,j})|_{\omega} = p(\omega_{c,m}, \theta_{c,j}) \cdot (1 - d) +$$

$$p(\omega_{c,m+1}, \theta_{c,j}) \cdot d, \quad j = 1 \dots N_{a},$$
(A.2)

where the weighting factor is $d = \frac{\omega - \omega_{c,m}}{\Delta \omega}$. Now we can normalize this 1D probability table so that the maximal value in the table is unity. Note that we can only normalize the probability table after interpolation between frequency levels. We still call the normalized table $p(\theta_{c,j})|_{\omega}$. For the velocities, we get $v_x(\theta_{c,j})|_{\omega}$ and $v_y(\theta_{c,j})|_{\omega}$ tables in the same way except that we do

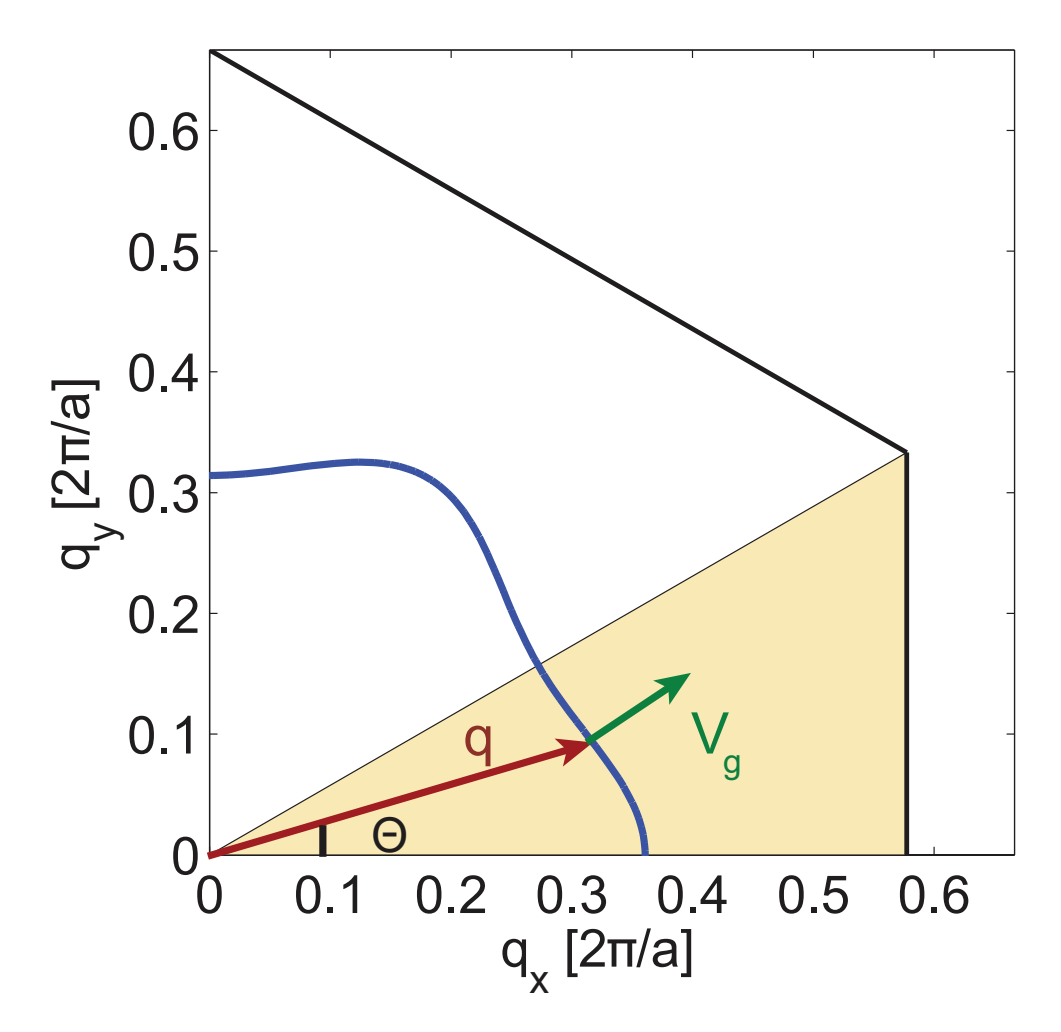


Figure A.2: A typical isoenergy curve ($\omega = 9 \times 10^{13} \text{ rad/s}$). The shaded area shows the irreducible wedge. Angle θ fixes a point at the curve and the associated wave vector \mathbf{q} and group velocity \mathbf{v}_g is shown.

not normalize them. Now we are working only on the frequency level ω , so we omit the subscript ω and just call the tables $p(\theta_{c,j})$, $v_{x,g}(\theta_{c,j})$, and $v_{x,g}(\theta_{c,j})$ from now on for brevity.

For a typical ω value, the probability table looks like Fig. A.3 (the figure shows the table for frequency level $\omega = 3 \times 10^{13}$ rad/s in TA-branch). We use the rejection technique with this probability graph for choosing the angle. Draw a pair of random numbers (R_4, R_5) (both R_4 and R_5 are between 0 and 1). We would use R_4 to get the tentative angle $\theta = R_4 \cdot \theta_{\text{max}}$ and compare R_5 with the probability to decide whether we accept the angle or not. To find the probability associated with angle θ , we seek the index n satisfying $\theta_n < \theta < \theta_{n+1}$ and interpolate between the two:

$$p(\theta) = p(\theta_{n}) \cdot (1 - d') + p(\theta_{n+1}) \cdot d', \tag{A.3}$$

where $d' = \frac{\theta - \theta_n}{\Delta \theta}$ is the weighting factor. If $R_5 < p(\theta)$, the angle is accepted and a point has been uniquely chosen in the irreducible wedge. We then use the $v_x(\theta_{c,j})$ and $v_y(\theta_{c,j})$ tables to get the group velocity v_x and v_y for the phonon at this point. Otherwise, the angle should be rejected, and we go back to drawing random number pairs (R_4, R_5) until one angle is accepted.

A.3 Mapping to The Whole 1BZ

Since we are working with the irreducible wedge, a last step to map the point we found in irreducible 1BZ to the whole 1BZ is needed. and modify the group velocity accordingly. The twelve equivalent triangles in 1BZ are shown in Fig. A.4 and we number them counterclockwise. A random number R_6 is used to choose one of the triangles and the index of the chosen triangle is ceiling($12 \times R_6$). Then the final group velocities $v_{\rm x}^{\rm final}$ and $v_{\rm y}^{\rm final}$ can be obtained from $v_{\rm x}$ and $v_{\rm y}$ by simple combinations of rotation and flipping according to the symmetry. The mapping rules are shown in Table A.1. After the mapping, we finally have a phonon satisfying all the distribution requirements and we can add this phonon to a random position in its cell.

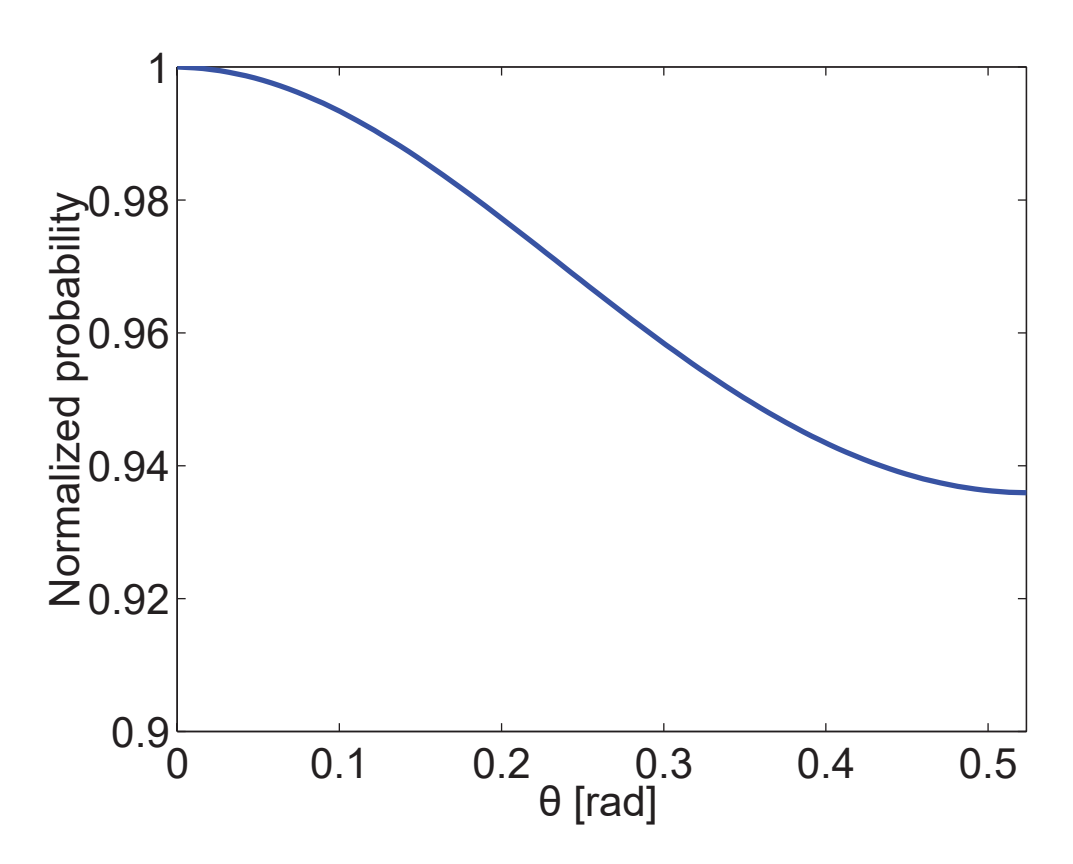


Figure A.3: A typical normalized probability versus angle curve for phonon generation. Here the frequency level is at $\omega=3\times10^{13}$ rad/s in TA-branch.

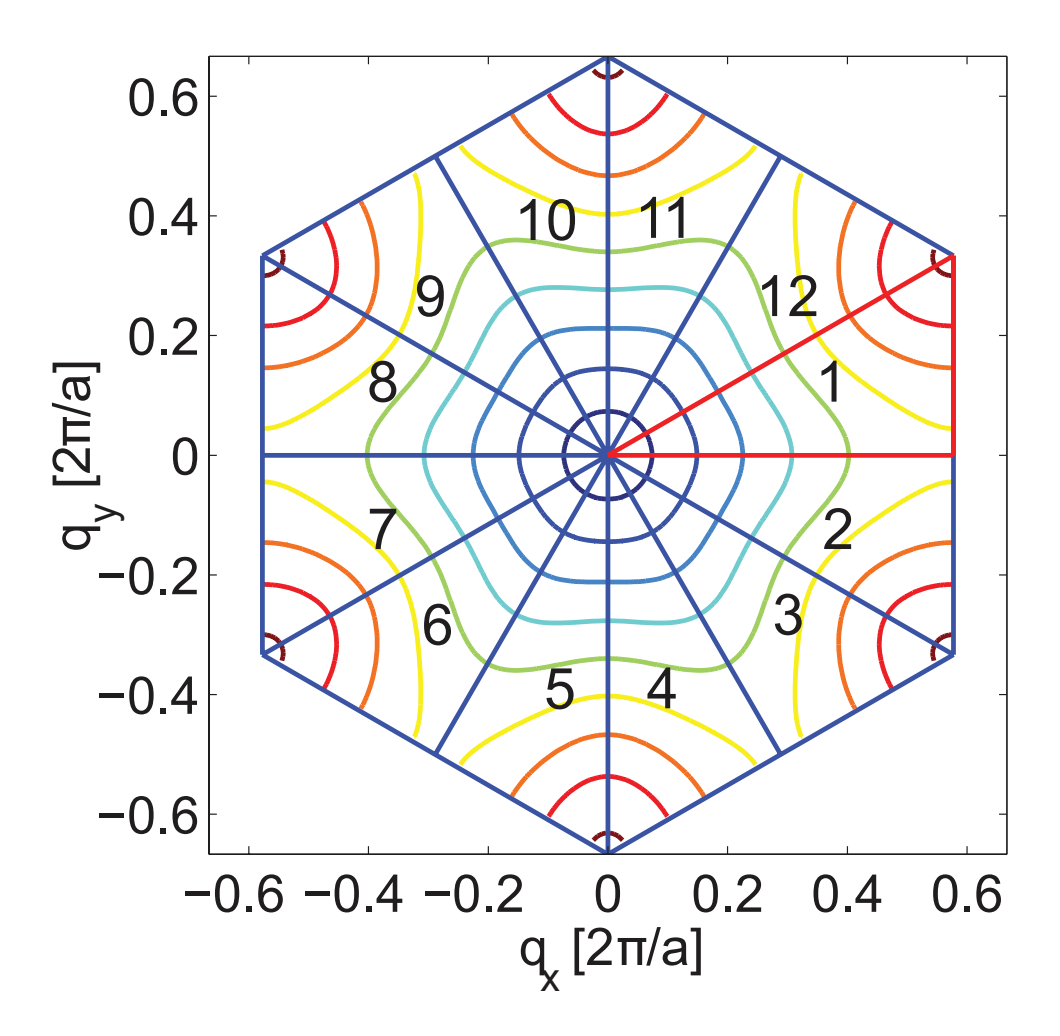


Figure A.4: Twelve equivalent triangles in 1BZ numbered counter-clockwise.

Index	1	2	3
$v_{\mathrm{x}}^{\mathrm{final}}$	v_{x}	$\frac{1}{2}v_{\mathbf{x}} + \frac{\sqrt{3}}{2}v_{\mathbf{y}}$	$\frac{1}{2}v_{\mathbf{x}} - \frac{\sqrt{3}}{2}v_{\mathbf{y}}$
$v_{\mathrm{y}}^{\mathrm{final}}$	$v_{ m y}$	$\frac{\sqrt{3}}{2}v_{\mathrm{x}} - \frac{1}{2}v_{\mathrm{y}}$	$\frac{\sqrt{3}}{2}v_{\mathbf{x}} + \frac{1}{2}v_{\mathbf{y}}$
Index	4	5	6
$v_{\mathrm{x}}^{\mathrm{final}}$	$-\frac{1}{2}v_{\mathbf{x}} + \frac{\sqrt{3}}{2}v_{\mathbf{y}}$	$-\frac{1}{2}v_{\mathbf{x}} - \frac{\sqrt{3}}{2}v_{\mathbf{y}}$	$-v_{\mathrm{x}}$
$v_{\mathrm{y}}^{\mathrm{final}}$	$\frac{\sqrt{3}}{2}v_{\mathbf{x}} + \frac{1}{2}v_{\mathbf{y}}$	$\frac{\sqrt{3}}{2}v_{\mathbf{x}} - \frac{1}{2}v_{\mathbf{y}}$	$v_{ m y}$
Index	7	8	9
$v_{\mathrm{x}}^{\mathrm{final}}$	$-v_{\rm x}$	$-\frac{1}{2}v_{\mathbf{x}} - \frac{\sqrt{3}}{2}v_{\mathbf{y}}$	$-\frac{1}{2}v_{\mathbf{x}} + \frac{\sqrt{3}}{2}v_{\mathbf{y}}$
$v_{\mathrm{y}}^{\mathrm{final}}$	$v_{ m y}$	$-\frac{\sqrt{3}}{2}v_{\mathbf{x}} + \frac{1}{2}v_{\mathbf{y}}$	$-\frac{\sqrt{3}}{2}v_{\mathbf{x}} - \frac{1}{2}v_{\mathbf{y}}$
Index	10	11	12
$v_{\mathrm{x}}^{\mathrm{final}}$	$\frac{1}{2}v_{\mathbf{x}} - \frac{\sqrt{3}}{2}v_{\mathbf{y}}$	$\frac{1}{2}v_{\mathbf{x}} + \frac{\sqrt{3}}{2}v_{\mathbf{y}}$	v_{x}
$v_{\mathrm{y}}^{\mathrm{final}}$	$-\frac{\sqrt{3}}{2}v_{\mathbf{x}} - \frac{1}{2}v_{\mathbf{y}}$	$\frac{\sqrt{3}}{2}v_{\mathbf{x}} - \frac{1}{2}v_{\mathbf{y}}$	$v_{ m y}$

Table A.1: Mapping rule of calculating the final group velocities $v_{\rm x}^{\rm final}$ and $v_{\rm y}^{\rm final}$ from the group velocities $v_{\rm x}$ and $v_{\rm y}$ in the irreducible wedge of the 1BZ according to the triangle index.

A final note, GNRs could have different orientations, with the armchair (AGNR) and zigzag (ZGNR) nanoribbon orientations being highly symmetric (Fig. 3.5). The presentation thus far applies to phonon in armchair GNRs (AGNRs). The only modification needed to simulate the transport in other orientations is to rotate \mathbf{v}_g with the angle Θ_o between the armchair orientation and the simulated orientation in phonon generation process. In particular, for zigzag GNRs (ZGNRs), the rotation angle is $\Theta_o = \frac{\pi}{6}$.

Appendix B: Parameterization of Isotropic Dispersion Relation in III-V Binary Materials

In order to calculate the thermal conductivity with full dispersion relation, we need to calculate and store the information for each material, which requires a lot of computation time and memory. However, it is a necessity in our case. First, we want to be able to calculate the thermal conductivity of a ternary materials with any given composition for which experimental work may generally not be available. Besides, experiments cannot give us the dispersion information on any composition we want. Figure B.1 shows the exact phonon dispersion of $In_{0.53}Ga_{0.47}As$ along highly symmetric directions calculated from ABCM. As we can see, the dispersion is not isotropic, and two TA branches are degenerate along the [100] $(\Gamma - X)$ direction. Also, we can see that the isotropic Debye approximation or the sine approximation of the dispersion are not ideal in capturing the features.

Thermal conductivity calculation of the three binary compounds (Figs. S1-S3) show that using isotropic dispersion underestimates thermal conductivity for the binaries, primarily because the two TA branches are not actually degenerate (Fig. B.1), and TA2 carries more heat than TA1 because of the higher average group velocity. The isotropic dispersion also overestimates the thermal conductivity of ternary materials, mainly because the phonon DOS calculated from the isotropic dispersion is much smaller than that from full dispersion (Fig. B.3).

To take advantage of the work we have done, and make it easier to get a sense of what the dispersion relation of a ternary compounds with a random composition is like, we fit our full dispersion data along [100] direction with a quadratic expression, which has been shown to perform well in materials with similar crystal structure, such as Si[141] and GaN[56]. With

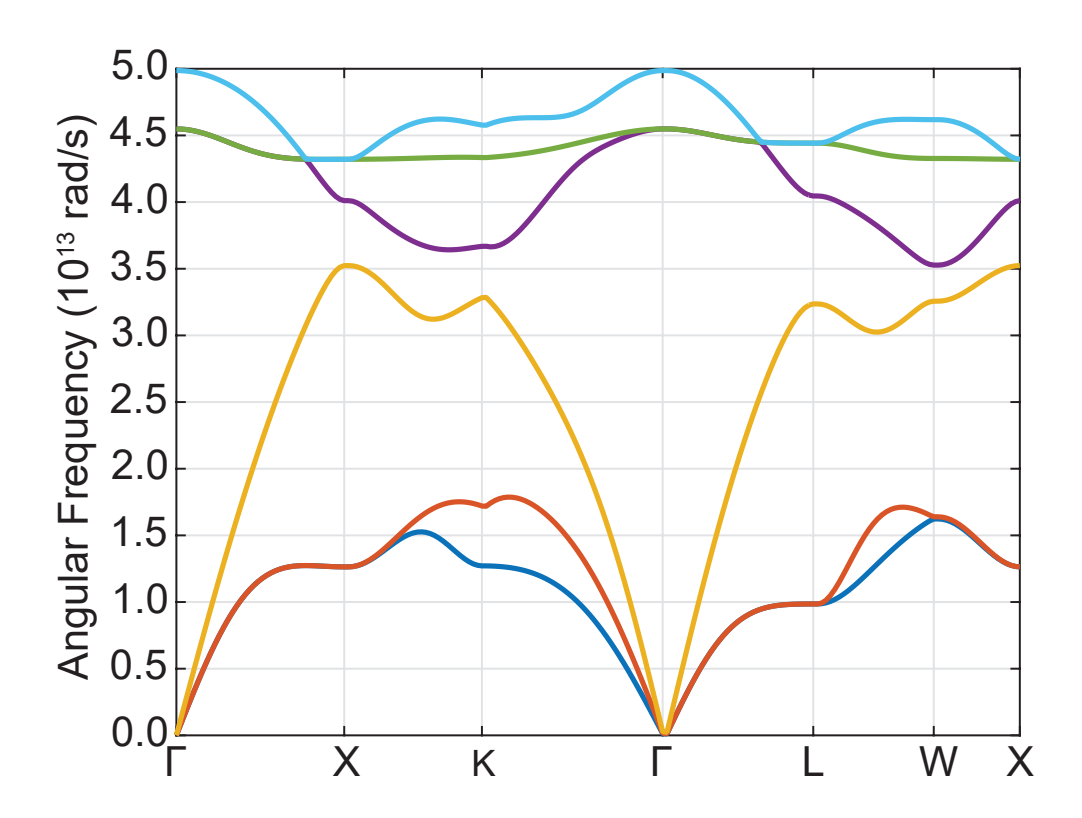


Figure B.1: Typical phonon dispersion of ternary group III arsenide compound $(In_{0.53}Ga_{0.47}As)$ along highly symmetric directions.

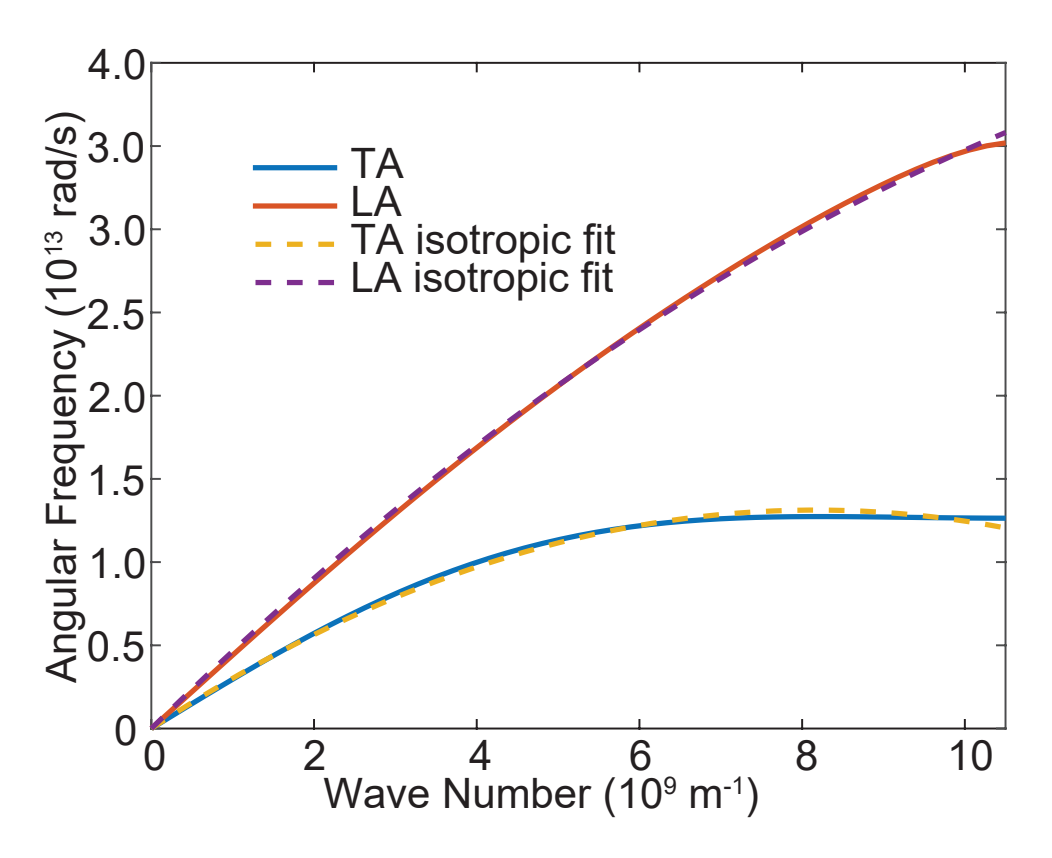


Figure B.2: Comparison of the full dispersion with isotropic fit along [100] direction for $In_{0.53}Ga_{0.47}As$.

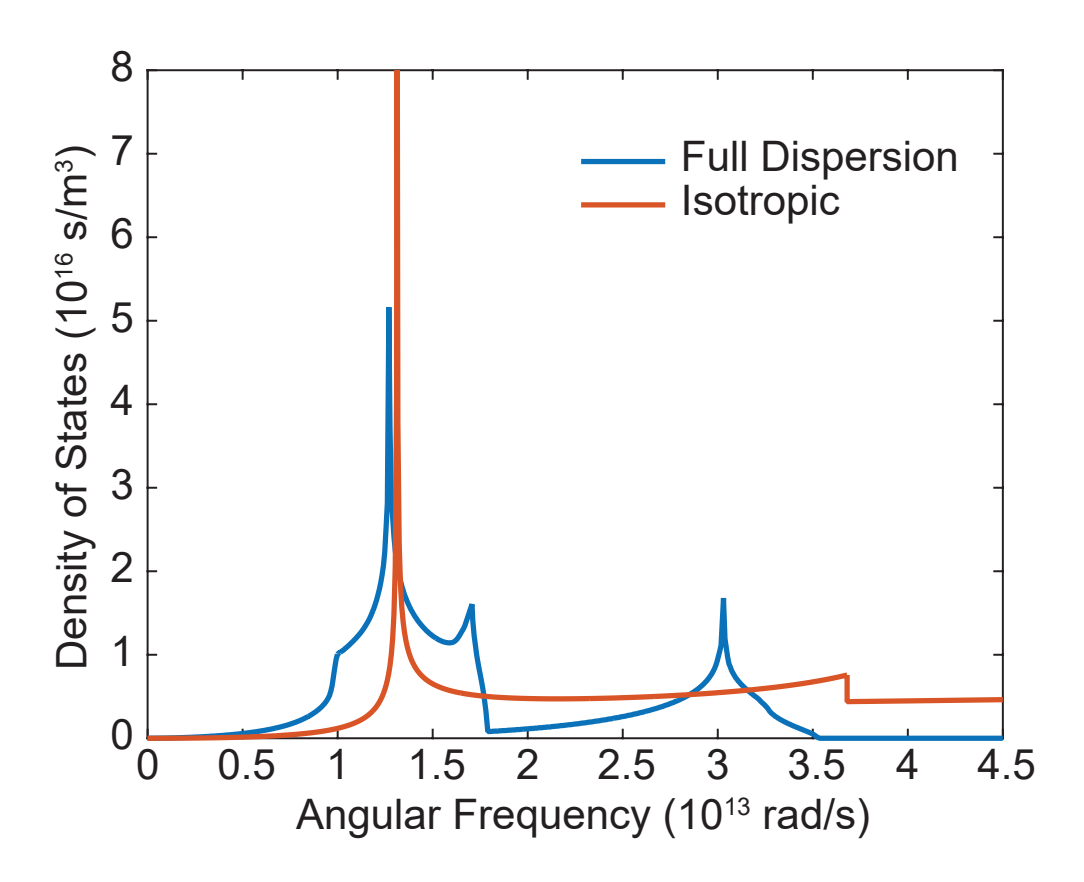


Figure B.3: Comparison of the phonon DOS calculated from the full dispersion and the isotropic quadratic fit for $\rm In_{0.53}Ga_{0.47}As$.

two TA branches being degenerate, the dispersion relation reads

$$\omega_{b}(q) = \begin{cases} v_{s}^{T}q + c^{T}q^{2}, & b = TA \\ v_{s}^{L}q + c^{L}q^{2}, & b = LA, \end{cases}$$
(B.1)

where v_s^T and v_s^L are the sound velocity of two branches and c^T and c^L are the corresponding quadratic coefficients. Note that everything reduces to a scalar in the isotropic approximation.

Figure B.2 shows that the expression is a good fit to the dispersion. We report the parameters in our quadratic fit so that one can get an easy and reasonably accurate estimate of the phonon dispersion of ternary group-III arsenide materials with any composition. Figures B.4 and B.5 show the two fitting parameters of InGaAs as a function of In composition. We find that both v_s and c fit well to a quadratic expression

$$v_{s}^{b}(x) = v_{s2}^{b}x^{2} + v_{s1}^{b}x + v_{s0}^{b};$$

$$c^{b}(x) = c_{2}^{b}x^{2} + c_{1}^{b}x + c_{0}^{b},$$
(B.2)

where b = TA or LA.

We have calculated the parameters for three types of ternary compounds, $In_xGa_{1-x}As$, $In_xAl_{1-x}As$, and $Al_xGa_{1-x}As$, and they are reported in Table B.1. The isotropic approximation (Eq. (B.1)) to the full dispersion gives a fairly good estimate of the sound velocity. The calculated thermal conductivity based on the isotropic approximation does differ from that calculated with full dispersion: $\kappa_{iso} \approx 0.6\kappa_{full}$ for binaries and $\kappa_{iso} \approx 1.2\kappa_{full}$ for almost evenly mixed ternaries. The error is in between when a ternary is not an even mix of two binaries. However, if high accuracy is not critical, good estimates are possible with isotropic dispersions that use the parameters given in Table B.1.

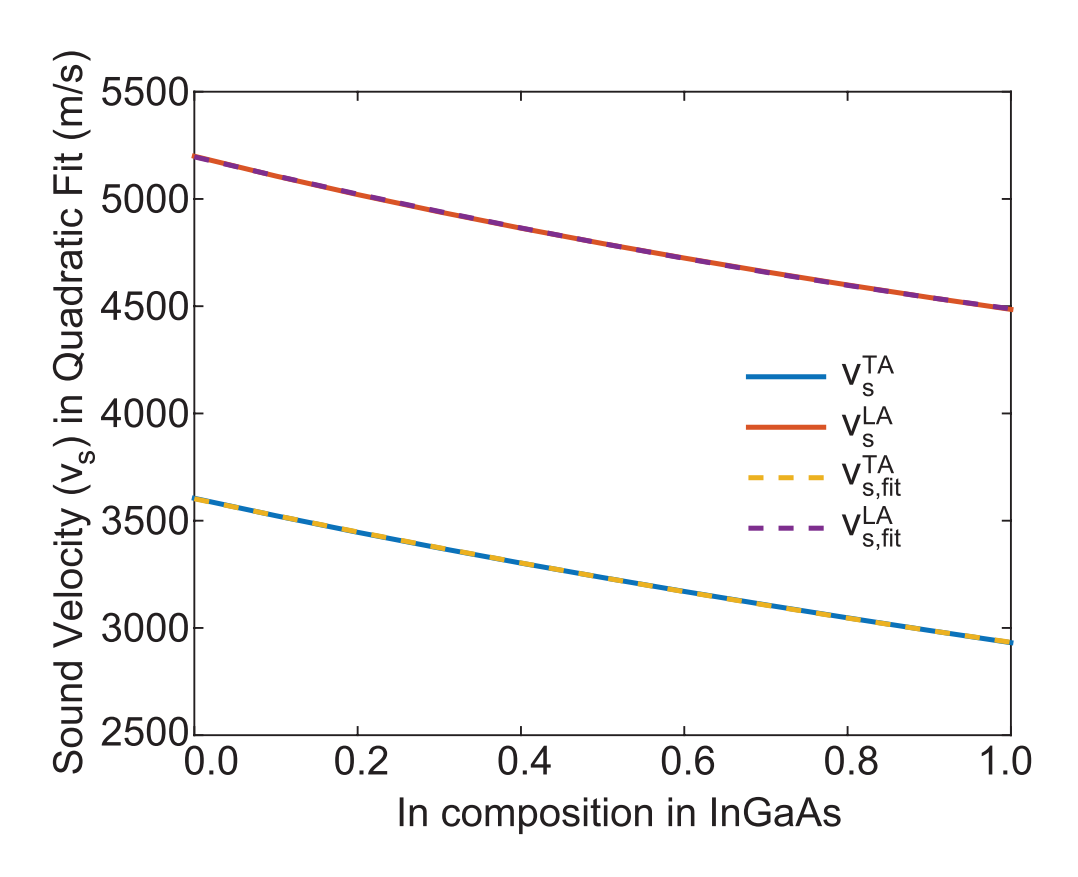


Figure B.4: Sound velocity of the quadratic fit to dispersion of InGaAs along [100] direction as a function of In composition.

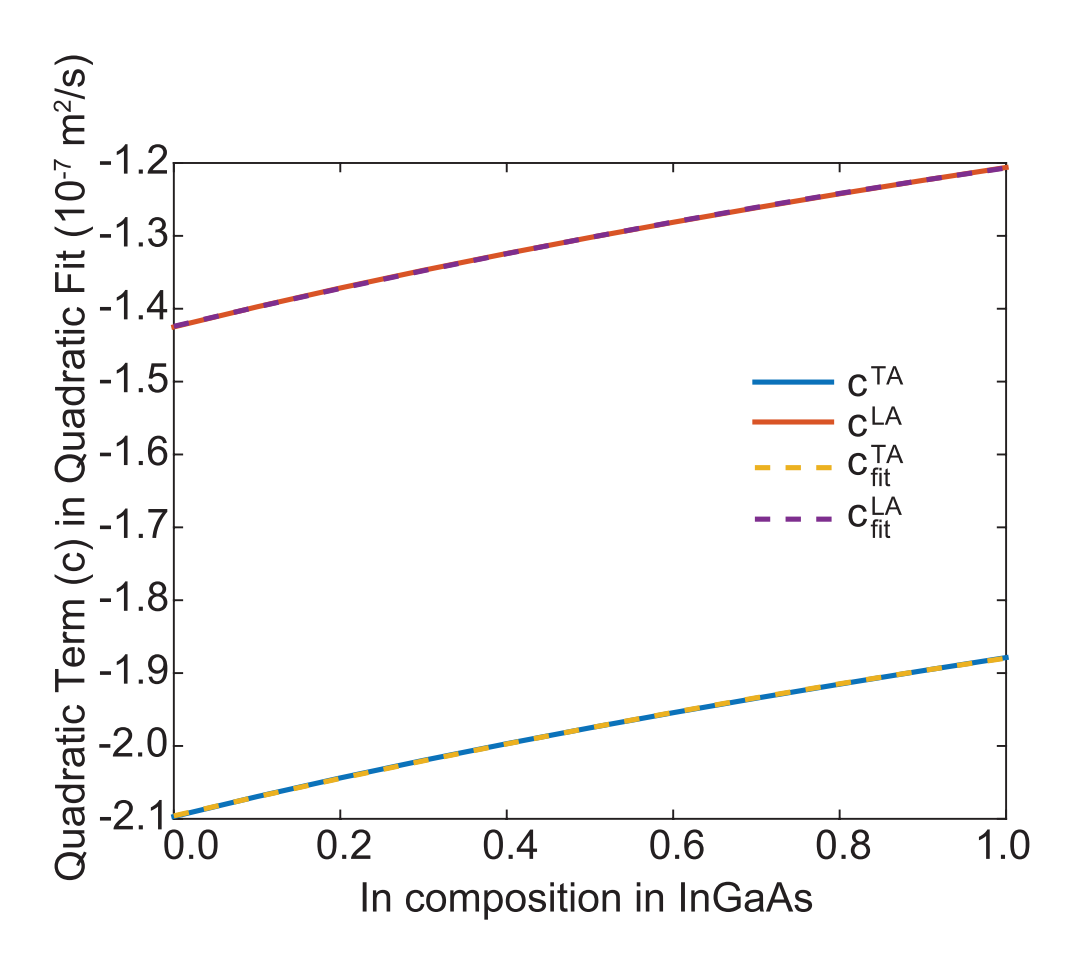


Figure B.5: Quadratic term of the quadratic fit to dispersion of InGaAs along [100] direction as a function of In composition.

InGaAs	InAlAs	AlGaAs
130.50	116.59	555.58
-800.80	-275.19	422.04
3602.3	4553.7	3616.6
-5e-9	-6.2e-8	-3.2e-8
2.7e-8	1.3e-7	-2.4e-8
-2.1e-7	-2.6e-7	-2.1e-7
199.94	165.43	782.56
-908.6	-359.84	537.55
5196.3	6480.0	5216.3
-5.3e-9	-4.7e-8	-2.3e-8
2.7e-8	1.1e-7	-1.8e-8
-1.4e-7	-1.8e-7	-1.4e-7
	130.50 -800.80 3602.3 -5e-9 2.7e-8 -2.1e-7 199.94 -908.6 5196.3 -5.3e-9 2.7e-8	130.50 116.59 -800.80 -275.19 3602.3 4553.7 -5e-9 -6.2e-8 2.7e-8 1.3e-7 -2.1e-7 -2.6e-7 199.94 165.43 -908.6 -359.84 5196.3 6480.0 -5.3e-9 -4.7e-8 2.7e-8 1.1e-7

Table B.1: Fitting parameters for sound velocity and quadratic coefficient to get isotropic dispersion.

LIST OF REFERENCES

- M. N. Luckyanova, J. A. Johnson, A. A. Maznev, J. Garg, A. Jandl, M. T. Bulsara,
 E. A. Fitzgerald, K. A. Nelson, and G. Chen, "Anisotropy of the thermal conductivity in gaas/alas superlattices," *Nano Lett.*, vol. 13, no. 9, pp. 3973–3977, 2013.
- [2] M. Sayed, J. Jefferson, A. Walker, and A. Cullis, "Molecular dynamics simulations of implantation damage and recovery in semiconductors," *Nucl. Instrum. Methods Phys. Res. B*, vol. 102, no. 1, pp. 218 222, 1995.
- [3] T. Hammerschmidt, P. Kratzer, and M. Scheffler, "Analytic many-body potential for inas/gaas surfaces and nanostructures: Formation energy of inas quantum dots," *Phys. Rev. B*, vol. 77, p. 235303, Jun 2008.
- [4] M. Abrahams, R. Braunstein, and F. Rosi, "Thermal, electrical and optical properties of (in,ga)as alloys," J. Phys. Chem. Solids, vol. 10, no. 23, pp. 204 210, 1959.
- [5] Y. K. Koh, S. L. Singer, W. Kim, J. M. O. Zide, H. Lu, D. G. Cahill, A. Majumdar, and A. C. Gossard, "Comparison of the 3 method and time-domain thermoreflectance for measurements of the cross-plane thermal conductivity of epitaxial semiconductors," *J. Appl. Phys.*, vol. 105, no. 5, p. 054303, 2009.
- [6] G. Gilat and L. J. Raubenheimer, "Accurate numerical method for calculating frequency-distribution functions in solids," *Phys. Rev.*, vol. 144, pp. 390–395, Apr 1966.
- [7] S. Chen, A. L. Moore, W. Cai, J. W. Suk, J. An, C. Mishra, C. Amos, C. W. Magnuson, J. Kang, L. Shi, and R. S. Ruoff, "Raman measurements of thermal transport in suspended monolayer graphene of variable sizes in vacuum and gaseous environments.," ACS Nano, vol. 5, pp. 321–8, Jan 2011.
- [8] X. Xu, L. F. C. Pereira, Y. Wang, J. Wu, K. Zhang, X. Zhao, S. Bae, C. Tinh Bui, R. Xie, J. T. L. Thong, B. H. Hong, K. P. Loh, D. Donadio, B. Li, and B. Ozyilmaz, "Length-dependent thermal conductivity in suspended single-layer graphene.," *Nat. Commun.*, vol. 5, p. 3689, Jan 2014.

- [9] S. Chen, Q. Wu, C. Mishra, J. Kang, H. Zhang, K. Cho, W. Cai, A. a. Balandin, and R. S. Ruoff, "Thermal conductivity of isotopically modified graphene.," *Nat. Mater.*, vol. 11, pp. 203–7, Mar 2012.
- [10] V. E. Dorgan, A. Behnam, H. J. Conley, K. I. Bolotin, and E. Pop, "High-field electrical and thermal transport in suspended graphene.," *Nano Lett.*, vol. 13, pp. 4581–6, Oct 2013.
- [11] L. Lindsay, D. A. Broido, and T. L. Reinecke, "Ab initio thermal transport in compound semiconductors," Phys. Rev. B, vol. 87, p. 165201, Apr 2013.
- [12] C. A. Evans, D. Indjin, Z. Ikonic, P. Harrison, M. S. Vitiello, V. Spagnolo, and G. Scamarcio, "Thermal modeling of terahertz quantum-cascade lasers: Comparison of optical waveguides," *IEEE J. Quantum Electron.*, vol. 44, pp. 680–685, Jul 2008.
- [13] A. V. Inyushkin, A. N. Taldenkov, A. Y. Yakubovsky, A. V. Markov, L. Moreno-Garsia, and B. N. Sharonov, "Thermal conductivity of isotopically enriched ⁷¹gaas crystal," Semicond. Sci. Technol., vol. 18, pp. 685–688, Jun 2003.
- [14] R. O. Carlson, G. A. Slack, and S. J. Silverman, "Thermal conductivity of gaas and $gaas_{1-x}p_x$ laser semiconductors," J. Appl. Phys., vol. 36, no. 2, pp. 505–507, 1965.
- [15] A. Amith, I. Kudman, and E. F. Steigmeier, "Electron and phonon scattering in gaas at high temperatures," *Phys. Rev.*, vol. 138, pp. A1270–A1276, May 1965.
- [16] M. A. Afromowitz, "Thermal conductivity of ga1xalxas alloys," J. Appl. Phys., vol. 44, no. 3, pp. 1292–1294, 1973.
- [17] E. M. Heckman, L. P. Gonzalez, and S. Guha, "Measurement of optical and thermal properties of hg1-xcdxte," *Appl. Opt.*, vol. 47, pp. 578–582, Feb 2008.
- [18] P. V. Tamarin and S. S. Shalyt, "Thermal conductivity and thermoelectric power of indium arsenide at low temperatures," Sov. Phys. Semicond., vol. 5, pp. 1097–1098, Jun 1971.
- [19] G. Le Guillou and H. J. Albany, "Phonon conductivity of inas," *Phys. Rev. B*, vol. 5, pp. 2301–2308, Mar 1972.
- [20] R. Bowers, R. W. Ure, J. E. Bauerle, and A. J. Cornish, "Inas and insb as thermoelectric materials," *J. Appl. Phys.*, vol. 30, no. 6, pp. 930–934, 1959.
- [21] B. Abeles, "Lattice thermal conductivity of disordered semiconductor alloys at high temperatures," *Phys. Rev.*, vol. 131, pp. 1906–1911, Sep 1963.
- [22] S. Adachi, "Lattice thermal resistivity of iiiv compound alloys," J. Appl. Phys., vol. 54, no. 4, pp. 1844–1848, 1983.

- [23] T. Yao, "Thermal properties of alas/gaas superlattices," Appl. Phys. Lett., vol. 51, no. 22, pp. 1798–1800, 1987.
- [24] X. Y. Yu, G. Chen, A. Verma, and J. S. Smith, "Temperature dependence of thermophysical properties of gaas/alas periodic structure," Appl. Phys. Lett., vol. 67, no. 24, pp. 3554–3556, 1995.
- [25] W. S. Capinski, H. J. Maris, T. Ruf, M. Cardona, K. Ploog, and D. S. Katzer, "Thermal-conductivity measurements of gaas/alas superlattices using a picosecond optical pump-and-probe technique," *Phys. Rev. B*, vol. 59, pp. 8105–8113, Mar 1999.
- [26] W. Capinski and H. Maris, "Thermal conductivity of gaas/alas superlattices," *Physica B*, vol. 219220, no. 0, pp. 699 701, 1996.
- [27] A. Sood, J. A. Rowlette, C. G. Caneau, E. Bozorg-Grayeli, M. Asheghi, and K. E. Goodson, "Thermal conduction in latticematched superlattices of ingaas/inalas," *Appl. Phys. Lett.*, vol. 105, no. 5, 2014.
- [28] B. Dorner and D. Strauch, "Phonon dispersion sheets and group velocities in gaas," J. Phys. Condens. Matter, vol. 2, no. 6, p. 1475, 1990.
- [29] N. S. Orlova, "Variation of phonon dispersion curves with temperature in indium arsenide measured by x-ray thermal diffuse scattering," *Phys. Status Solidi B Basic Solid State Phys.*, vol. 119, no. 2, pp. 541–546, 1983.
- [30] R. Carles, N. Saint-Cricq, J. B. Renucci, M. A. Renucci, and A. Zwick, "Second-order raman scattering in inas," *Phys. Rev. B*, vol. 22, pp. 4804–4815, Nov 1980.
- [31] C. Kittel, *Introduction to Solid State Physics*. New York: John Wiley & Sons, Inc., 8th ed., 2004.
- [32] N. W. Ashcroft and N. D. Mermin, *Solid State Physics*. Philadelphia: Saunders College, 1976.
- [33] G. Chen, "Thermal conductivity and ballistic-phonon transport in the cross-plane direction of superlattices," *Phys. Rev. B*, vol. 57, pp. 14958–14973, Jun 1998.
- [34] M. N. Luckyanova, J. Garg, K. Esfarjani, A. Jandl, M. T. Bulsara, A. J. Schmidt, A. J. Minnich, S. Chen, M. S. Dresselhaus, Z. Ren, E. A. Fitzgerald, and G. Chen, "Coherent phonon heat conduction in superlattices," *Science*, vol. 338, no. 6109, pp. 936–939, 2012.
- [35] K. Y. Cheng, "Molecular beam epitaxy technology of iii-v compound semiconductors for optoelectronic applications," *Proc. IEEE*, vol. 85, pp. 1694–1714, Nov 1997.

- [36] K. Goetz, D. Bimberg, H. Jrgensen, J. Selders, A. V. Solomonov, G. F. Glinskii, and M. Razeghi, "Optical and crystallographic properties and impurity incorporation of gaxin1xas (0.44_ix_i0.49) grown by liquid phase epitaxy, vapor phase epitaxy, and metal organic chemical vapor deposition," *Journal of Applied Physics*, vol. 54, no. 8, pp. 4543–4552, 1983.
- [37] S. Mei, L. N. Maurer, Z. Aksamija, and I. Knezevic, "Full-dispersion monte carlo simulation of phonon transport in micron-sized graphene nanoribbons," *J. Appl. Phys.*, vol. 116, no. 16, p. 164307, 2014.
- [38] S. Mei and I. Knezevic, "Thermal conductivity of iii-v semiconductor superlattices," J. Appl. Phys., vol. 118, no. 17, p. 175101, 2015.
- [39] S. Mei, C. J. Foss, L. N. Maurer, O. Jonasson, Z. Aksamija, and I. Knezevic, "Boundaries, interfaces, point defects, and strain as impediments to thermal transport in nanostructures," in 2017 IEEE International Reliability Physics Symposium (IRPS), pp. 6A–1.1–6A–1.10, April 2017.
- [40] S. Mei and I. Knezevic, "Thermal conductivity of ternary iii-v semiconductor alloys: the role of mass difference and long-range order," J. Appl. Phys., submitted.
- [41] L. N. Maurer, S. Mei, and I. Knezevic, *Phonon Monte Carlo: Generating Random Variates for Thermal Transport Simulation*. Pan Stanford Publishing, 2017.
- [42] O. Jonasson, S. Mei, F. Karimi, J. Kirch, D. Botez, L. Mawst, and I. Knezevic, "Quantum transport simulation of high-power 4.6-m quantum cascade lasers," *Photonics*, vol. 3, no. 2, p. 38, 2016.
- [43] Y. B. Shi, S. Mei, O. Jonasson, and I. Knezevic, "Modeling quantum cascade lasers: Coupled electron and phonon transport far from equilibrium and across disparate spatial scales," *Fortschritte der Physik*, vol. 65, no. 6-8, pp. 1600084–n/a, 2017. 1600084.
- [44] S. Mei, Y. B. Shi, O. Jonasson, and I. Knezevic, Quantum Cascade Lasers: Electrother-mal Simulation. CRC Press, 2017.
- [45] D. Lacroix, K. Joulain, and D. Lemonnier, "Monte carlo transient phonon transport in silicon and germanium at nanoscales," *Phys. Rev. B*, vol. 72, p. 064305, Aug 2005.
- [46] E. B. Ramayya, L. N. Maurer, A. H. Davoody, and I. Knezevic, "Thermoelectric properties of ultrathin silicon nanowires," *Phys. Rev. B*, vol. 86, p. 115328, Sep 2012.
- [47] Z. Aksamija and I. Knezevic, "Lattice thermal conductivity of graphene nanoribbons: Anisotropy and edge roughness scattering," *Appl. Phys. Lett.*, vol. 98, no. 14, p. 141919, 2011.

- [48] R. Wu, R. Hu, and X. Luo, "First-principle-based full-dispersion monte carlo simulation of the anisotropic phonon transport in the wurtzite gan thin film," *J. of Appl. Phys.*, vol. 119, no. 14, p. 145706, 2016.
- [49] J.-H. Zou and B.-Y. Cao, "Phonon thermal properties of graphene on h-bn from molecular dynamics simulations," *Appl. Phys. Lett.*, vol. 110, no. 10, p. 103106, 2017.
- [50] R. Saito, G. Dresselhaus, and M. S. Dresselhaus, *Physical Properties of Carbon Nan-otubes*. London: Imperial College Press, 1998.
- [51] S. Mazumder and A. Majumdar, "Monte carlo study of phonon transport in solid thin films including dispersion and polarization," *J. Heat Transfer*, vol. 123, no. 4, p. 749, 2001.
- [52] Y. Chen, D. Li, J. R. Lukes, and A. Majumdar, "Monte carlo simulation of silicon nanowire thermal conductivity," *J. Heat Transfer*, vol. 127, no. 10, p. 1129, 2005.
- [53] D. Lacroix, K. Joulain, D. Terris, and D. Lemonnier, "Monte carlo simulation of phonon confinement in silicon nanostructures: Application to the determination of the thermal conductivity of silicon nanowires," *Appl. Phys. Lett.*, vol. 89, no. 10, p. 103104, 2006.
- [54] J. Randrianalisoa and D. Baillis, "Monte carlo simulation of steady-state microscale phonon heat transport," J. Heat Transfer, vol. 130, no. 7, p. 072404, 2008.
- [55] J.-P. M. Péraud and N. G. Hadjiconstantinou, "Efficient simulation of multidimensional phonon transport using energy-based variance-reduced monte carlo formulations," *Phys. Rev. B*, vol. 84, p. 205331, Nov 2011.
- [56] A. H. Davoody, E. B. Ramayya, L. N. Maurer, and I. Knezevic, "Ultrathin gan nanowires: Electronic, thermal, and thermoelectric properties," *Phys. Rev. B*, vol. 89, p. 115313, Mar 2014.
- [57] P. Klemens and D. Pedraza, "Thermal conductivity of graphite in the basal plane," *Carbon N. Y.*, vol. 32, no. 4, pp. 735–741, 1994.
- [58] L. Lindsay, W. Li, J. Carrete, N. Mingo, D. A. Broido, and T. L. Reinecke, "Phonon thermal transport in strained and unstrained graphene from first principles," *Phys. Rev. B*, vol. 89, p. 155426, Apr 2014.
- [59] X. Li, W. Cai, J. An, S. Kim, J. Nah, D. Yang, R. Piner, A. Velamakanni, I. Jung, E. Tutuc, S. K. Banerjee, L. Colombo, and R. S. Ruoff, "Large-area synthesis of highquality and uniform graphene films on copper foils.," *Science*, vol. 324, pp. 1312–4, Jun 2009.

- [60] A. Y. Serov, Z.-Y. Ong, and E. Pop, "Effect of grain boundaries on thermal transport in graphene," *Appl. Phys. Lett.*, vol. 102, p. 033104, 2013.
- [61] N. Petrone, C. R. Dean, I. Meric, A. M. van der Zande, P. Y. Huang, L. Wang, D. Muller, K. L. Shepard, and J. Hone, "Chemical vapor deposition-derived graphene with electrical performance of exfoliated graphene.," *Nano Lett.*, vol. 12, pp. 2751–6, Jun 2012.
- [62] G.-H. Lee, R. C. Cooper, S. J. An, S. Lee, A. van der Zande, N. Petrone, A. G. Hammerberg, C. Lee, B. Crawford, W. Oliver, J. W. Kysar, and J. Hone, "High-strength chemical-vapor-deposited graphene and grain boundaries.," *Science*, vol. 340, pp. 1073–6, May 2013.
- [63] I. Vlassiouk, S. Smirnov, I. Ivanov, P. F. Fulvio, S. Dai, H. Meyer, M. Chi, D. Hensley, P. Datskos, and N. V. Lavrik, "Electrical and thermal conductivity of low temperature cvd graphene: the effect of disorder.," *Nanotechnology*, vol. 22, p. 275716, Jul 2011.
- [64] Z. Aksamija and I. Knezevic, "Lattice thermal transport in large-area polycrystalline graphene," *Phys. Rev. B*, vol. 90, p. 035419, Jul 2014.
- [65] T. Klitsner, J. VanCleve, H. Fischer, and R. Pohl, "Phonon radiative heat transfer and surface scattering," *Phys. Rev. B*, vol. 38, no. 11, 1988.
- [66] A. a. Balandin, S. Ghosh, W. Bao, I. Calizo, D. Teweldebrhan, F. Miao, and C. N. Lau, "Superior thermal conductivity of single-layer graphene.," *Nano Lett.*, vol. 8, pp. 902–7, Mar 2008.
- [67] W. Cai, A. L. Moore, Y. Zhu, X. Li, S. Chen, L. Shi, and R. S. Ruoff, "Thermal transport in suspended and supported monolayer graphene grown by chemical vapor deposition.," *Nano Lett.*, vol. 10, pp. 1645–51, May 2010.
- [68] C. Faugeras, B. Faugeras, M. Orlita, M. Potemski, R. R. Nair, and A. K. Geim, "Thermal conductivity of graphene in corbino membrane geometry.," ACS Nano, vol. 4, pp. 1889–92, Apr 2010.
- [69] J.-U. Lee, D. Yoon, H. Kim, S. W. Lee, and H. Cheong, "Thermal conductivity of suspended pristine graphene measured by raman spectroscopy," *Phys. Rev. B*, vol. 83, p. 081419, Feb 2011.
- [70] M.-H. Bae, Z. Li, Z. Aksamija, P. N. Martin, F. Xiong, Z.-Y. Ong, I. Knezevic, and E. Pop, "Ballistic to diffusive crossover of heat flow in graphene ribbons.," *Nat. Com*mun., vol. 4, p. 1734, Jan 2013.
- [71] K. Yoon, G. Hwang, J. Chung, H. G. Kim, O. Kwon, K. D. Kihm, and J. S. Lee, "Measuring the thermal conductivity of residue-free suspended graphene bridge using null point scanning thermal microscopy," *Carbon N. Y.*, vol. 76, pp. 77–83, Sep 2014.

- [72] S. Ghosh, I. Calizo, D. Teweldebrhan, E. P. Pokatilov, D. L. Nika, A. A. Balandin, W. Bao, F. Miao, and C. N. Lau, "Extremely high thermal conductivity of graphene: Prospects for thermal management applications in nanoelectronic circuits," Appl. Phys. Lett., vol. 92, no. 15, p. 151911, 2008.
- [73] K. Saito, J. Nakamura, and A. Natori, "Ballistic thermal conductance of a graphene sheet," *Phys. Rev. B*, vol. 76, p. 115409, Sep 2007.
- [74] E. Muñoz, J. Lu, and B. I. Yakobson, "Ballistic thermal conductance of graphene ribbons.," *Nano Lett.*, vol. 10, pp. 1652–6, May 2010.
- [75] H. Tomita and J. Nakamura, "Ballistic phonon thermal conductance in graphene nanoribbons," J. Vac. Sci. Technol. B Microelectron. Nanom. Struct., vol. 31, no. 4, p. 04D104, 2013.
- [76] X. Li, X. Wang, L. Zhang, S. Lee, and H. Dai, "Chemically derived, ultrasmooth graphene nanoribbon semiconductors.," *Science*, vol. 319, pp. 1229–32, Feb 2008.
- [77] X. Jia, M. Hofmann, and V. Meunier, "Controlled formation of sharp zigzag and armchair edges in graphitic nanoribbons," *Science*, vol. 323, no. March, pp. 1701–1705, 2009.
- [78] J. Cai, P. Ruffieux, R. Jaafar, M. Bieri, T. Braun, S. Blankenburg, M. Muoth, A. P. Seitsonen, M. Saleh, X. Feng, K. Müllen, and R. Fasel, "Atomically precise bottom-up fabrication of graphene nanoribbons.," *Nature*, vol. 466, pp. 470–3, Jul 2010.
- [79] K. Kim, S. Coh, C. Kisielowski, M. F. Crommie, S. G. Louie, M. L. Cohen, and a. Zettl, "Atomically perfect torn graphene edges and their reversible reconstruction.," *Nat. Commun.*, vol. 4, p. 2723, Jan 2013.
- [80] P. Koskinen, S. Malola, and H. Häkkinen, "Self-passivating edge reconstructions of graphene," *Phys. Rev. Lett.*, vol. 101, p. 115502, Sep 2008.
- [81] c. Girit, J. Meyer, R. Erni, and M. Rossell, "Graphene at the edge: stability and dynamics," *Science* (80-.)., vol. 666, no. March, pp. 1705–1708, 2009.
- [82] Y. Xu, X. Chen, B.-L. Gu, and W. Duan, "Intrinsic anisotropy of thermal conductance in graphene nanoribbons," *Appl. Phys. Lett.*, vol. 95, no. 23, p. 233116, 2009.
- [83] Z. W. Tan, J.-S. Wang, and C. K. Gan, "First-principles study of heat transport properties of graphene nanoribbons.," *Nano Lett.*, vol. 11, pp. 214–9, Jan 2011.
- [84] Y. Wang, B. Qiu, and X. Ruan, "Edge effect on thermal transport in graphene nanoribbons: A phonon localization mechanism beyond edge roughness scattering," *Appl. Phys. Lett.*, vol. 101, no. 1, p. 013101, 2012.

- [85] J. Wang, X.-M. Wang, Y.-F. Chen, and J.-S. Wang, "Dimensional crossover of thermal conductance in graphene nanoribbons: a first-principles approach.," *J. Phys. Condens. Matter*, vol. 24, p. 295403, Jul 2012.
- [86] B. Kong, S. Paul, M. Nardelli, and K. Kim, "First-principles analysis of lattice thermal conductivity in monolayer and bilayer graphene," *Phys. Rev. B*, vol. 80, p. 033406, Jul 2009.
- [87] J. Faist, F. Capasso, D. L. Sivco, C. Sirtori, A. L. Hutchinson, and A. Y. Cho, "Quantum cascade laser," *Science*, vol. 264, no. 5158, pp. 553–556, 1994.
- [88] R. Köhler, A. Tredicucci, F. Beltram, H. E. Beere, E. H. Linfield, A. G. Davies, D. A. Ritchie, R. C. Iotti, and F. Rossi, "Terahertz semiconductor-heterostructure laser.," Nature, vol. 417, no. 6885, pp. 156–159, 2002.
- [89] M. Razeghi, N. Bandyopadhyay, Y. Bai, Q. Lu, and S. Slivken, "Recent advances in mid infrared (3-5μm) quantum cascade lasers," Opt. Mater. Express, vol. 3, pp. 1872– 1884, Nov 2013.
- [90] Y. Yao, A. J. Hoffman, and C. F. Gmachl, "Mid-infrared quantum cascade lasers," *Nat. Photonics*, vol. 6, no. 7, pp. 432–439, 2012.
- [91] M. Vitiello, G. Scamarcio, and V. Spagnolo, "Temperature dependence of thermal conductivity and boundary resistance in thz quantum cascade lasers," *IEEE J. Sel. Topics Quantum Electron.*, vol. 14, pp. 431–435, Mar 2008.
- [92] G. A. Slack and S. Galginaitis, "Thermal conductivity and phonon scattering by magnetic impurities in cdte," *Phys. Rev.*, vol. 133, pp. A253–A268, Jan 1964.
- [93] D. T. Morelli, J. P. Heremans, and G. A. Slack, "Estimation of the isotope effect on the lattice thermal conductivity of group iv and group iii-v semiconductors," *Phys. Rev. B*, vol. 66, p. 195304, Nov 2002.
- [94] M. Asen-Palmer, K. Bartkowski, E. Gmelin, M. Cardona, A. P. Zhernov, A. V. In-yushkin, A. Taldenkov, V. I. Ozhogin, K. M. Itoh, and E. E. Haller, "Thermal conductivity of germanium crystals with different isotopic compositions," *Phys. Rev. B*, vol. 56, pp. 9431–9447, Oct 1997.
- [95] T. Soma and H.-M. Kagaya, "Mode grneisen parameters for long-wave phonons of iii-v covalent compounds under pressure," *Phys. Status Solidi B*, vol. 130, no. 2, pp. 497–501, 1985.
- [96] T. Soma and H.-M. Kagaya, "Compression effect on elastic coefficients of alp, alas, and alsb compounds," *Phys. Status Solidi B*, vol. 139, no. 1, pp. K1–K4, 1987.

- [97] D. N. Talwar and M. Vandevyver, "Pressure-dependent phonon properties of iii-v compound semiconductors," *Phys. Rev. B*, vol. 41, pp. 12129–12139, Jun 1990.
- [98] S.-I. Tamura, "Isotope scattering of dispersive phonons in ge," *Phys. Rev. B*, vol. 27, pp. 858–866, Jan 1983.
- [99] H. J. Maris, "Phonon propagation with isotope scattering and spontaneous anharmonic decay," *Phys. Rev. B*, vol. 41, pp. 9736–9743, May 1990.
- [100] M. G. Holland, "Phonon scattering in semiconductors from thermal conductivity studies," *Phys. Rev.*, vol. 134, pp. A471–A480, Apr 1964.
- [101] A. Shore, A. Fritsch, M. Heim, A. Schuh, and M. Thoennessen, "Discovery of the arsenic isotopes," At. Data Nucl. Data Tables, vol. 96, no. 3, pp. 299 306, 2010.
- [102] J. E. Parrott, "Heat conduction mechanisms in semiconducting materials," Rev. Int. Hautes Temp. Refract., vol. 16, pp. 393–403, 1979.
- [103] S. Adachi, "Gaas, alas, and alxga1xas: Material parameters for use in research and device applications," *J. Appl. Phys.*, vol. 58, no. 3, pp. R1–R29, 1985.
- [104] M. T. Ramsbey, S. Tamura, and J. P. Wolfe, "Mode-selective scattering of phonons in a semi-insulating gaas crystal: A case study using phonon imaging," *Phys. Rev. B*, vol. 46, pp. 1358–1364, Jul 1992.
- [105] P. Klemens, "Thermal conductivity and lattice vibrational modes," in *Solid State Physics: Advances in Research and Applications* (F. Seitz and D. Turnbull, eds.), vol. 7, pp. 1–98, Academic Press, 1958.
- [106] W. Weber, "New bond-charge model for the lattice dynamics of diamond-type semi-conductors," *Phys. Rev. Lett.*, vol. 33, pp. 371–374, Aug 1974.
- [107] K. Rustagi and W. Weber, "Adiabatic bond charge model for the phonons in {A3B5} semiconductors," *Solid State Commun.*, vol. 18, no. 6, pp. 673 675, 1976.
- [108] S. Adachi, *Properties of Aluminium Gallium Arsenide*. London, United Kingdom: INSPEC, the Institution of Electrical Engineers, 1993.
- [109] B. F. Levine, K. K. Choi, C. G. Bethea, J. Walker, and R. J. Malik, "New 10 m infrared detector using intersubband absorption in resonant tunneling gaalas superlattices," Appl. Phys. Lett., vol. 50, no. 16, pp. 1092–1094, 1987.
- [110] S. Nakamura, M. Senoh, S.-I. Nagahama, N. Iwasa, T. Yamada, T. Matsushita, H. Kiyoku, Y. Sugimoto, T. Kozaki, H. Umemoto, M. Sano, and K. Chocho, "Ingan/gan/algan-based laser diodes with modulation-doped strained-layer superlattices grown on an epitaxially laterally overgrown gan substrate," Appl. Phys. Lett., vol. 72, no. 2, pp. 211–213, 1998.

- [111] D. G. Cahill, P. V. Braun, G. Chen, D. R. Clarke, S. Fan, K. E. Goodson, P. Keblinski, W. P. King, G. D. Mahan, A. Majumdar, H. J. Maris, S. R. Phillpot, E. Pop, and L. Shi, "Nanoscale thermal transport. ii. 20032012," *Appl. Phys. Rev.*, vol. 1, no. 1, 2014.
- [112] I. Hatta, Y. Sasuga, R. Kato, and A. Maesono, "Thermal diffusivity measurement of thin films by means of an ac calorimetric method," *Rev. Sci. Instrum.*, vol. 56, no. 8, pp. 1643–1647, 1985.
- [113] D. G. Cahill and R. O. Pohl, "Thermal conductivity of amorphous solids above the plateau," *Phys. Rev. B*, vol. 35, pp. 4067–4073, Mar 1987.
- [114] M. A. Panzer, M. Shandalov, J. Rowlette, Y. Oshima, Y. W. Chen, P. C. McIntyre, and K. E. Goodson, "Thermal properties of ultrathin hafnium oxide gate dielectric films," *IEEE Electron. Device Lett.*, vol. 30, pp. 1269–1271, Dec 2009.
- [115] G. Chen, C. L. Tien, X. Wu, and J. S. Smith, "Thermal diffusivity measurement of gaas/algaas thin-film structures," *J. Heat Transfer*, vol. 116, pp. 325–331, May 1994.
- [116] S.-M. Lee, D. G. Cahill, and R. Venkatasubramanian, "Thermal conductivity of sige superlattices," *Appl. Phys. Lett.*, vol. 70, no. 22, pp. 2957–2959, 1997.
- [117] S. T. Huxtable, A. R. Abramson, C.-L. Tien, A. Majumdar, C. LaBounty, X. Fan, G. Zeng, J. E. Bowers, A. Shakouri, and E. T. Croke, "Thermal conductivity of si/sige and sige/sige superlattices," *Appl. Phys. Lett.*, vol. 80, no. 10, pp. 1737–1739, 2002.
- [118] G. Chen, "Size and interface effects on thermal conductivity of superlattices and periodic thin-film structures," J. Heat Transfer, vol. 119, no. 2, p. 220, 1997.
- [119] P. K. Schelling, S. R. Phillpot, and P. Keblinski, "Phonon wave-packet dynamics at semiconductor interfaces by molecular-dynamics simulation," *Appl. Phys. Lett.*, vol. 80, no. 14, pp. 2484–2486, 2002.
- [120] D. G. Cahill, W. K. Ford, K. E. Goodson, G. D. Mahan, A. Majumdar, H. J. Maris, R. Merlin, and S. R. Phillpot, "Nanoscale thermal transport," J. Appl. Phys., vol. 93, no. 2, pp. 793–818, 2003.
- [121] I. M. Khalatnikov Zh. Eksp. Teor. Fiz., vol. 22, p. 687, 1952.
- [122] E. T. Swartz and R. O. Pohl, "Thermal boundary resistance," Rev. Mod. Phys., vol. 61, pp. 605–668, Jul 1989.
- [123] R. J. Stevens, L. V. Zhigilei, and P. M. Norris, "Effects of temperature and disorder on thermal boundary conductance at solidsolid interfaces: Nonequilibrium molecular dynamics simulations," *Int. J. Heat Mass Transfer*, vol. 50, no. 1920, pp. 3977 3989, 2007.

- [124] E. S. Landry and A. J. H. McGaughey, "Thermal boundary resistance predictions from molecular dynamics simulations and theoretical calculations," *Phys. Rev. B*, vol. 80, p. 165304, Oct 2009.
- [125] K. Termentzidis, P. Chantrenne, J.-Y. Duquesne, and A. Saci, "Thermal conductivity of gaas/alas superlattices and the puzzle of interfaces.," *J. Phys. Condens. Matter*, vol. 22, no. 47, p. 475001, 2010.
- [126] Y. Chalopin, K. Esfarjani, A. Henry, S. Volz, and G. Chen, "Thermal interface conductance in si/ge superlattices by equilibrium molecular dynamics," *Phys. Rev. B*, vol. 85, p. 195302, May 2012.
- [127] Z. Liang, K. Sasikumar, and P. Keblinski, "Thermal transport across a substrate thin-film interface: Effects of film thickness and surface roughness," *Phys. Rev. Lett.*, vol. 113, p. 065901, Aug 2014.
- [128] W. Zhang, T. S. Fisher, and N. Mingo, "The atomistic green's function method: An efficient simulation approach for nanoscale phonon transport," *Numer. Heat Tr. B-Fund.*, vol. 51, no. 4, pp. 333–349, 2007.
- [129] P. E. Hopkins, P. M. Norris, M. S. Tsegaye, and A. W. Ghosh, "Extracting phonon thermal conductance across atomic junctions: Nonequilibrium greens function approach compared to semiclassical methods," *J. Appl. Phys.*, vol. 106, no. 6, 2009.
- [130] J. Ravichandran, A. K. Yadav, R. Cheaito, P. B. Rossen, A. Soukiassian, S. J. Suresha, J. C. Duda, B. M. Foley, C.-H. Lee, Y. Zhu, A. W. Lichtenberger, J. E. Moore, D. A. Muller, D. G. Schlom, P. E. Hopkins, A. Majumdar, R. Ramesh, and M. A. Zurbuchen, "Crossover from incoherent to coherent phonon scattering in epitaxial oxide superlattices.," Nat. Mater., vol. 13, no. 2, pp. 168–72, 2014.
- [131] B. Jusserand, F. Mollot, J. Moison, and G. Le Roux, "Atomicscale roughness of gaas/alas interfaces: A raman scattering study of asymmetrical shortperiod superlattices," *Appl. Phys. Lett.*, vol. 57, no. 6, pp. 560–562, 1990.
- [132] T. Ruf, J. Spitzer, V. F. Sapega, V. I. Belitsky, M. Cardona, and K. Ploog, "Interface roughness and homogeneous linewidths in quantum wells and superlattices studied by resonant acoustic-phonon raman scattering," *Phys. Rev. B*, vol. 50, pp. 1792–1806, Jul 1994.
- [133] J. Belk, C. McConville, J. Sudijono, T. Jones, and B. Joyce, "Surface alloying at inas-gaas interfaces grown on (001) surfaces by molecular beam epitaxy," *Surf. Sci.*, vol. 387, no. 13, pp. 213 226, 1997.
- [134] M. R. Pillai, S.-S. Kim, S. T. Ho, and S. a. Barnett, "Growth of in[sub x]ga[sub 1x]as/gaas heterostructures using bi as a surfactant," *J. Vac. Sci. Technol. B Microelectron. Nanom. Struct.*, vol. 18, no. 3, p. 1232, 2000.

- [135] P. D. Robb and A. J. Craven, "Column ratio mapping: A processing technique for atomic resolution high-angle annular dark-field (haadf) images," *Ultramicroscopy*, vol. 109, no. 1, pp. 61 69, 2008.
- [136] B. Yang and G. Chen *Phys. Rev. B*, vol. 67, p. 195311, May 2003.
- [137] D. Botez, J. C. Shin, J. Kirch, C.-C. Chang, L. Mawst, and T. Earles, "Multidimensional conduction-band engineering for maximizing the continuous-wave (cw) wallplug efficiencies of mid-infrared quantum cascade lasers," *IEEE J. Sel. Topics Quantum Electron.*, vol. 19, pp. 1200312–1200312, Jul 2013.
- [138] Y. Wang, H. Huang, and X. Ruan, "Decomposition of coherent and incoherent phonon conduction in superlattices and random multilayers," *Phys. Rev. B*, vol. 90, p. 165406, Oct 2014.
- [139] S. B. Soffer, "Statistical model for the size effect in electrical conduction," *J. Appl. Phys.*, vol. 38, no. 4, pp. 1710–1715, 1967.
- [140] J. M. Ziman, Electrons and Phonons: The Theory of Transport Phenomena in Solids. London: Oxford University Press, 1960.
- [141] L. N. Maurer, Z. Aksamija, E. B. Ramayya, A. H. Davoody, and I. Knezevic, "Universal features of phonon transport in nanowires with correlated surface roughness," *Appl. Phys. Lett.*, vol. 106, no. 13, 2015.
- [142] A. A. Maznev, "Boundary scattering of phonons: Specularity of a randomly rough surface in the small-perturbation limit," *Phys. Rev. B*, vol. 91, p. 134306, Apr 2015.
- [143] Z. Aksamija and I. Knezevic, "Thermal conductivity of $\sin_{1-x} ge_x/\sin_{1-y} ge_y$ superlattices: Competition between interfacial and internal scattering," *Phys. Rev. B*, vol. 88, p. 155318, Oct 2013.
- [144] M. V. Simkin and G. D. Mahan, "Minimum thermal conductivity of superlattices," *Phys. Rev. Lett.*, vol. 84, pp. 927–930, Jan 2000.
- [145] W. A. Little, "The transport of heat between dissimilar solids at low temperatures," *Can. J. Phys.*, vol. 37, no. 3, pp. 334–349, 1959.
- [146] P. Reddy, K. Castelino, and A. Majumdar, "Diffuse mismatch model of thermal boundary conductance using exact phonon dispersion," *Appl. Phys. Lett.*, vol. 87, no. 21, pp. 1–3, 2005.
- [147] Y. K. Koh, Y. Cao, D. G. Cahill, and D. Jena, "Heat-transport mechanisms in super-lattices," Adv. Funct. Mater., vol. 19, no. 4, pp. 610–615, 2009.

- [148] M. Kazan, "Interpolation between the acoustic mismatch model and the diffuse mismatch model for the interface thermal conductance: Application to inn/gan superlattice," J. Heat Transfer, vol. 133, no. 11, p. 112401, 2011.
- [149] S. Simons, "On the thermal contact resistance between insulators," J. Phys. C Solid State Phys., vol. 7, no. 22, pp. 4048–4052, 1974.
- [150] T. Zeng and G. Chen, "Nonequilibrium electron and phonon transport and energy conversion in heterostructures," *Microelectron. J.*, vol. 34, no. 3, pp. 201 206, 2003.
- [151] M. A. Shahid, S. Mahajan, D. E. Laughlin, and H. M. Cox, "Atomic ordering in $ga_{0.47}in_{0.53}as$ and $ga_xin_{1-x}as_yp_{1-y}$ alloy semiconductors," *Phys. Rev. Lett.*, vol. 58, pp. 2567–2570, Jun 1987.
- [152] K. Shin, J. Yoo, S. Joo, T. Mori, D. Shindo, T. Hanada, H. Makino, M. Cho, T. Yao, and Y.-G. Park, "Ordering of in and ga in epitaxially grown injsub¿0.53i/sub¿gajsub¿0.47i/sub¿as films on (001) inp substrates," *MATER. TRANS.*, vol. 47, no. 4, pp. 1115–1120, 2006.
- [153] T. S. Kuan, W. I. Wang, and E. L. Wilkie, "Longrange order in inxga1xas," *Appl. Phys. Lett.*, vol. 51, no. 1, pp. 51–53, 1987.
- [154] T. Mori, T. Hanada, T. Morimura, K. Shin, H. Makino, and T. Yao, "Surface structure of ingaas/inp(001) ordered alloy during and after growth," *Appl. Surf. Sci.*, vol. 237, no. 14, pp. 230 234, 2004.
- [155] J. Kulik, R. Forrest, J. Li, T. Golding, S. C. Moss, and J. Bai, "X-ray and tem studies of short-range order in allxinxas thin films," *MRS Proceedings*, vol. 583, 1999.
- [156] R. L. Forrest, J. Kulik, T. D. Golding, and S. C. Moss, "X-ray diffraction and transmission electron microscopy analysis of ordering and structure in allxinxas thin films," *J. Mater. Res.*, vol. 15, no. 1, p. 4555, 2000.
- [157] T. Suzuki, "Basic aspects of atomic ordering in iii-v semiconductor alloys," in *Spontaneous Ordering in Semiconductor Alloys* (A. Mascarenhas, ed.), New York: Springer US, 2002.
- [158] T. Suzuki, T. Ichihashi, and T. Nakayama, "Observation of cupt-a type atomic ordering in alxin1xas alloys," *Appl. Phys. Lett.*, vol. 73, no. 18, pp. 2588–2590, 1998.
- [159] A. Gomyo, K. Makita, I. Hino, and T. Suzuki, "Observation of a new ordered phase in al_xin_{1-x} as alloy and relation between ordering structure and surface reconstruction during molecular-beam-epitaxial growth," *Phys. Rev. Lett.*, vol. 72, pp. 673–676, Jan 1994.

- [160] S. Ohkouchi, T. Furuhashi, A. Gomyo, K. Makita, and T. Suzuki, "Cross-sectional scanning tunneling microscopy observation of atomic arrangement in triple period-a type ordered alinas alloy," *Appl. Surf. Sci.*, vol. 241, no. 12, pp. 9 13, 2005.
- [161] T. S. Kuan, T. F. Kuech, W. I. Wang, and E. L. Wilkie, "Long-range order in $al_xga_{1-x}As$," *Phys. Rev. Lett.*, vol. 54, pp. 201–204, Jan 1985.
- [162] J. E. Bernard, R. G. Dandrea, L. G. Ferreira, S. Froyen, S. Wei, and A. Zunger, "Ordering in semiconductor alloys," *Appl. Phys. Lett.*, vol. 56, no. 8, pp. 731–733, 1990.
- [163] J. Tersoff, "New empirical approach for the structure and energy of covalent systems," *Phys. Rev. B*, vol. 37, pp. 6991–7000, Apr 1988.
- [164] J. Tersoff, "Modeling solid-state chemistry: Interatomic potentials for multicomponent systems," *Phys. Rev. B*, vol. 39, pp. 5566–5568, Mar 1989.
- [165] D. Powell, M. A. Migliorato, and A. G. Cullis, "Optimized tersoff potential parameters for tetrahedrally bonded iii-v semiconductors," *Phys. Rev. B*, vol. 75, p. 115202, Mar 2007.
- [166] L. Lindsay and D. A. Broido, "Optimized tersoff and brenner empirical potential parameters for lattice dynamics and phonon thermal transport in carbon nanotubes and graphene," *Phys. Rev. B*, vol. 81, p. 205441, May 2010.
- [167] S. Plimpton, "Fast parallel algorithms for short-range molecular dynamics," J. Comput. Phys., vol. 117, no. 1, pp. 1 19, 1995.
- [168] S. Nos, "A unified formulation of the constant temperature molecular dynamics methods," *The Journal of Chemical Physics*, vol. 81, no. 1, pp. 511–519, 1984.
- [169] W. G. Hoover, "Canonical dynamics: Equilibrium phase-space distributions," *Phys. Rev. A*, vol. 31, pp. 1695–1697, Mar 1985.
- [170] C. Z. Wang, C. T. Chan, and K. M. Ho, "Tight-binding molecular-dynamics study of phonon anharmonic effects in silicon and diamond," *Phys. Rev. B*, vol. 42, pp. 11276–11283, Dec 1990.
- [171] J. R. Lukes and H. Zhong, "Thermal conductivity of individual single-wall carbon nanotubes," *Int. J. Heat Transfer*, vol. 129, pp. 705–716, Jun 2007.
- [172] K. Nordlund, J. Nord, J. Frantz, and J. Keinonen, "Strain-induced kirkendall mixing at semiconductor interfaces," *Comput. Mater. Sci.*, vol. 18, no. 34, pp. 283 294, 2000.
- [173] K. Albe, K. Nordlund, J. Nord, and A. Kuronen, "Modeling of compound semiconductors: Analytical bond-order potential for ga, as, and gaas," *Phys. Rev. B*, vol. 66, p. 035205, Jul 2002.

- [174] G. Srivastava, The Physics of Phonons. London: Taylor & Francis, 1990.
- [175] T. Suzuki, T. Ichihasfh, and M. Tsuji, "Triple-period (tp)-a and cupt-a type ordering in al0.5in0.5as grown by metalorganic-vapor-phase-epitaxy," MRS Proceedings, vol. 583, 1999.
- [176] J. Duda, T. English, D. Jordan, P. Norris, and W. Soffa, "Controlling thermal conductivity of alloys via atomic ordering," *J. Heat Transfer*, vol. 134, p. 014501, Oct 2011.
- [177] J. C. Duda, T. S. English, D. A. Jordan, P. M. Norris, and W. A. Soffa, "Reducing thermal conductivity of binary alloys below the alloy limit via chemical ordering," *J. of Phys. Condens. Matter*, vol. 23, no. 20, p. 205401, 2011.
- [178] C. H. Baker and P. M. Norris, "Effect of long- and short-range order on sige alloy thermal conductivity: Molecular dynamics simulation," *Phys. Rev. B*, vol. 91, p. 180302, May 2015.